ornl

OAK RIDGE NATIONAL LABORATORY

UNION CARBIDE

OPERATED BY
UNION CARBIDE CORPORATION
FOR THE UNITED STATES
DEPARTMENT OF ENERGY

NUREG/CR-2753
ORNL-5886

Analysis of a Double-Ended Cold-Leg Break Simulation—THTF Test 3.05.5B

W. G. Craddick
R. E. Pevey

Prepared for the U.S. Nuclear Regulatory Commission
Office of Nuclear Regulatory Research
Under Interagency Agreements DOE 40-551-75 and 40-552-75

Printed in the United States of America. Available from
National Technical Information Service
U.S. Department of Commerce
5285 Port Royal Road, Springfield, Virginia 22161

Available from

GPO Sales Program
Division of Technical Information and Document Control
U.S. Nuclear Regulatory Commission
Washington, D.C. 20555

NUREG/CR-2753
ORNL-5886
Dist. Category AN

Contract No. W-7405-eng-26

Engineering Technology Division

ANALYSIS OF A DOUBLE-ENDED COLD-LEG BREAK SIMULATION - THTF TEST 3.05.5B

W. G. Craddick R. E. Pevey

Manuscript Completed - August 19, 1982
Date Published - September 1982

Prepared for the
U.S. Nuclear Regulatory Commission
Office of Nuclear Regulatory Research
Under Interagency Agreements DOE 40-551-75 and 40-552-75

NRC FIN. No. B0125

Prepared by the
OAK RIDGE NATIONAL LABORATORY
Oak Ridge, Tennessee 37830
operated by
UNION CARBIDE CORPORATION
for the
DEPARTMENT OF ENERGY

CONTENTS

ACKNOWLEDGMENTS

The authors express their appreciation to R. C. Hagar and M. S. Thompson for their assistance in preparing many of the graphs used in this report. R. C. Hagar also provided valuable advice on the application of the PINSIM code. Pretest planning of THTF Test 3.05.5B was performed by R. C. Hagar and D. G. Morris. D. G. Morris also assisted in the performance of posttest calculations. The authors also express their appreciation to all of those who participated in the conduct and data reduction of the test:

T. M. Anklam
J. L. Bartley
D. H. Cook
R. D. Dabbs
R. L. Durrall
D. K. Felde
R. M. Flanders
D. J. Fraysier
S. S. Gould
R. H. Greene
R. C. Hagar
D. F. Hunt
C. R. Hyman
D. G. Madewell
D. G. Morris
C. B. Mullins
L. J. Ott
W. Ragan, Jr.
J. J. Robinson
A. G. Sutton
J. W. Teague, II
R. E. Textor
M. S. Thompson
B. J. Beazie
J. D. White
M. D. White
J. E. Wolfe
G. L. Yoder

ANALYSIS OF A DOUBLE-ENDED COLD-LEG BREAK SIMULATION - THTF TEST 3.05.5B

W. G. Craddick R. E. Pevey

ABSTRACT

On July 3, 1980, an experiment was performed in the Oak Ridge National Laboratory Thermal-Hydraulic Test Facility that simulated a double-ended cold-leg break pressurized-water reactor (PWR) accident. Analysis of the experiment revealed that nuclear fuel rods exposed to the same hydrodynamic environment as that which existed in the experiment would have departed from nucleate boiling both earlier and later than the fuel rod simulator (FRS), depending on the size of the gap between the nuclear fuel pellets and cladding and on the initial power of the nuclear fuel rod. Comparison of the results of the current experiment, which used an FRS bundle with geometry similar to 17 x 17 PWR fuel assemblies, to the results of earlier experiments, which used an FRS bundle with geometry similar to 15 x 15 PWR fuel assemblies, revealed no differences that can be attributed to the difference in geometries.

1. INTRODUCTION

On July 3, 1980, an experiment was performed at the Oak Ridge National Laboratory (ORNL) Thermal-Hydraulic Test Facility (THTF) that was intended to simulate the conditions that would occur in the core of a pressurized-water reactor (PWR) during a double-ended cold-leg break (DECLB) accident. The experiment was designated THTF Test 3.05.5B and was conducted as part of the PWR Blowdown Heat Transfer (BDHT) Separate-Effects Program sponsored by the Nuclear Regulatory Commission (NRC). The objectives of the experiment were to obtain data on time to departure from nucleate boiling (DNB) and to provide data that can be used to benchmark transient reactor analysis codes. This report describes the analyses that have been performed to investigate the extent to which the results of THTF Test 3.05.5B can be used to draw conclusions about the behavior of a nuclear reactor during a DECLB.

The PWR-BDHT Separate-Effects Program was begun in 1972 and will be completed early in 1982. During this period, the program objectives have changed considerably. During the past 2 years, the principal objective of

the program has been to obtain data on heat transfer coefficients and related parameters under a variety of accident conditions. Prior to this time, the program's principal objective was to obtain data on time to DNB during simulations of large break loss-of-coolant accidents (LOCAs). THTF Test 3.05.5B was the only test conducted in the last 2 years with the objective of simulating core conditions during a DECLB.

The experiment was conducted in the THTF, a heavily instrumented nonnuclear pressurized-water loop containing 64 full-length [3.66-m (12-ft)] rods arranged in an 8 x 8 square lattice.[1] Sixty of the 64 rods are electrically heated fuel rod simulators (FRSs). The four unheated rods are located within the lattice in positions that would be occupied by control rods in a 17 x 17 PWR fuel assembly. The FRS diameter [0.95 cm (0.374 in.)] and the pitch of the lattice [1.27 cm (0.501 in.)] are typical of late generation 17 x 17 PWR fuel assemblies. The THTF is capable of achieving pressures in excess of 15.9 MPa (2300 psia) and temperatures in excess of 1089 K (1500°F). Data are recorded from every instrument at intervals no larger than 0.05 s.

The relationship of the behavior of FRSs in an experimental facility such as the THTF to the behavior of nuclear fuel rods during an actual reactor accident may be considered in two parts. First, to what extent does the behavior of the FRS simulate the behavior of a nuclear fuel rod exposed to the same fluid conditions? Second, to what extent do the fluid conditions produced during the experiment correspond to the fluid conditions that would exist during an actual reactor accident? The former question is addressed in some detail in this report through the use of the PINSIM computer code;[2] PINSIM is essentially a generalized one-dimensional heat conduction code for cylindrical geometries. The code is used to perform two types of calculations aimed at relating FRS behavior to nuclear fuel rod behavior; these will be referred to as back calculations (described in Chap. 4) and forward calculations (described in Chap. 5).

The extent of the similarity of the fluid conditions in the experiment to the fluid conditions in an actual reactor accident is extremely difficult to determine. This difficulty stems from several factors. To make the needed comparison, one must calculate the bundle fluid conditions for both the experiment and a reactor accident. Because the THTF does not

have flow measuring sites within the rod bundle, calculation of bundle fluid conditions must use a thermal-hydraulic code with boundary conditions supplied from measurements made outside of the rod bundle. The nature of Test 3.05.5B makes this task extremely difficult. The outlet of the test section saturates immediately in the experiment, and the inlet to the test section saturates after ~2 s. Thus, we are faced with the task of measuring two-phase flow at both the test section inlet and outlet through most of the transient. The accurate measurement of two-phase flow is, of course, extremely difficult. These difficulties are compounded by the fact that the flow reversed direction during the test. Flow reversals cause periods of flow too low to be measured accurately. The difficulty in determining bundle fluid conditions accurately in such an environment is well documented.[3,4] We currently have no means to accurately calculate bundle fluid conditions under these conditions.

The calculation of bundle fluid conditions that would exist in a reactor during a large break LOCA must be accomplished by means of a thermal-hydraulic code used in a purely predictive manner. The extent to which currently existing codes can accurately predict such conditions for an actual reactor remains unknown. And even if accurate bundle fluid conditions could be obtained for both the experiment and a reactor accident, the means by which we could assess the significance of any observed discrepancies between the conditions is uncertain. This report does contain comparisons of the predictions of RELAP4 MOD5 Update 2 of a 200% cold-leg break and bundle fluid conditions calculated for Test 3.05.5B (Chap. 2). However, due to the large uncertainties connected with both of these calculations, no reliable judgments can currently be made of the extent or significance of differences in fluid conditions between the experiment and an actual reactor accident.

Chapter 5 contains a brief discussion of tests that were conducted earlier in the THTF. These tests used a rod bundle that had geometries similar to that of a 15 x 15 PWR fuel assembly in contrast to the geometry of a 17 x 17 PWR fuel assembly used in Test 3.05.5B. Before presenting the analytical results, a discussion of the planning and conduct of the tests and the facility is presented.

2. EXPERIMENTAL PROCEDURE

2.1 Facility Description

A schematic of the THTF as configured for Test 3.05.5B is shown in Fig. 2.1. The THTF does not attempt to model components outside of a reactor core. Thus the heat exchangers, pressurizer, and pump are used only to achieve reactor-like conditions in the test section that contains the rod bundle. To facilitate instrumentation, a downcomer external to the test section is used. While the test section is heavily instrumented with temperature and pressure sensors, flow measurement sites exist only outside the test section in instrumented "spool pieces." A spool piece typically contains temperature and pressure sensors, a single- or triple-beam gamma densitometer, and drag body and turbine flowmeters. The location of specific spool-piece instruments is shown in Fig. 2.2 with the following key to instrument designations.

Instrument designations consist of a group of letters that identify the type of instrument followed by a number used to distinguish instruments of similar type. The letter designations are as follows:

DE Gamma densitometer (If the identifying number is followed by the letter A, B, or C, the instrument is a triple-beam densitometer, and the letters identify the separate beams. Otherwise, it is a single-beam densitometer.)

PE Absolute-pressure sensor

TE Thermocouple

FE Turbine flowmeter

FMFE Drag body flowmeter

PdE Pressure-difference sensor

A schematic of the THTF as configured for tests before 1980 (Refs. 5 and 6) is shown in Fig. 2.3. Principal differences are the annular downcomer, rather than the external downcomer with additional instrumented spool pieces, and lack of a spool piece on the test section outlet horizontal piping. The implications of these differences are discussed in more detail in Chap. 5.

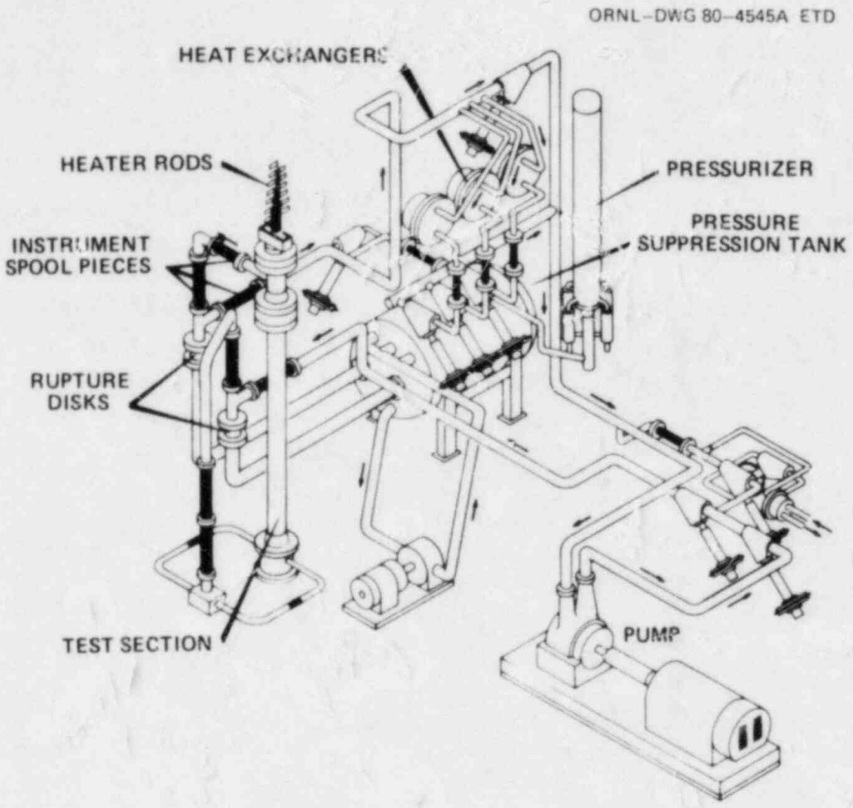

Fig. 2.1. Major components of THTF for Test 3.05.5B.

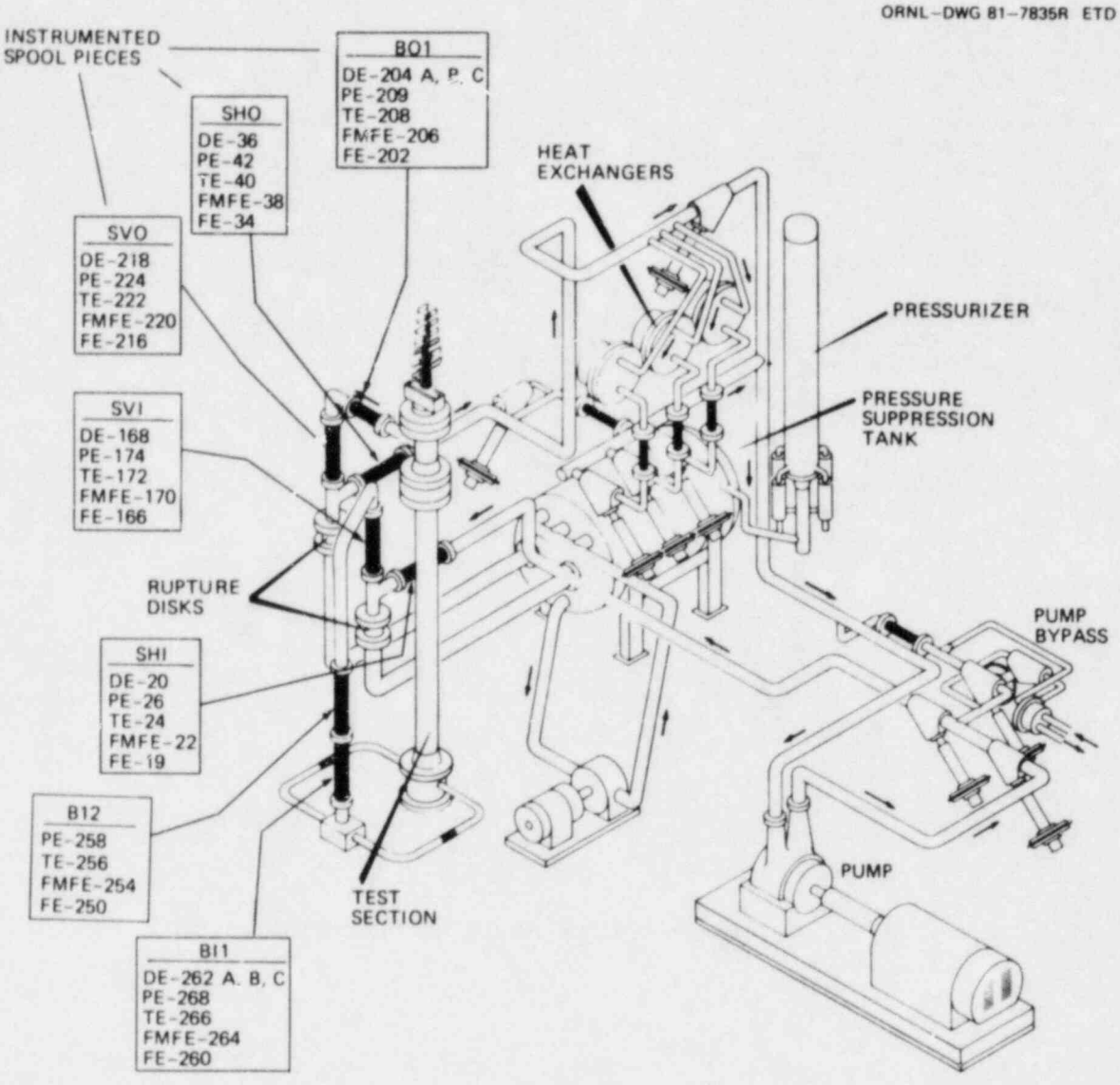

Fig. 2.2. Primary instruments outside the test section for THTF Test 3.05.5B.

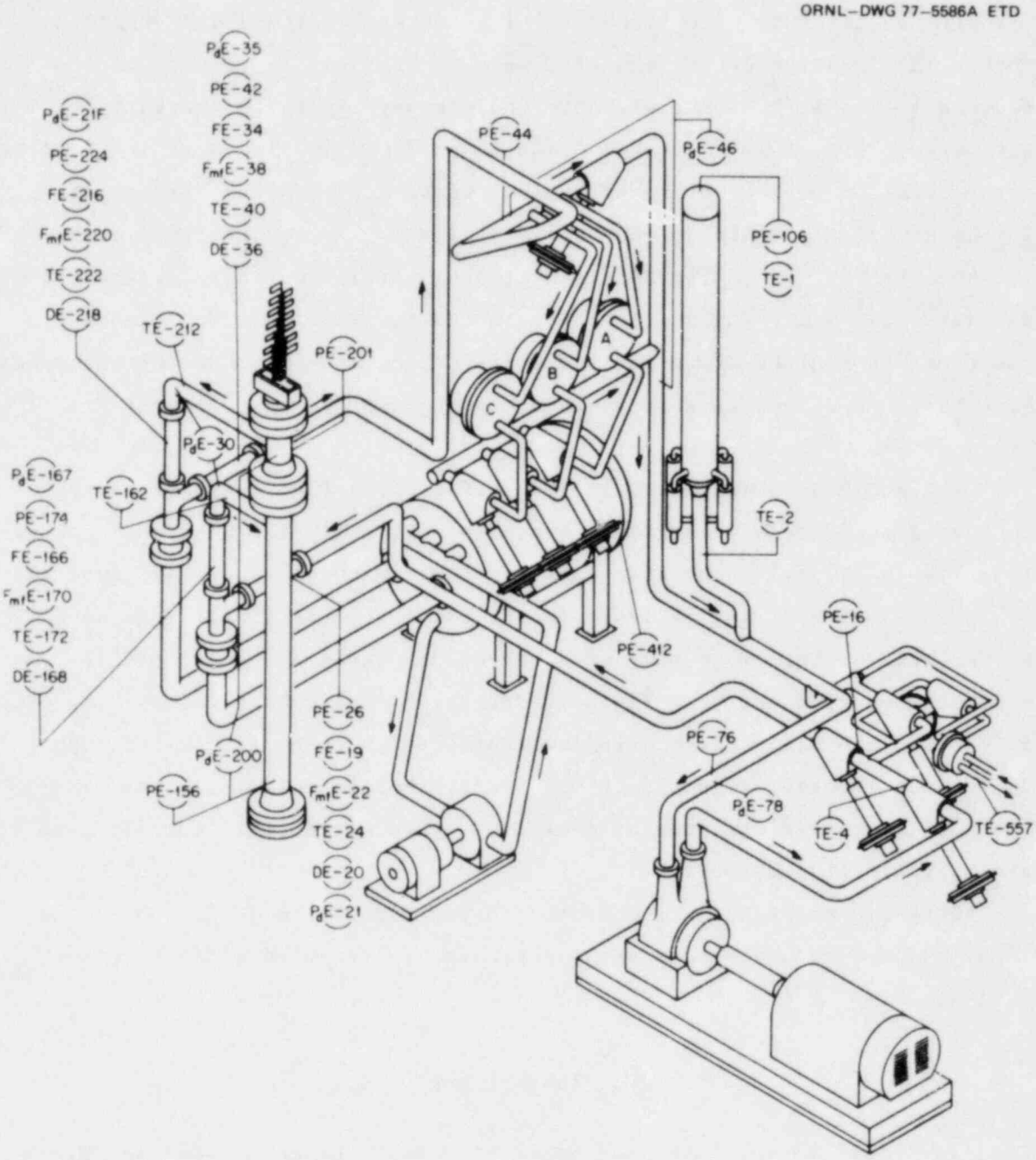

Fig. 2.3. Primary instruments outside the test section for THTF tests before 1980.

The rod bundle contained in the test section for Test 5B consisted of 64 rods arranged as shown in Fig. 2.4. The bundle is composed of 60 electrically heated FRSs with 3.66-m (12-ft) heated lengths and 4 unheated rods. The location of the unheated rods is the same as that of control rods in a 17 x 17 PWR fuel assembly (note upper-right one-fourth of 17 x 17 assembly in Fig. 2.5). The FRS diameter [0.95 cm (0.374 in.)] and lattice pitch [1.27 cm (0.501 in.)] are typical of 17 x 17 PWR fuel assemblies. The axial power profile in the bundle is flat. The construction of an FRS is shown in Fig. 2.6. The rod is heated by passing current through the Inconel cylinder. From one to three sheath thermocouples may have their junctions at a given elevation. The elevations at which FRS thermocouples have their junctions as well as the locations of the spacer grids are shown in Fig. 2.7.

The rod bundle contained in the test section for tests before 1980 consisted of 49 rods arranged as shown in Fig. 2.8. The heated length was also 3.66 m (12 ft). The FRS diameter [1.07 cm (0.422 in.)] was typical of 15 x 15 PWR fuel assemblies. In the first six tests, all rods were heated; thereafter, four rods were unheated. The axial power profile was a stepped chopped-cosine. The construction of these FRSs is shown in Fig. 2.9. They are heated by passing current through the cylinders of cupronickel and Inconel. The elevations of the thermocouple junctions, locations of spacer grids, and the peak-to-average power ratio for the bundle are shown in Fig. 2.10.

Data are acquired by a computer-controlled data acquisition system (DAS) and are recorded from each instrument at least as often as every 0.05 s.

2.2 Test Planning and Conduct

Test 3.05.5B was conducted by first establishing the desired initial conditions and allowing the facility to come to steady state. Once steady state was achieved, rupture disk assemblies were activated at the test section inlet and outlet. These assemblies produced a break of a predetermined, constant size. The breaks were connected to an effluent tank kept at atmospheric pressure. The total power delivered to the core was

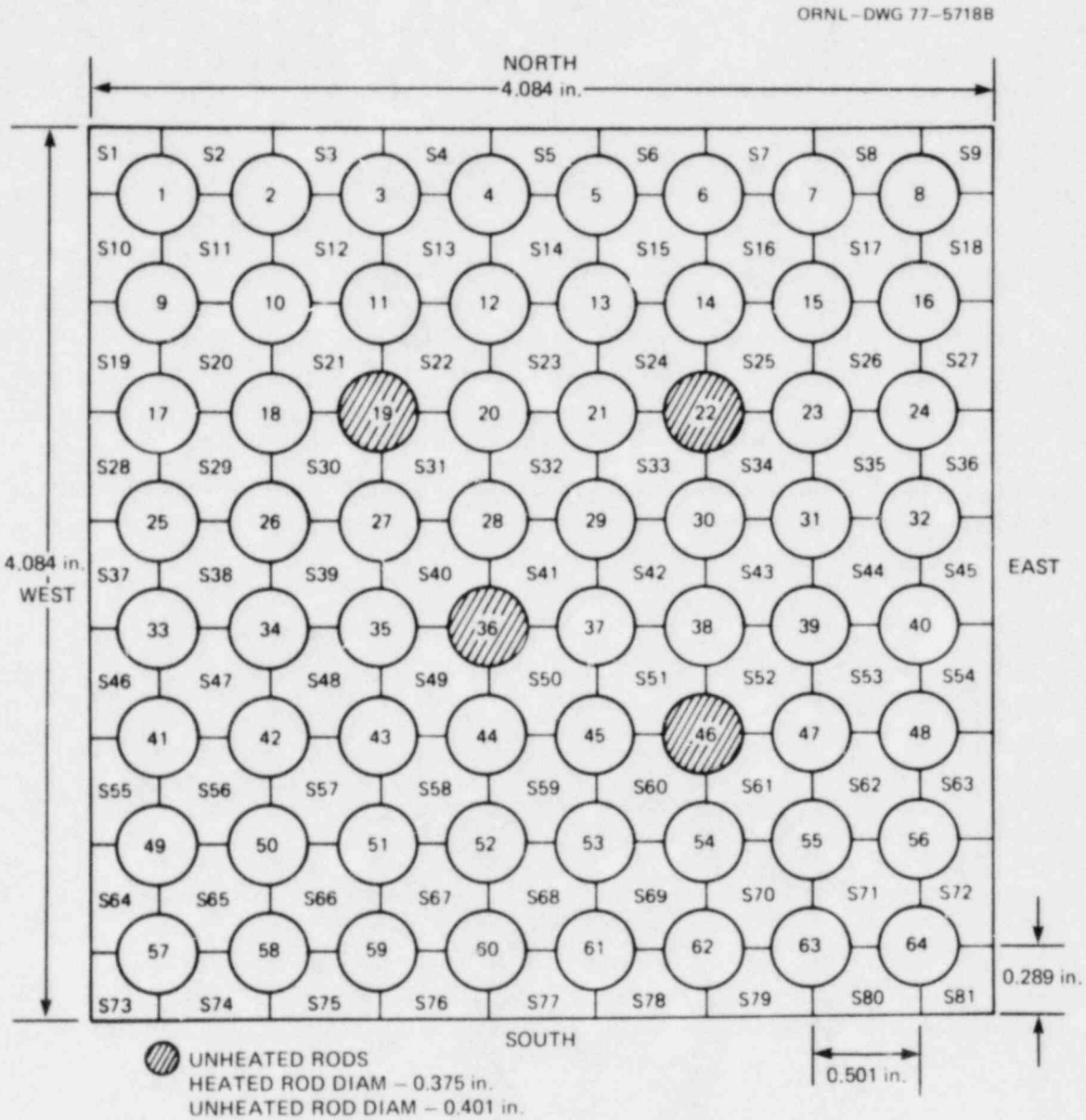

Fig. 2.4. Bundle cross section showing rods and subchannels for THTF Test 3.05.5B.

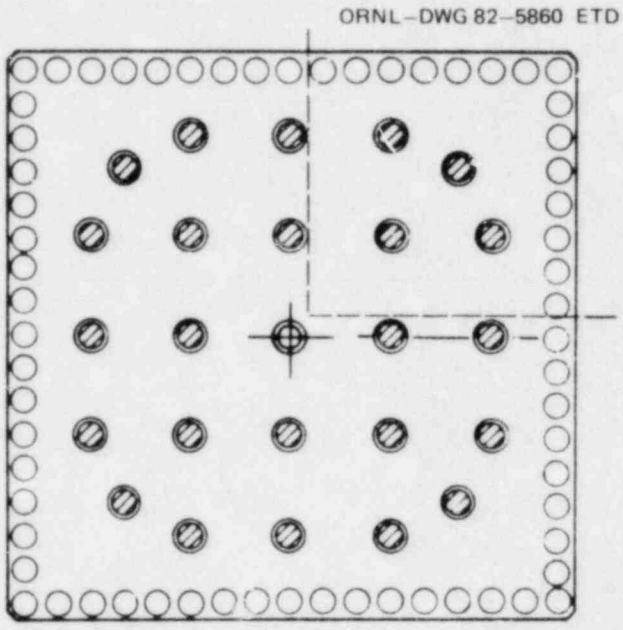

Fig. 2.5. Bundle cross section of 17 x 17 PWR fuel assembly showing location of unheated rods.

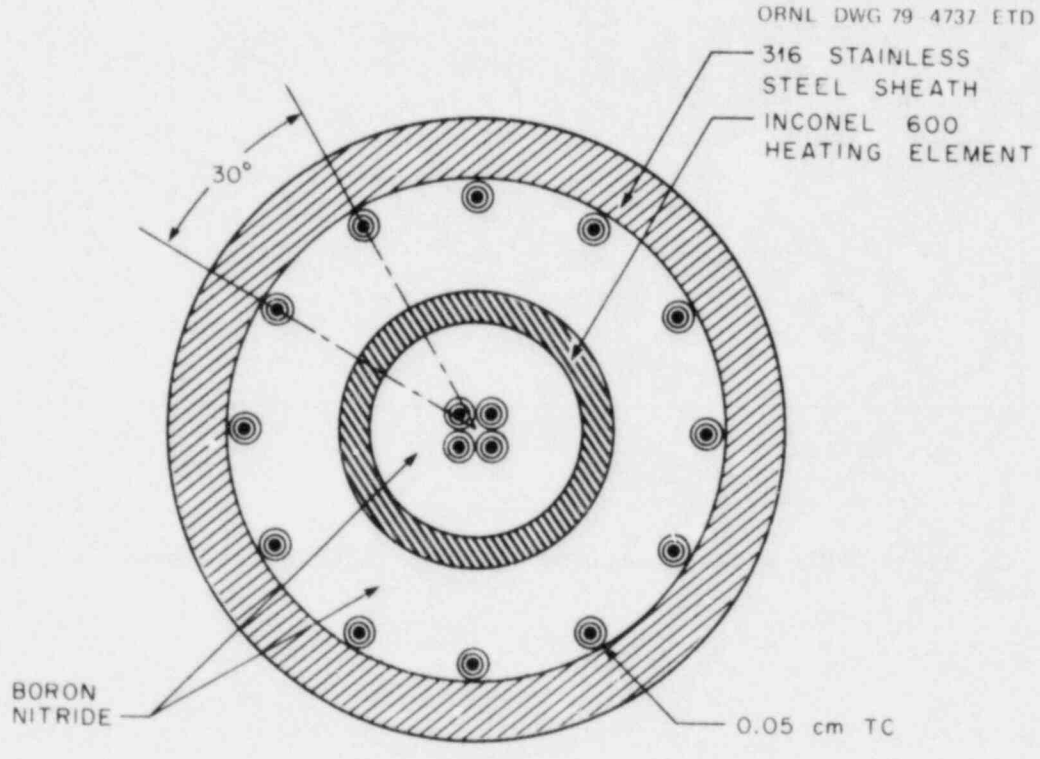

Fig. 2.6. Cross section of FRS for THTF Test 3.05.5B.

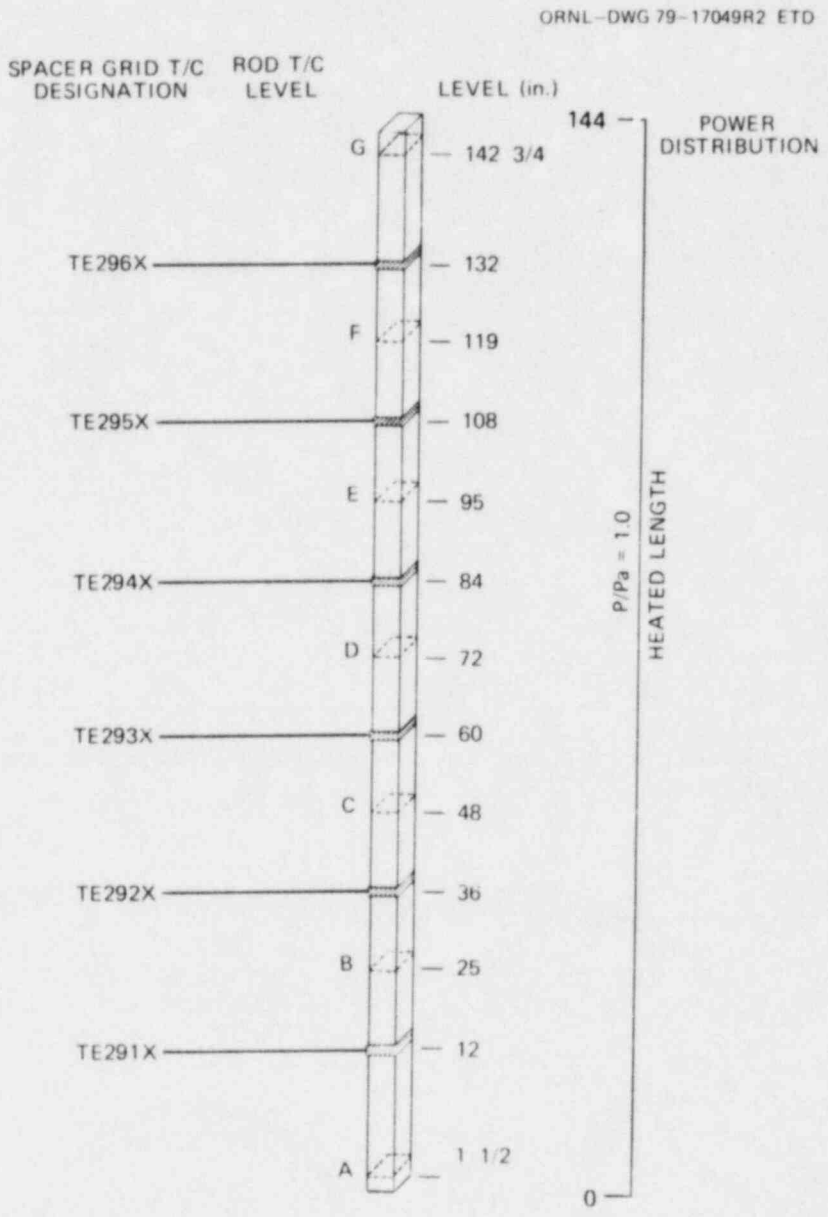

Fig. 2.7. Axial location of spacer-grid and FRS thermocouples for THTF Test 3.05.5B.

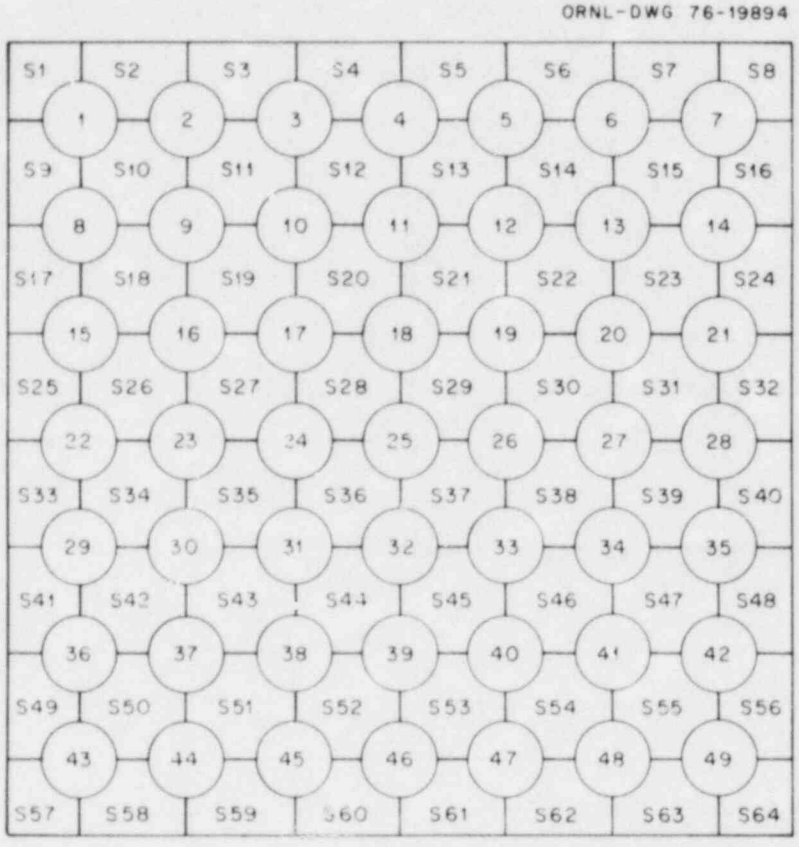

Fig. 2.8. Bundle cross section showing rods and subchannels for THTF tests before 1980.

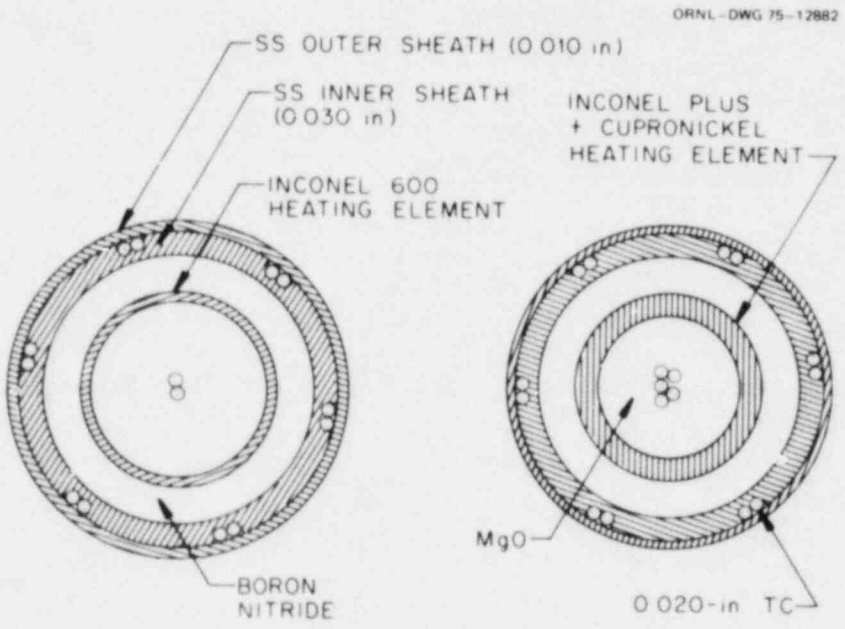

Fig. 2.9. Cross section of FRS for THTF tests before 1980.

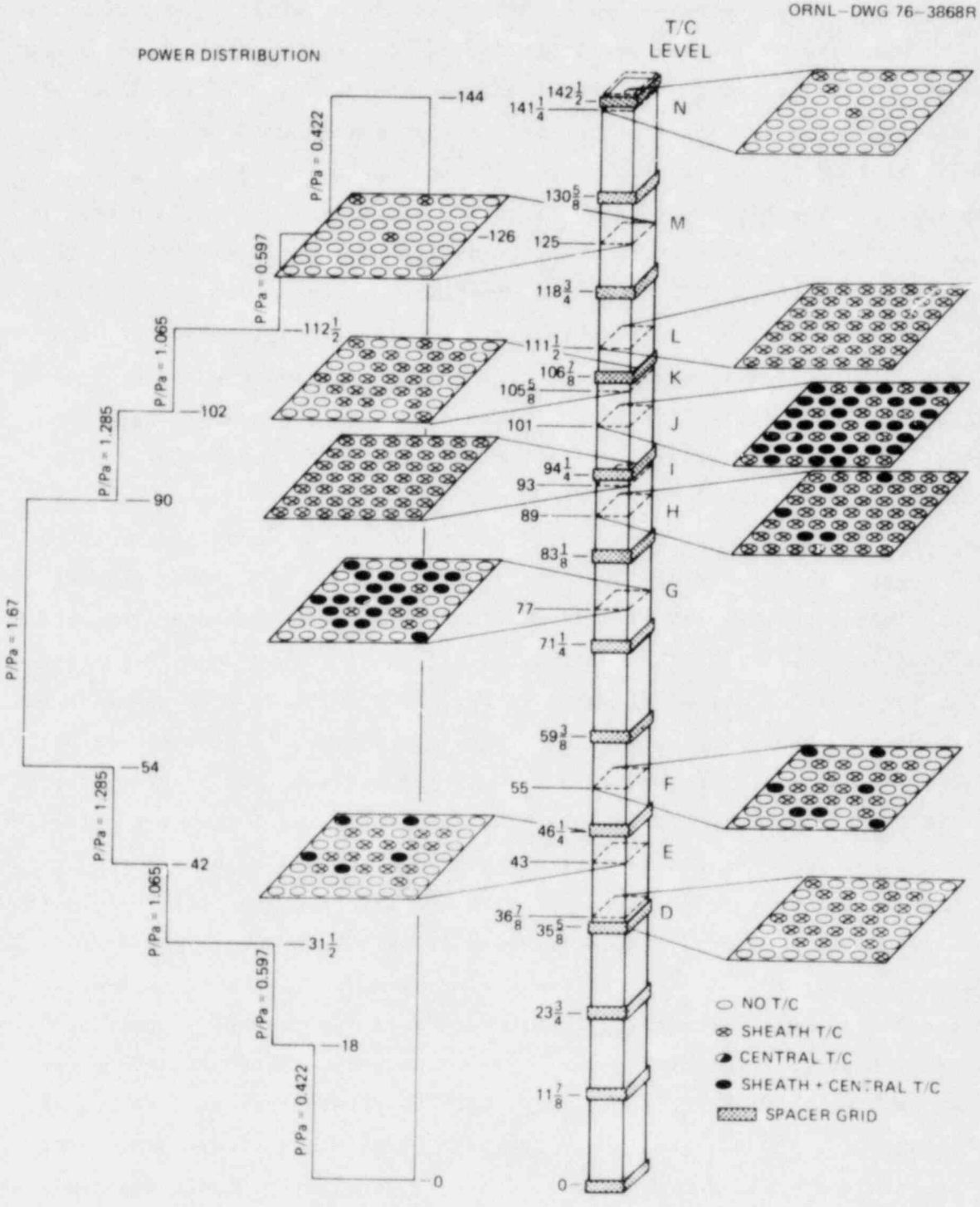

Fig. 2.10. Axial location of FRS thermocouples and axial power profile for THTF tests before 1980.

varied through the transient in accordance with the predetermined power "program." Data recording by the DAS began ~30 s before break initiation.

Thus, the parameters available for the experimenter's selection are initial pressure, test section inlet temperature, test section flow rate, total bundle power, inlet and outlet break sizes, and the power program. For Test 3.05.5B, these parameters were chosen in an effort to match as closely as possible the conditions that would exist in a nuclear reactor during a 200% cold-leg break. The initial conditions for a PWR can be well matched by the THTF except for the discrepancy between the THTF's flat axial power profile and a reactor's cosine profile. However, the inability to exert active control over the hydrodynamics once the transient has begun (except for the limited effect of the power program) severely limits the extent to which a set of desired conditions can be matched through time.

The source for the core conditions of a reactor undergoing a DECLB was a prediction of RELAP4 MOD5 Update 2. A RELAP4 model of a Westinghouse four-loop PWR with 17 x 17 fuel assemblies was obtained from Sandia National Laboratory.[7] The model was modified to remove upper-head injection resulting in the model shown in Fig. 2.11. RELAP4 MOD5 Update 2 was then used to model the entire THTF (the "system" model) as shown in Fig. 2.12. The system model was then used to produce a series of predictions of THTF behavior with varying break sizes. The break sizes were selected that caused RELAP4's predictions for the THTF to best match its predictions for a reactor. The power program for the experiment was determined using the PINSIM code. PINSIM was used to calculate the response of a nuclear fuel rod to the hydrodynamic conditions predicted by RELAP4 to occur during the experiment. PINSIM then used the surface temperature and surface heat flux calculated for the nuclear rod to determine the power that must be supplied to the electric FRS to produce the same responses. The determination of input power from the surface heat flux and surface temperature will be referred to as a "back" calculation (described in more detail in Chap. 3 and Appendix A). At this point, it is sufficient to say that a back calculation was used in an attempt to arrive at a power program with the electric FRS that would compensate for the internal differences between an electric rod and a nuclear rod to produce behavior in the electric rod similar to that which would occur in a nuclear fuel rod.

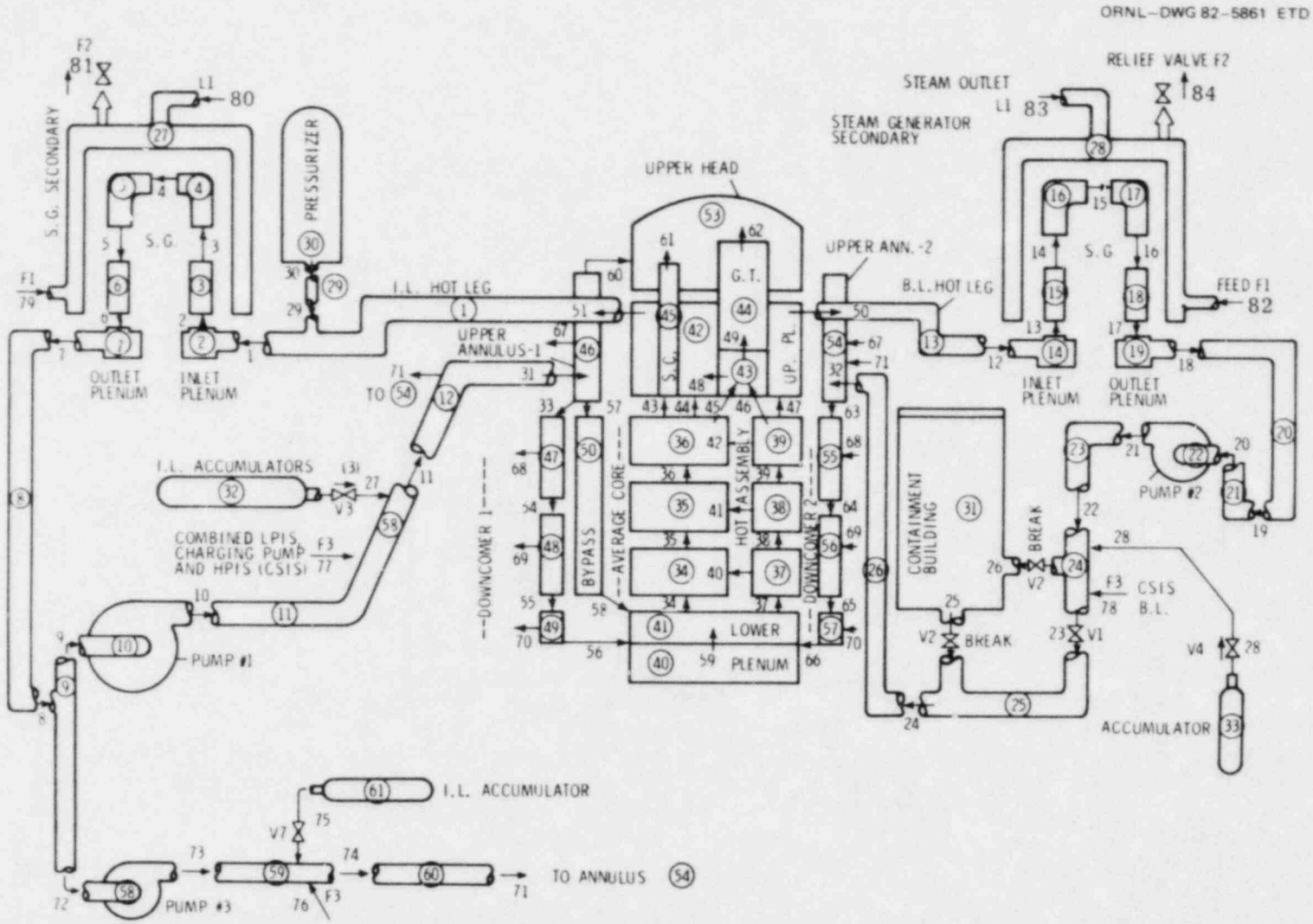

Fig. 2.11. RELAP4 MOD5 update 2 nodalization of representative PWR primary side.

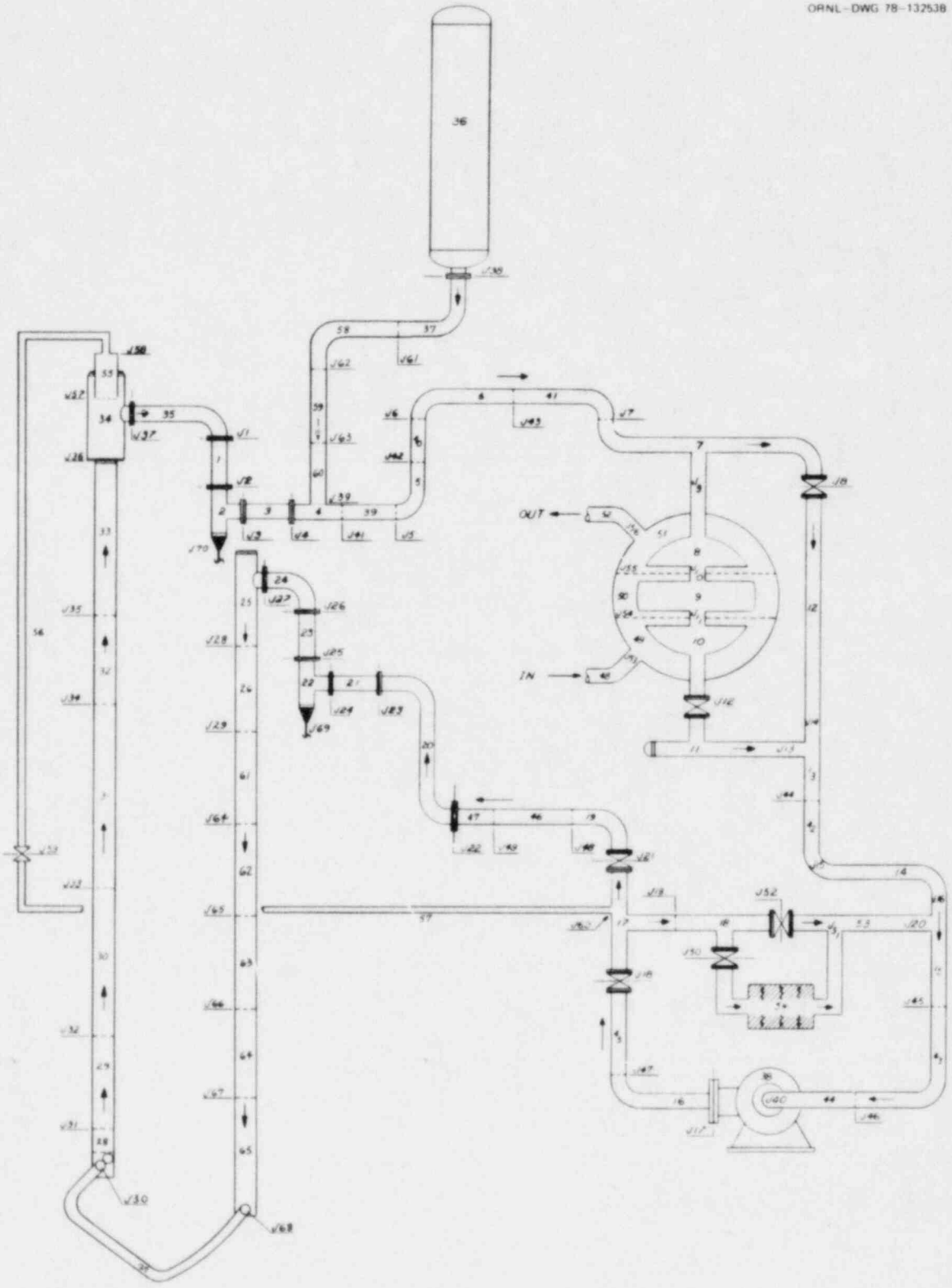

Fig. 2.12. RELAP4 MOD5 update 2 nodalization of THTF primary side.

A summary of the initial conditions for Test 3.05.5B is contained in Table 2.1. The variation in power supplied to the electric FRSs is shown in Fig. 2.13.

Having described the planning and conduct of the experiment, a brief graphical summary of the test results will be provided. Figures 2.14–2.17 show the temporal variation of the pressure, temperature, density, and volumetric flow as measured at the test section inlet. Figures 2.18–2.21 show the same quantities for the test section outlet. Approximately 1 in. above the top of the heated length, a thermocouple rake with fluid thermocouples projects into the subchannels. Representative responses from these thermocouples are shown in Fig. 2.22.

The instrument responses for all instruments for Test 3.05.5B have been provided to the NRC data bank at Idaho National Engineering Laboratory. These instrument responses have also been documented in a data report[8] along with a complete description of instrument uncertainties.

As described earlier (Fig. 2.6), each FRS contains a number of internal thermocouples. The quantities of principal interest are the surface heat flux and surface temperature of the FRSs, and these quantities must be calculated from the instrument responses. This task is accomplished by the computer code ORINC (Ref. 9). ORINC uses the measured sheath temperatures, the measured electrical current supplied to each rod, and thermophysical properties determined from in situ calibrations[10] to calculate the rod surface temperatures and surface heat fluxes. Representative surface temperatures and surface heat fluxes for each thermocouple level (Fig. 2.7) are shown in Figs. 2.23–2.36.

Table 2.1. Initial conditions for Test 3.05.5B

Quantity	Initial value
System pressure (PE-209)	14.84 MN/m² (2153 psia)
Test section inlet temperature (TE-266)	550 K (531°F)
Test section outlet temperature (TE-208)	603 K (625°F)
Core power	124 kW/rod
Test section inlet volumetric flow rate (FE-250)	31.5 L/s (505 gpm)
Bundle mass flux	3965 kg/s·m² (2.93×10^6 $lb_m/h \cdot ft^2$)
Inlet break size	4.01 cm² (0.622 in.²)
Outlet break size	3.51 cm² (0.544 in.²)

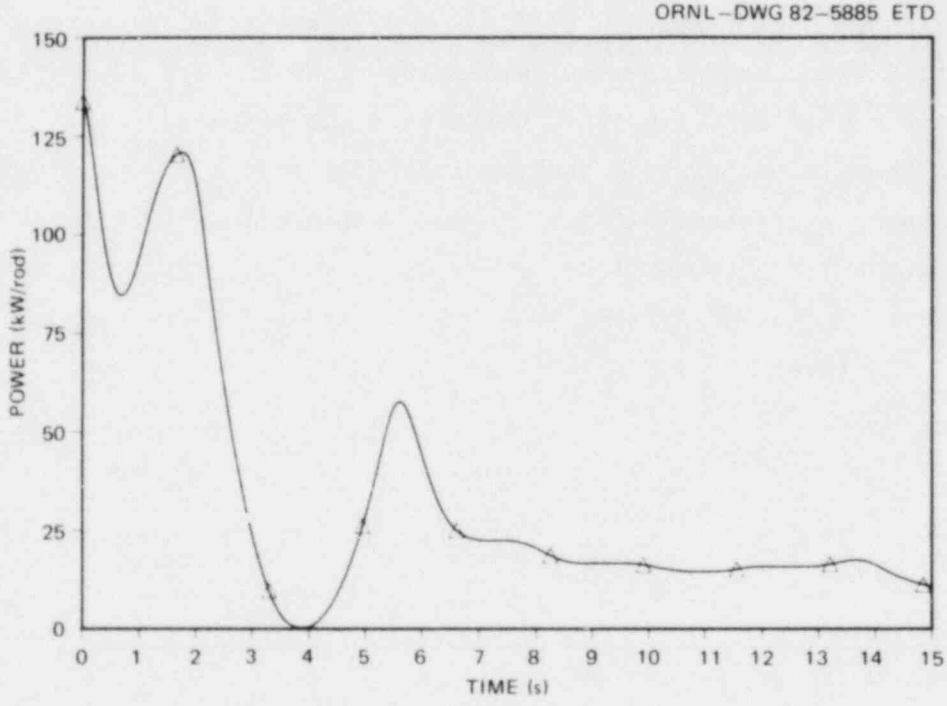

Fig. 2.13. Power as a function of time for THTF Test 3.05.5B.

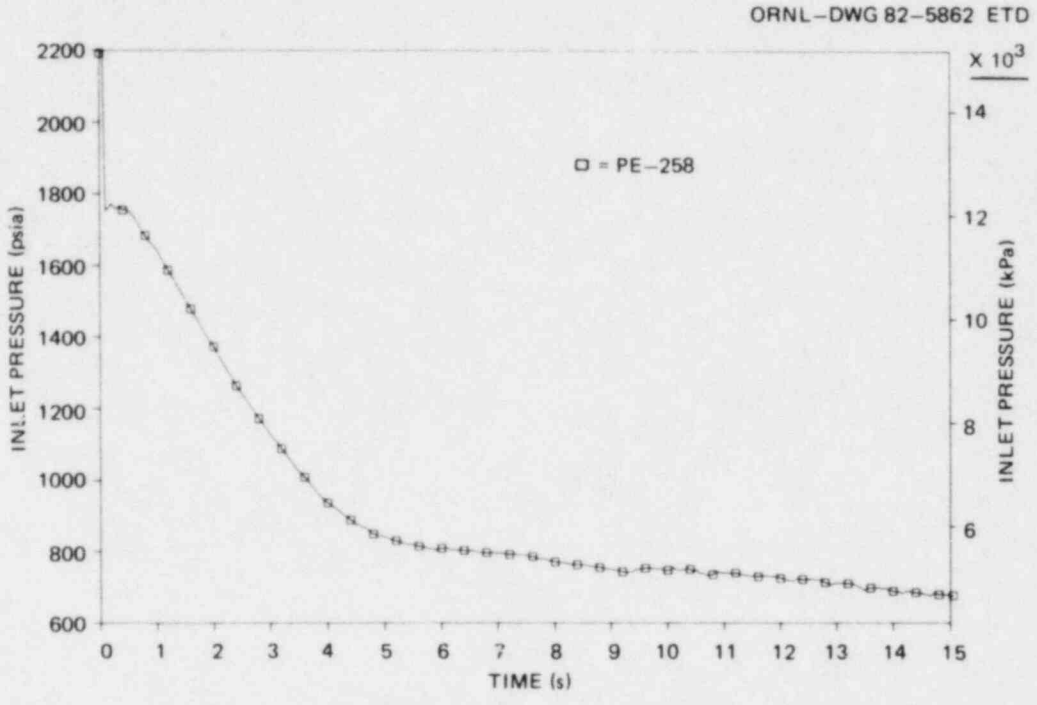

Fig. 2.14. Instrument responses from THTF Test 3.05.5B – inlet spool-piece pressure.

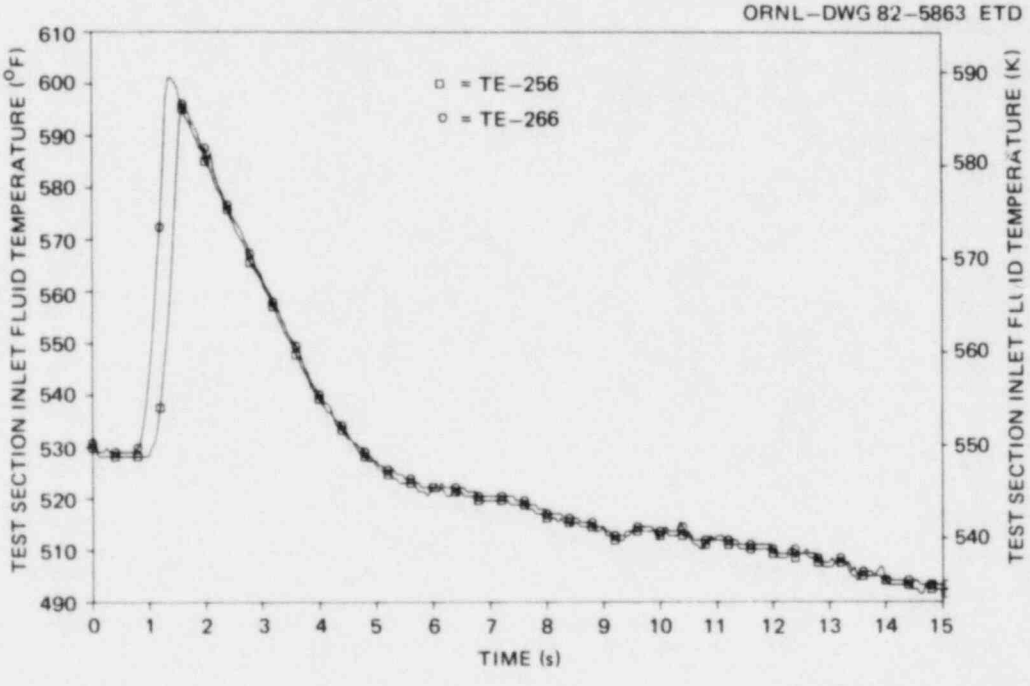

Fig. 2.15. Instrument responses from THTF Test 3.05.5B – inlet spool-piece fluid temperatures.

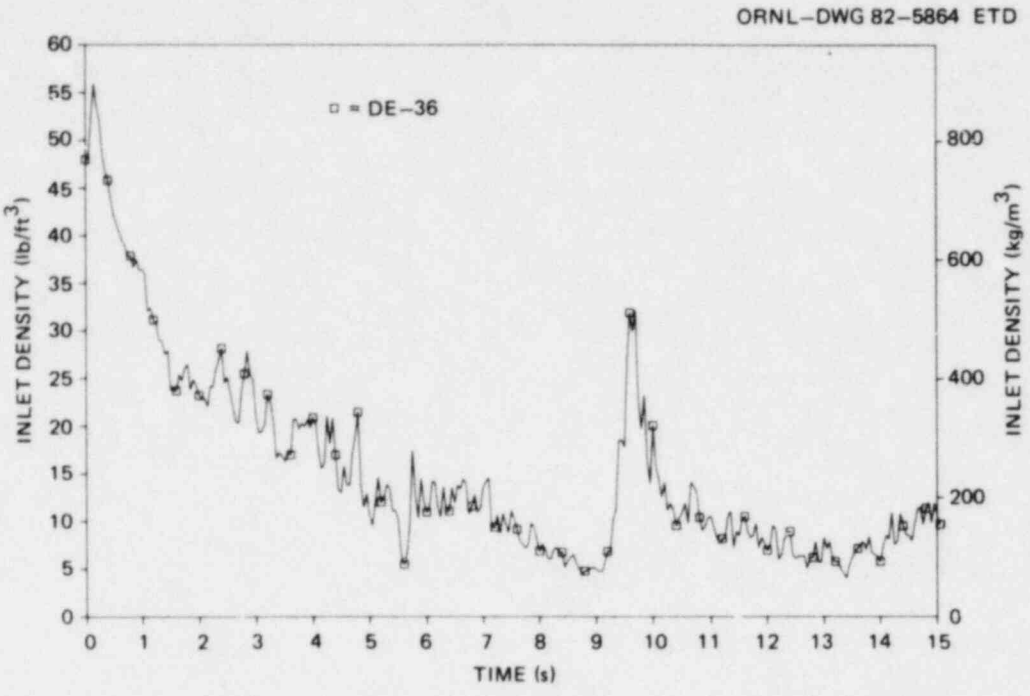

Fig. 2.16. Instrument responses from THTF Test 3.05.5B – inlet spool-piece fluid density.

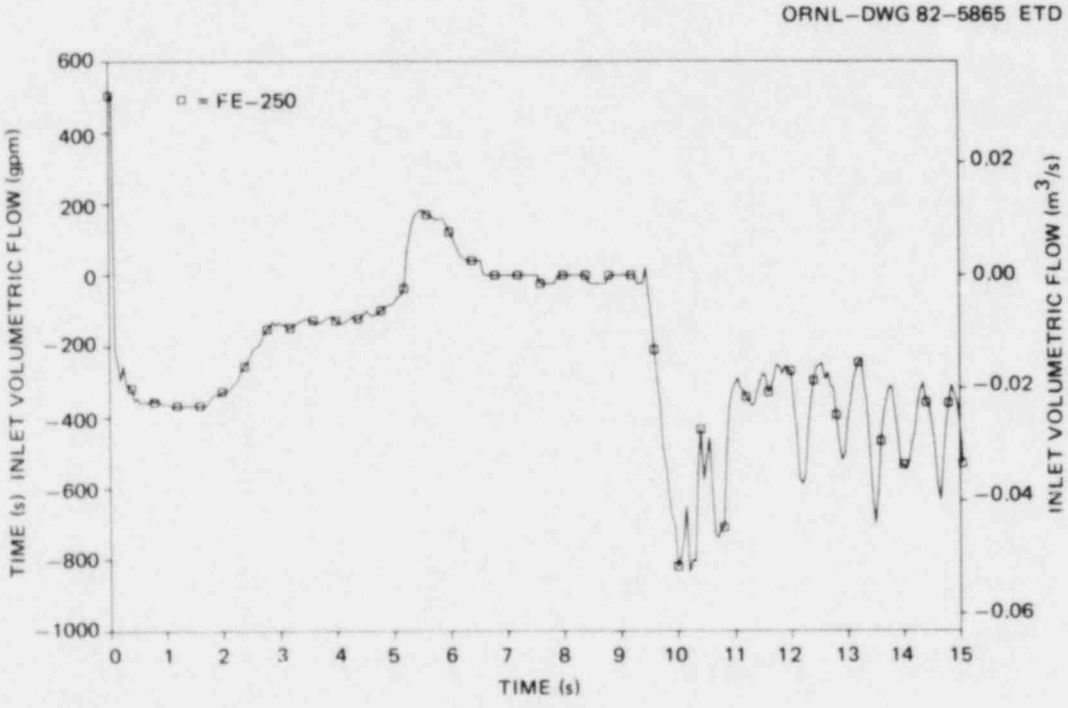

Fig. 2.17. Instrument responses from THTF Test 3.05.5B – inlet spool-piece volumetric flow.

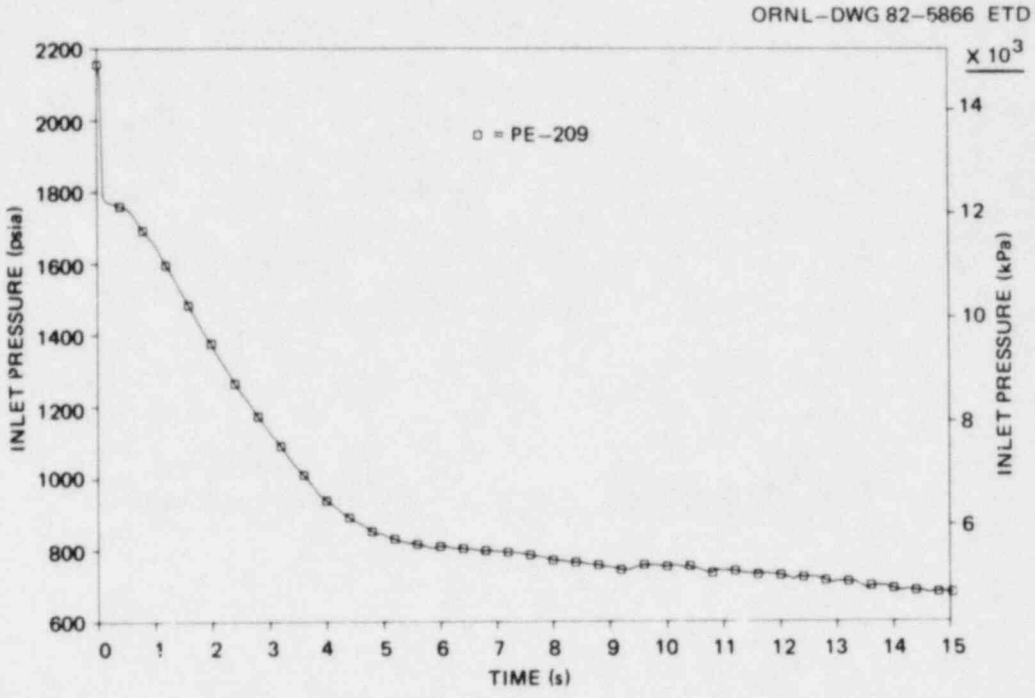

Fig. 2.18. Instrument responses from THTF Test 3.05.5B – outlet spool-piece pressure.

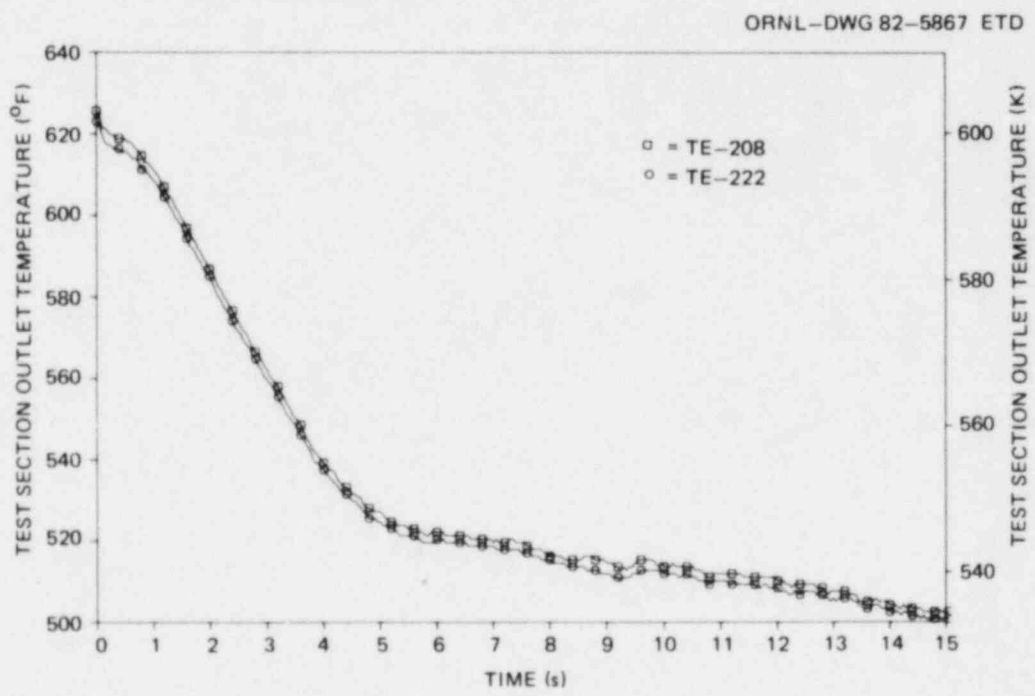

Fig. 2.19. Instrument responses from THTF Test 3.05.5B – outlet spool-piece fluid temperatures.

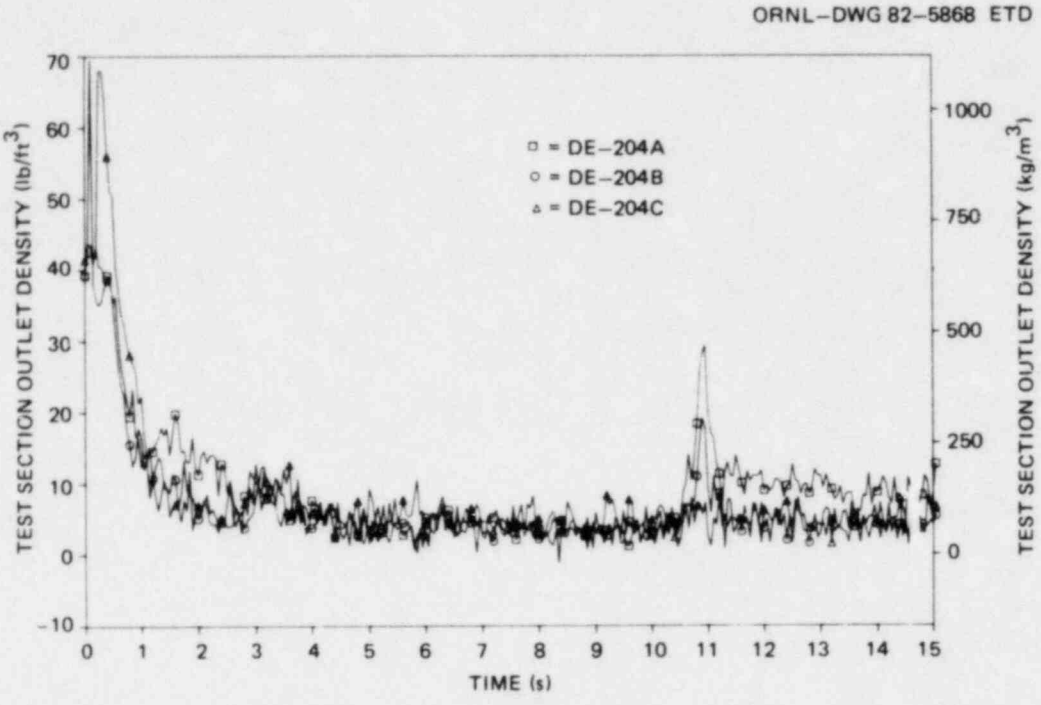

Fig. 2.20. Instrument responses from THTF Test 3.05.5B – outlet spool-piece fluid density from each beam of triple-beam gamma densitometer.

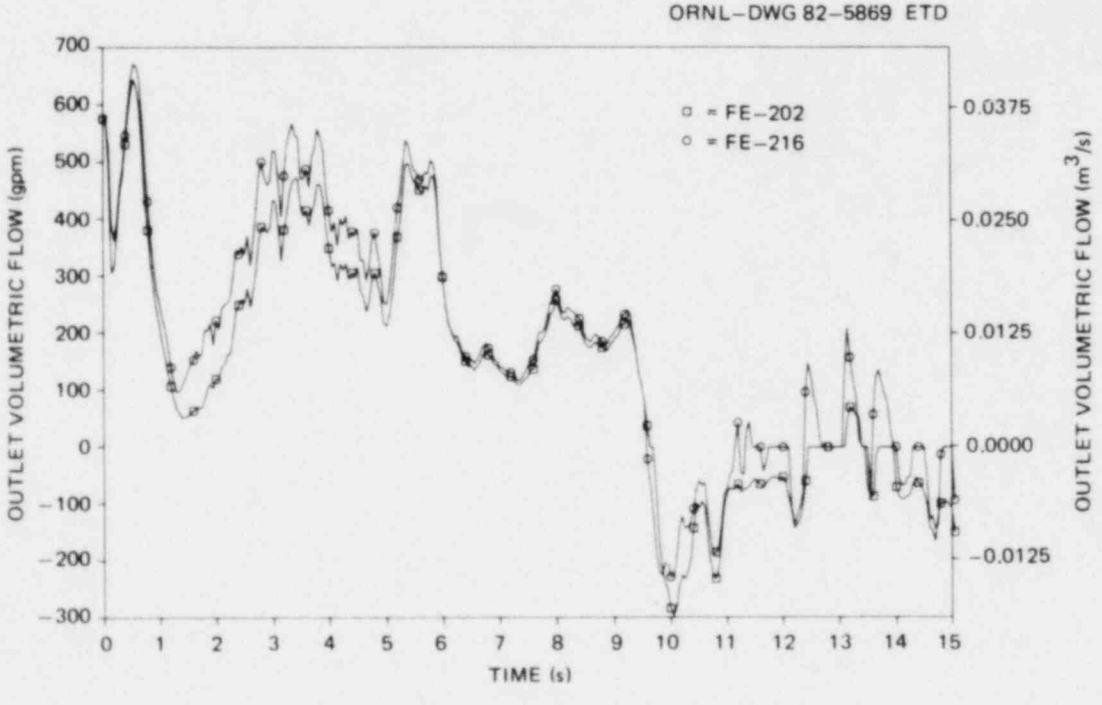

Fig. 2.21. Instrument responses from THTF Test 3.05.5B – outlet spool-piece volumetric flow.

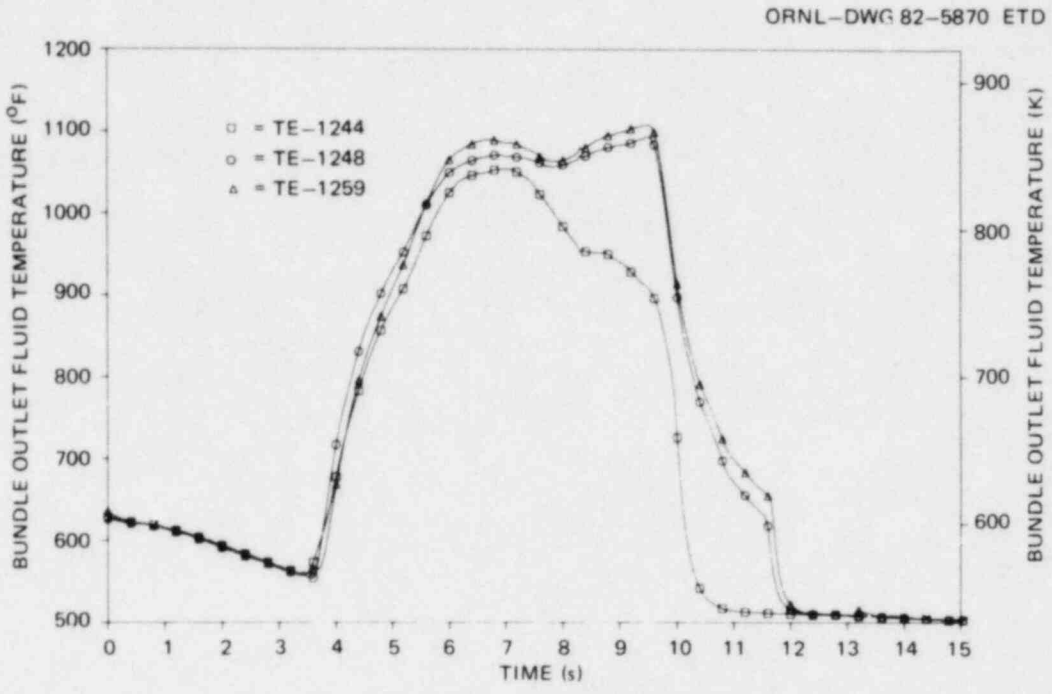

Fig. 2.22. Instrument responses from TF Test 3.05.5B – fluid temperatures as measured by thermocouples located 2.54 cm (1 in.) beyond end of heated length in bundle subchannels 44 (square), 48 (octagon), and 59 (triangle).

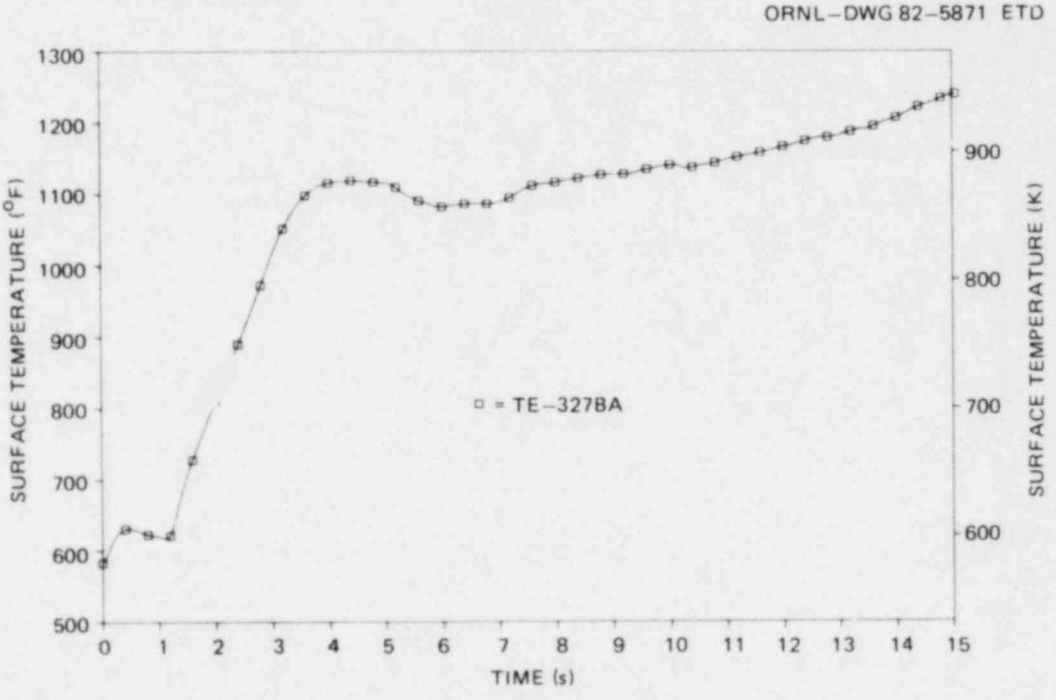

Fig. 2.23. Experimentally determined FRS surface temperature from axial level A.

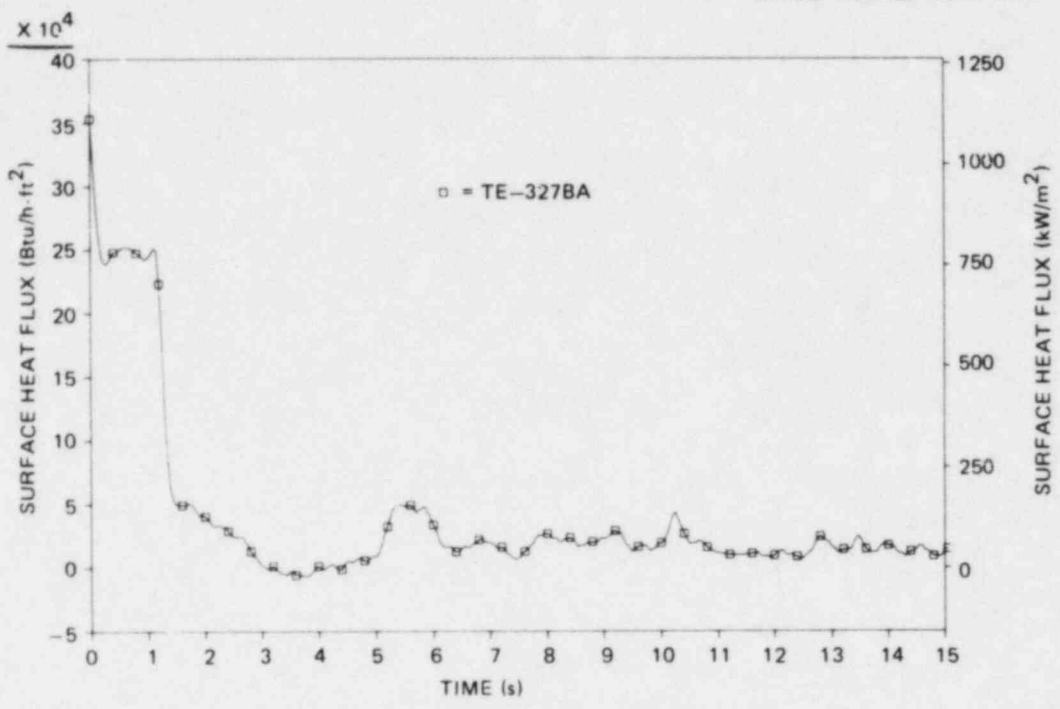

Fig. 2.24. Experimentally determined FRS surface heat flux from axial level A.

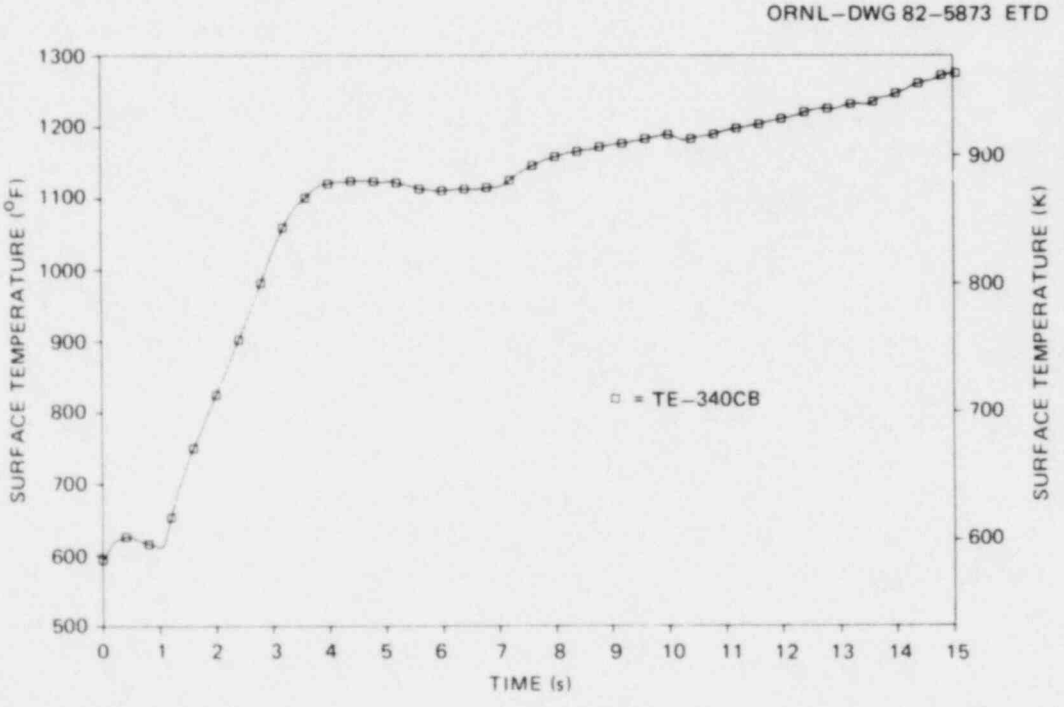

Fig. 2.25. Experimentally determined FRS surface temperature from axial level B.

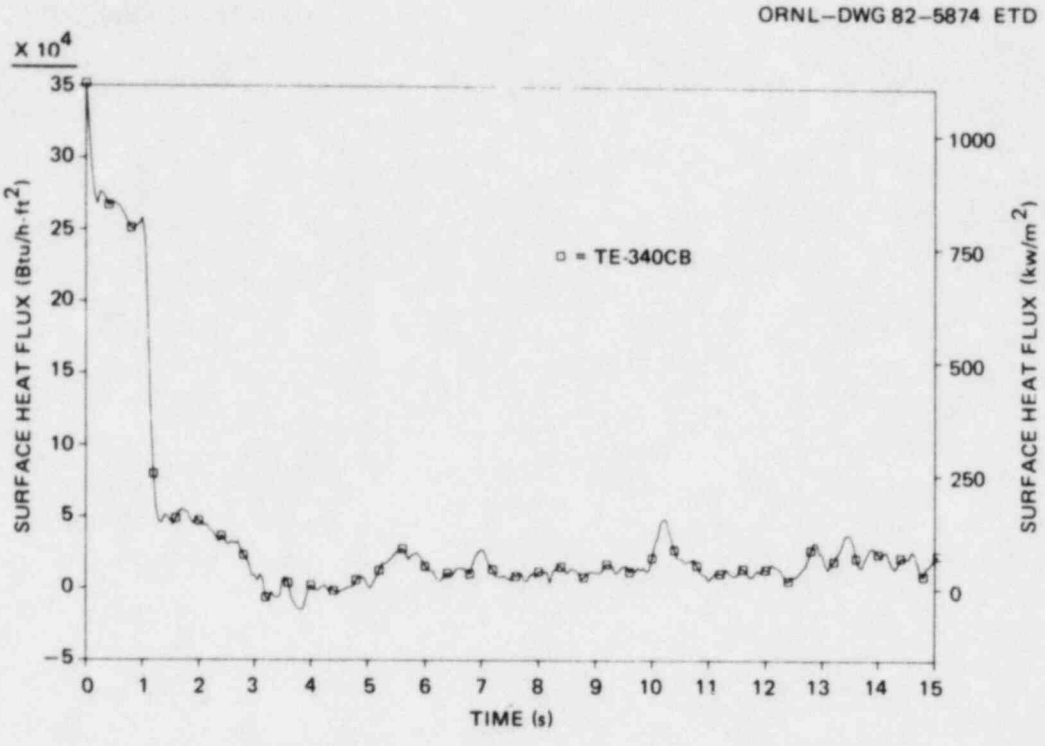

Fig. 2.26. Experimentally determined FRS surface heat flux from axial level B.

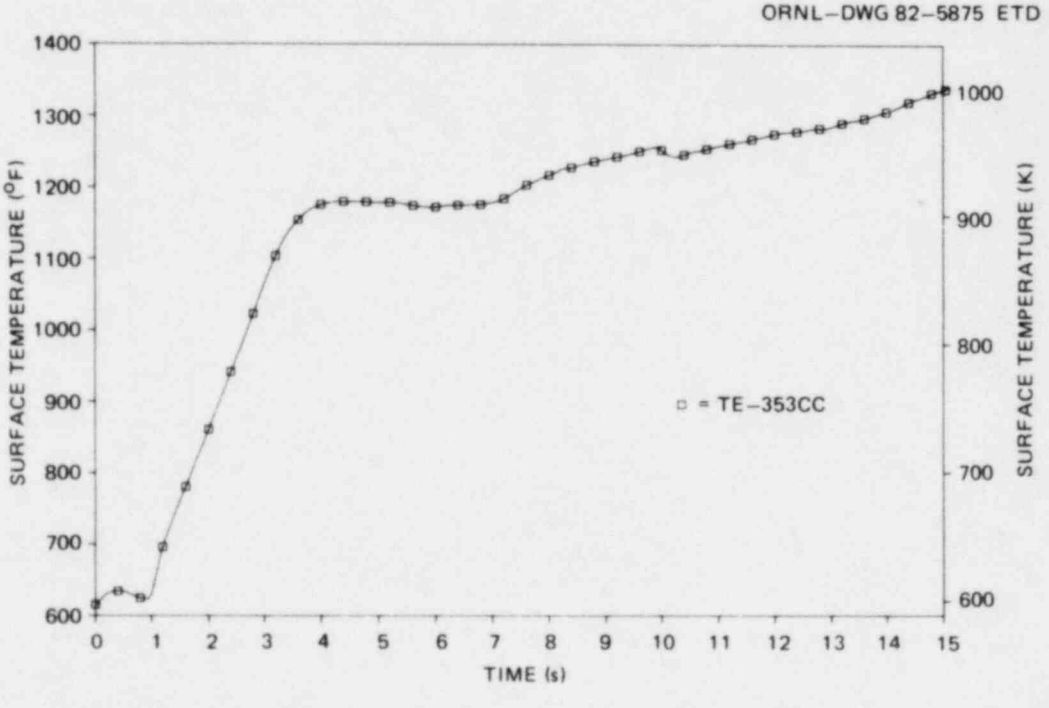

Fig. 2.27. Experimentally determined FRS surface temperature from axial level C.

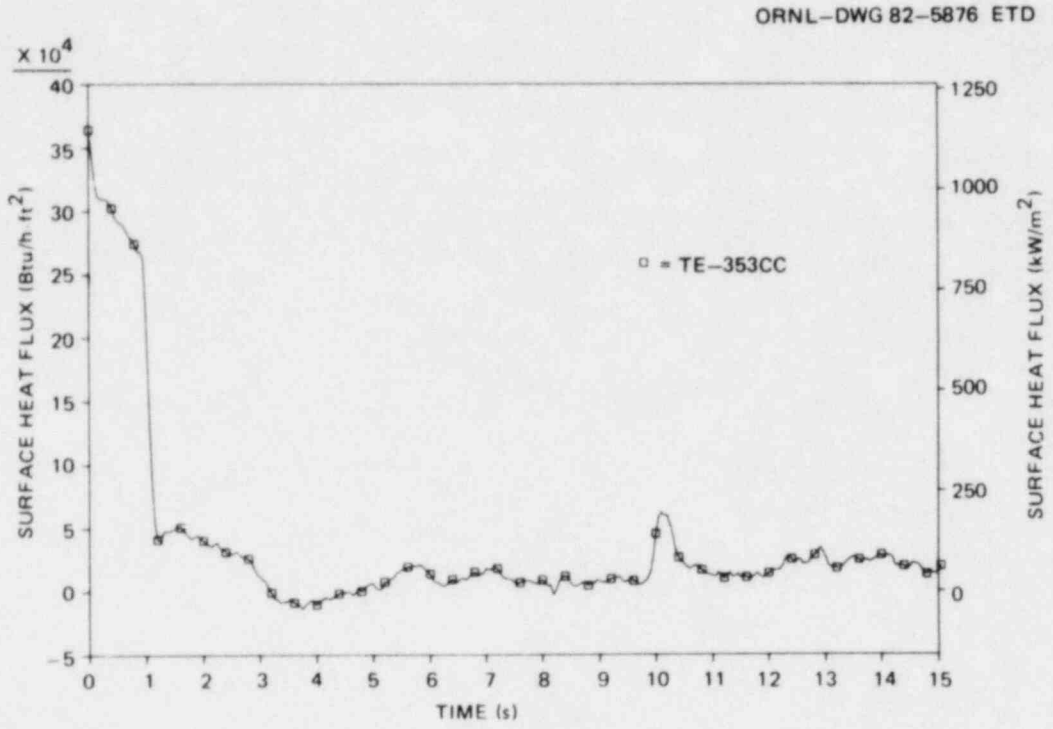

Fig. 2.28. Experimentally determined FRS surface heat flux from axial level C.

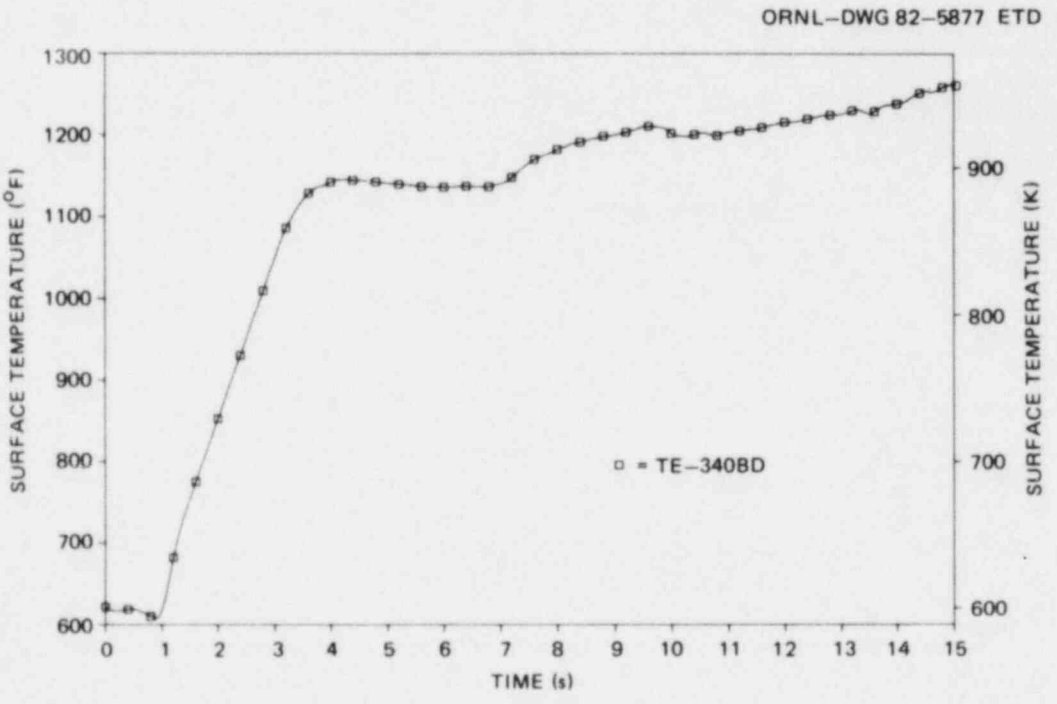

Fig. 2.29. Experimentally determined FRS surface temperature from axial level D.

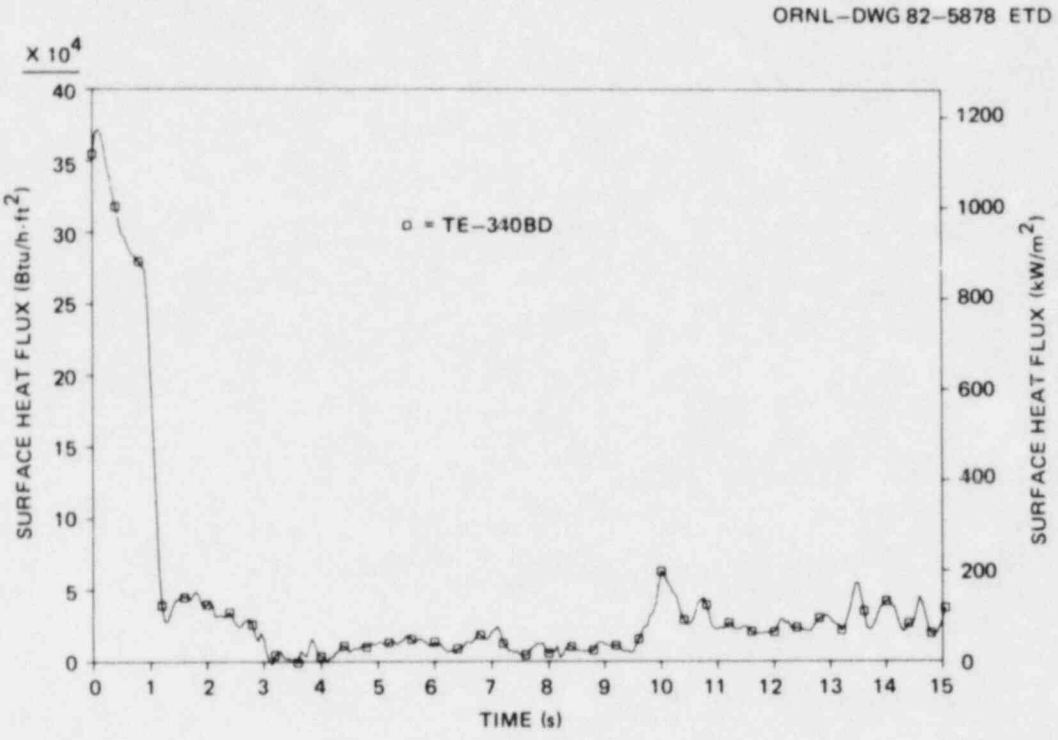

Fig. 2.30. Experimentally determined FRS surface heat flux from axial level D.

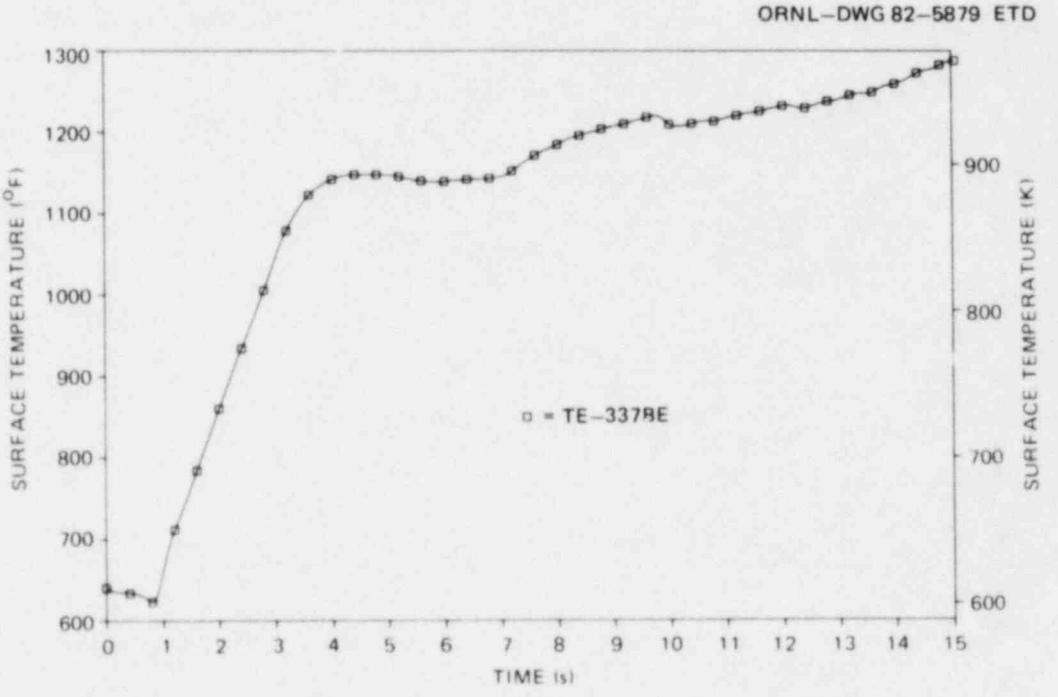

Fig. 2.31. Experimentally determined FRS surface temperature from axial level E.

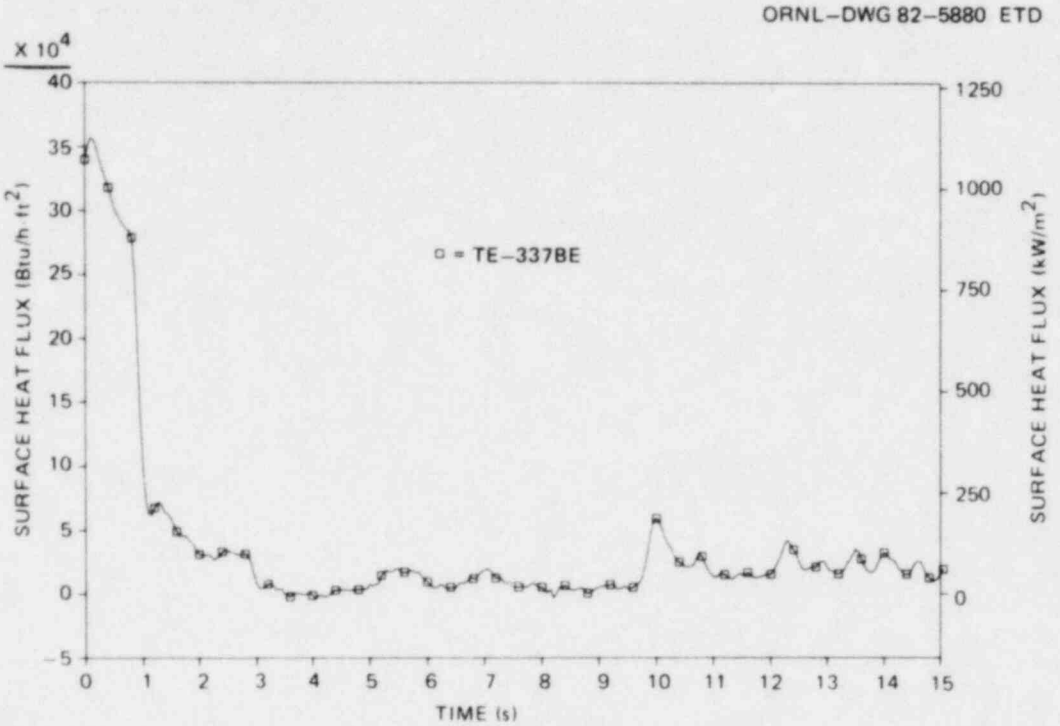

Fig. 2.32. Experimentally determined FRS surface heat flux from axial level E.

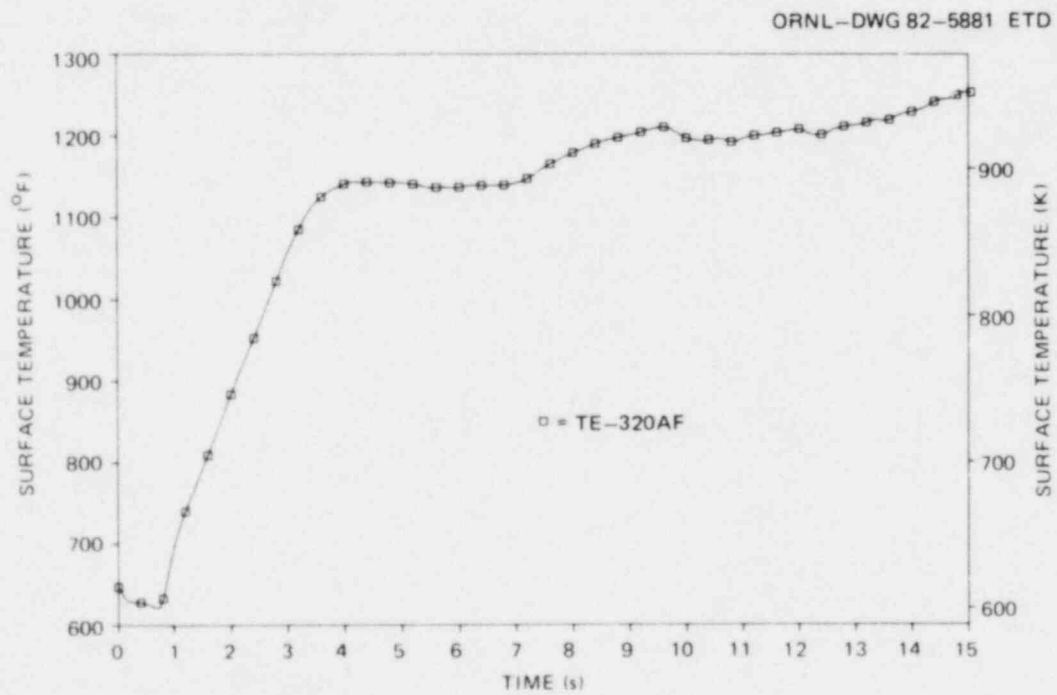

Fig. 2.33. Experimentally determined FRS surface temperature from axial level F.

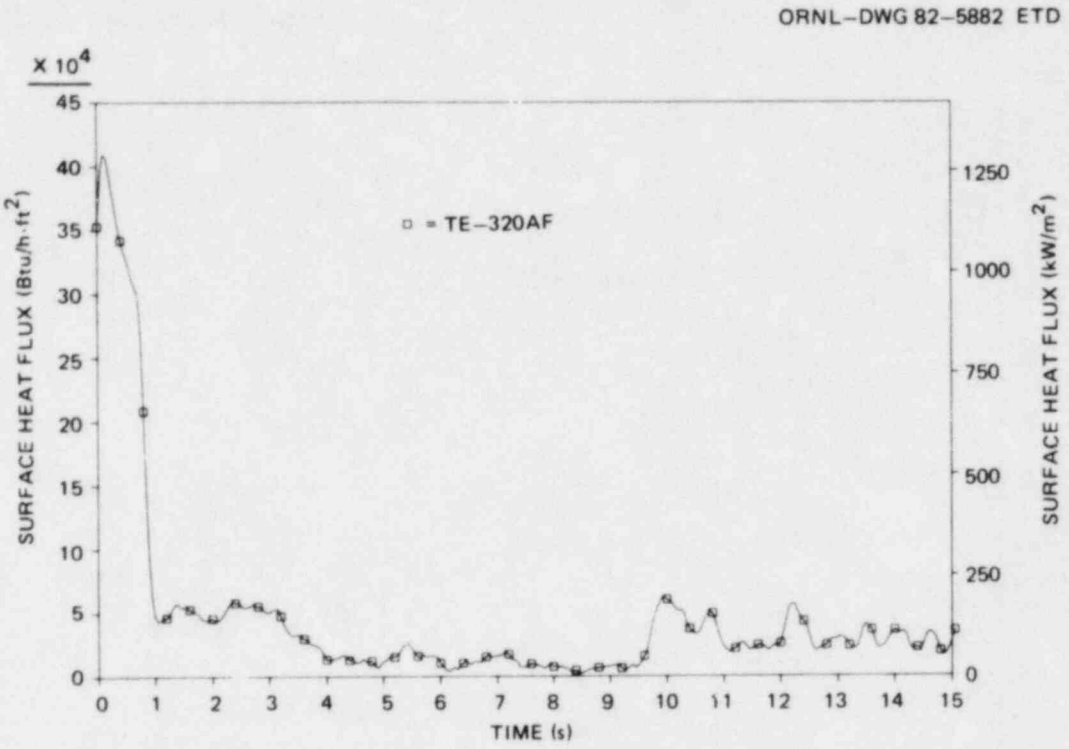

Fig. 2.34. Experimentally determined FRS surface heat flux from axial level F.

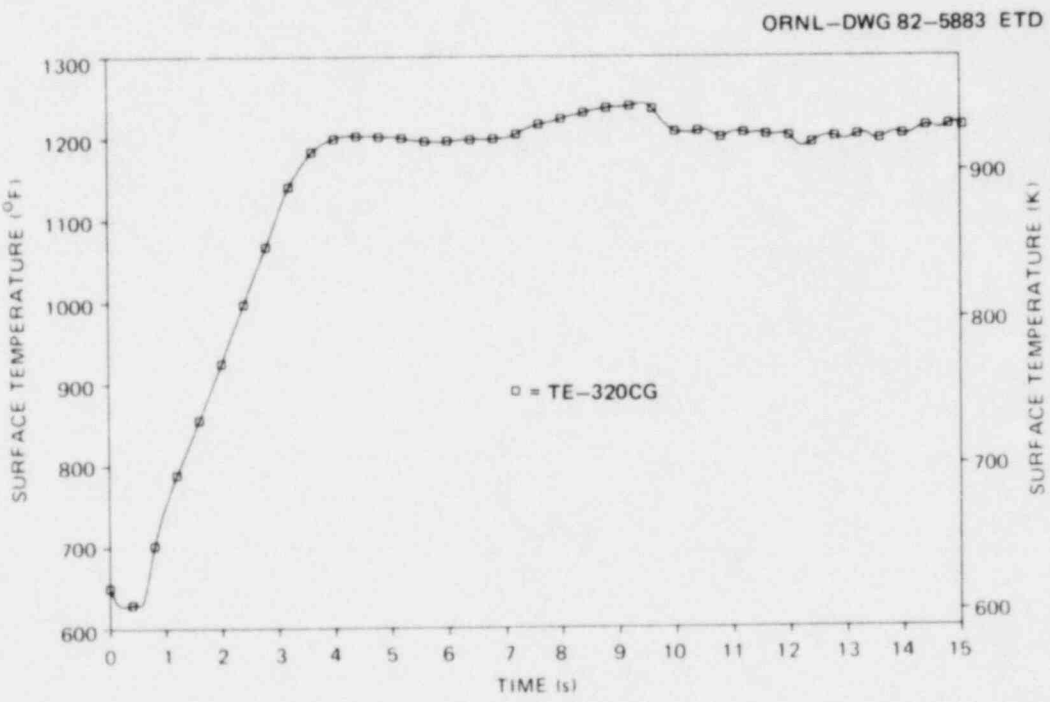

Fig. 2.35. Experimentally determined FRS surface temperature for axial level G.

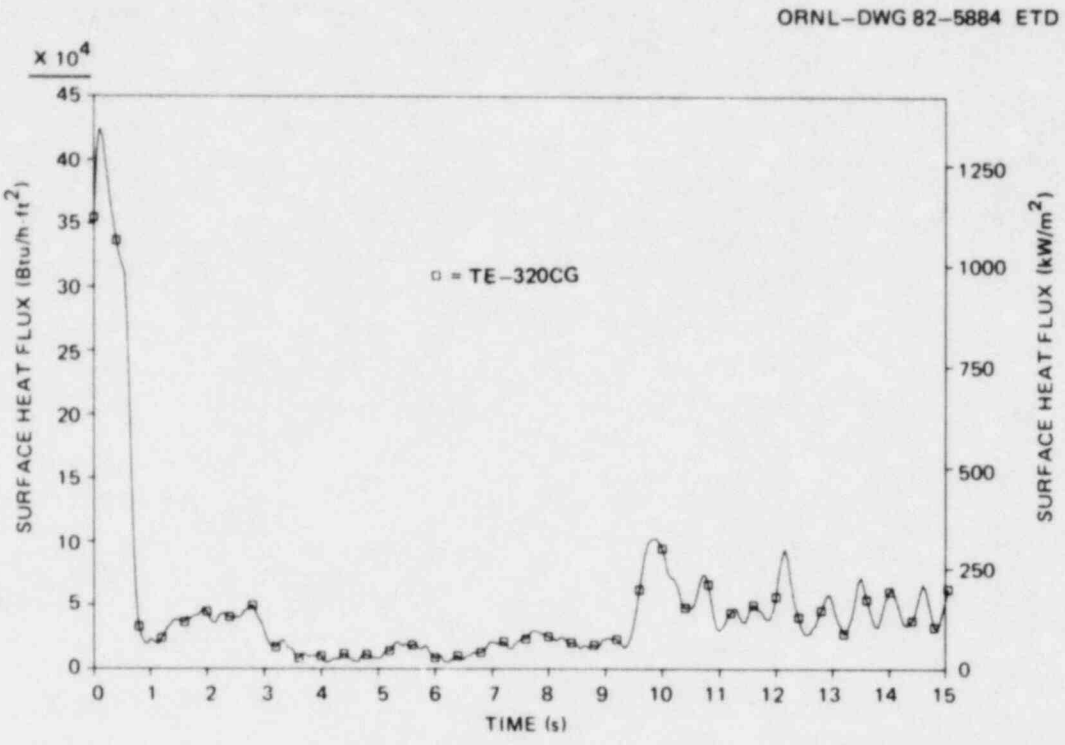

Fig. 2.36. Experimentally determined FRS surface heat flux for axial level G.

3. BACK CALCULATION

3.1 Concept

This report presents two approaches to answering the question of how well the electric FRSs in the THTF simulated the behavior of nuclear fuel rods exposed to the same hydrodynamic environment. One of these approaches, referred to as the forward calculation, is described in Chap. 4; this chapter describes an alternate technique, referred to as a back calculation. The back calculation determines the power that must have been generated in the nuclear fuel rod in order for it to experience the same surface temperature and surface heat flux transient as the electric FRS. The variation of power with time that would occur in a nuclear reactor during a DECLB can be calculated in a fairly straightforward manner, assuming that reactor scram occurs on break initiation. Comparing the expected transient power for an actual nuclear reactor accident with the power produced by the back calculation will provide a means of assessing whether the surface temperature and surface heat flux experienced by the electric FRS could have represented the surface heat flux and surface temperature that would have been experienced by the nuclear fuel rod. If the power produced by the back calculation is totally unrealistic, this would indicate that a nuclear fuel rod could not have experienced the surface temperature and surface heat flux transients that were experienced by the electric FRSs.

The precise means by which the back calculation is performed is described in Appendix A. Neither existence nor uniqueness theorems exist for this type of problem. As formulated and solved by PINSIM, this problem is extremely ill-conditioned. Minor fluctuations in the surface flux or surface temperature produce extreme fluctuations in the calculated power; however, this problem has not proved insurmountable. When the power produced by the back calculation is smoothed, a reasonable result is obtained. This has been verified by performing a back calculation using a model of the electric FRS and supplying it with the temperature and heat flux determined from the experimental measurements. When the power produced by this back calculation was smoothed, the power program that was

actually supplied during the experiment was produced. Validation studies for both the back- and forward-calculational capabilities of the PINSIM code have been performed and are documented.[11]

3.2 Results

At each axial level, an FRS sheath thermocouple was selected whose behavior was representative of all the thermocouples at that level. The surface heat flux and surface temperature calculated by ORINC for these thermocouples were used as boundary conditions in back calculations using three nuclear fuel rod models. The differences in these models were in the size of the gas gap. One model, referred to as the nominal-gap model, had a gas gap of 0.01 cm (0.004 in.); one model had no gas gap; and one model had a wide gap, twice as large as the nominal gap. The use of three models of varying gap sizes allows one to determine if the results are dependent on the size of the pellet-to-clad thermal resistance. Other than that caused by the gas gap, no thermal resistance (i.e., no contact resistance) is used between the fuel pellet and the cladding; the intent is to determine the effect of the variation in the pellet-to-clad thermal resistance, and this can be done with the range of gap sizes.

The method selected to present the results of the calculations was to smooth the calculated power and then integrate it over time. Graphs are presented that show the integrated power as a function of time. The graphs also contain a reference integrated power curve for comparative purposes. The reference curve was obtained by integrating the power calculated by RELAP4 Mod 5 Update 2 in a prediction of a DECLB. This is the same calculation (described in Sect. 2.2) that was used to plan the experiment. Thus, the question of interest is how closely the integrated "back power" for each nuclear fuel rod model follows the integrated reference power curve.

The results of the calculations for each thermocouple level are shown in Figs. 3.1-3.7. Each figure contains two graphs; one shows the results of the comparisons for 9 s, and one shows the comparisons for the first 3 s only. The latter allows a more detailed examination of the period during which all of the FRSs experience DNB. Note that the character of the

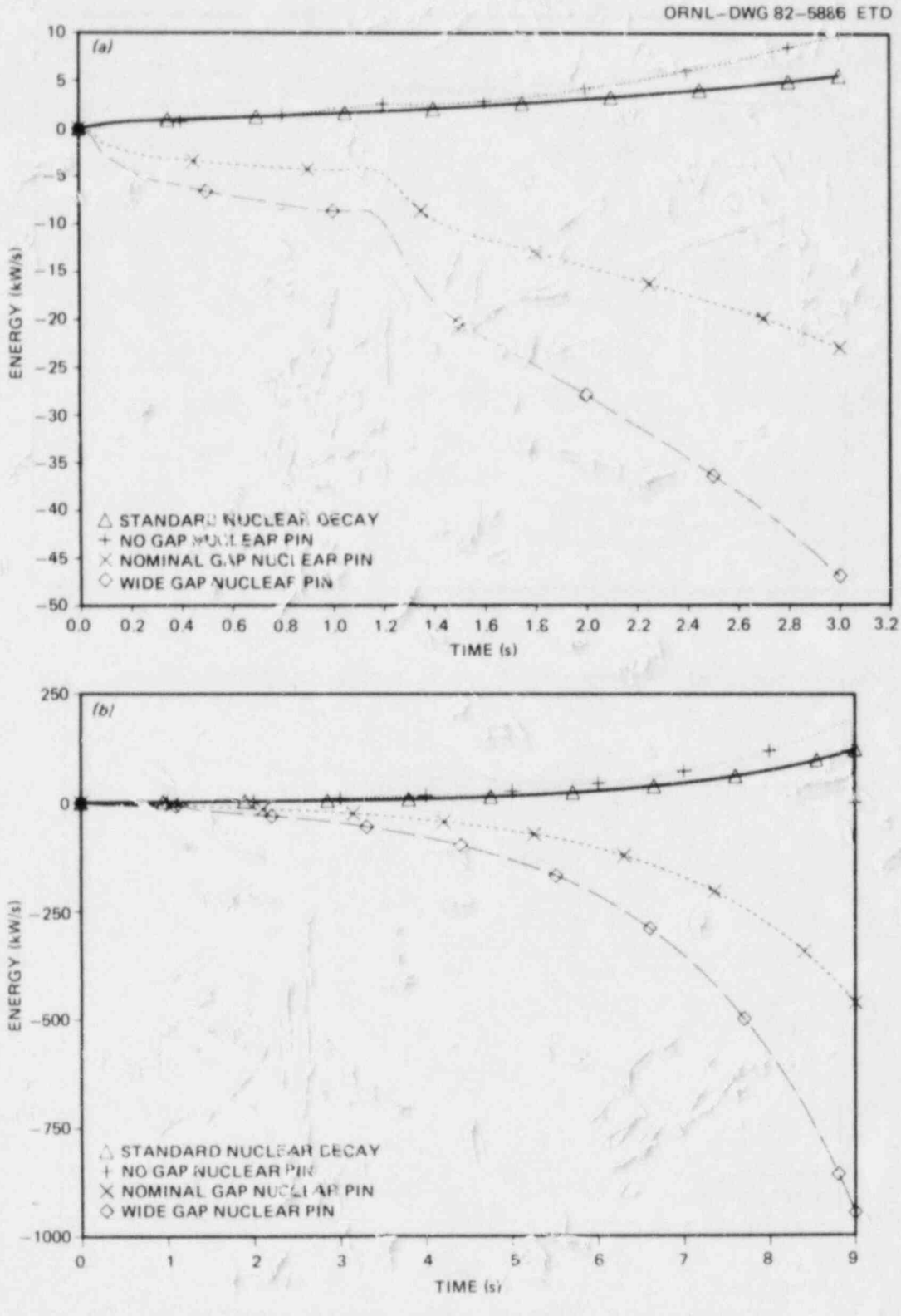

Fig. 3.1. Integrated internal power generation (energy) for axial level A.

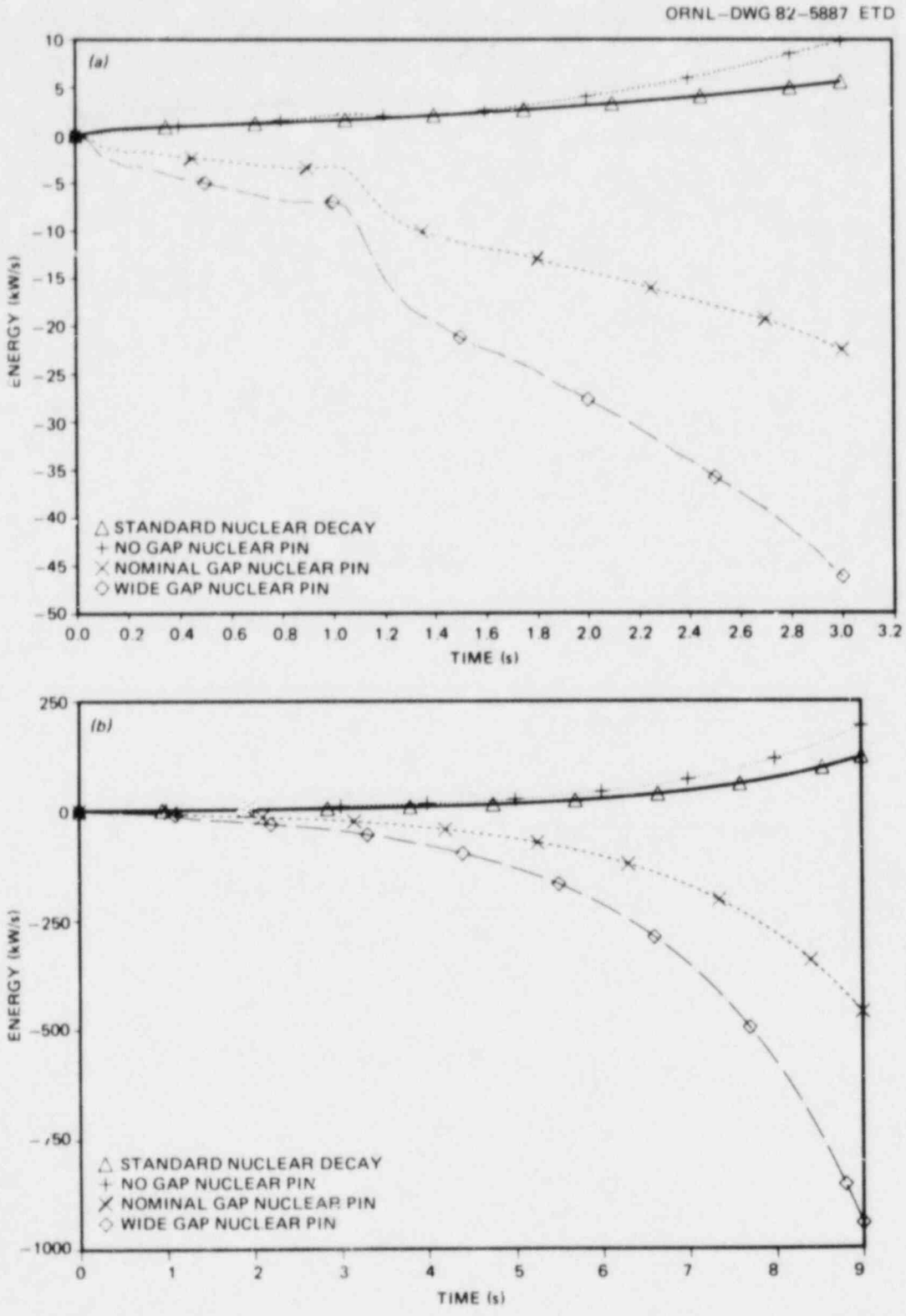

Fig. 3.2. Integrated internal power generation (energy) for axial level B.

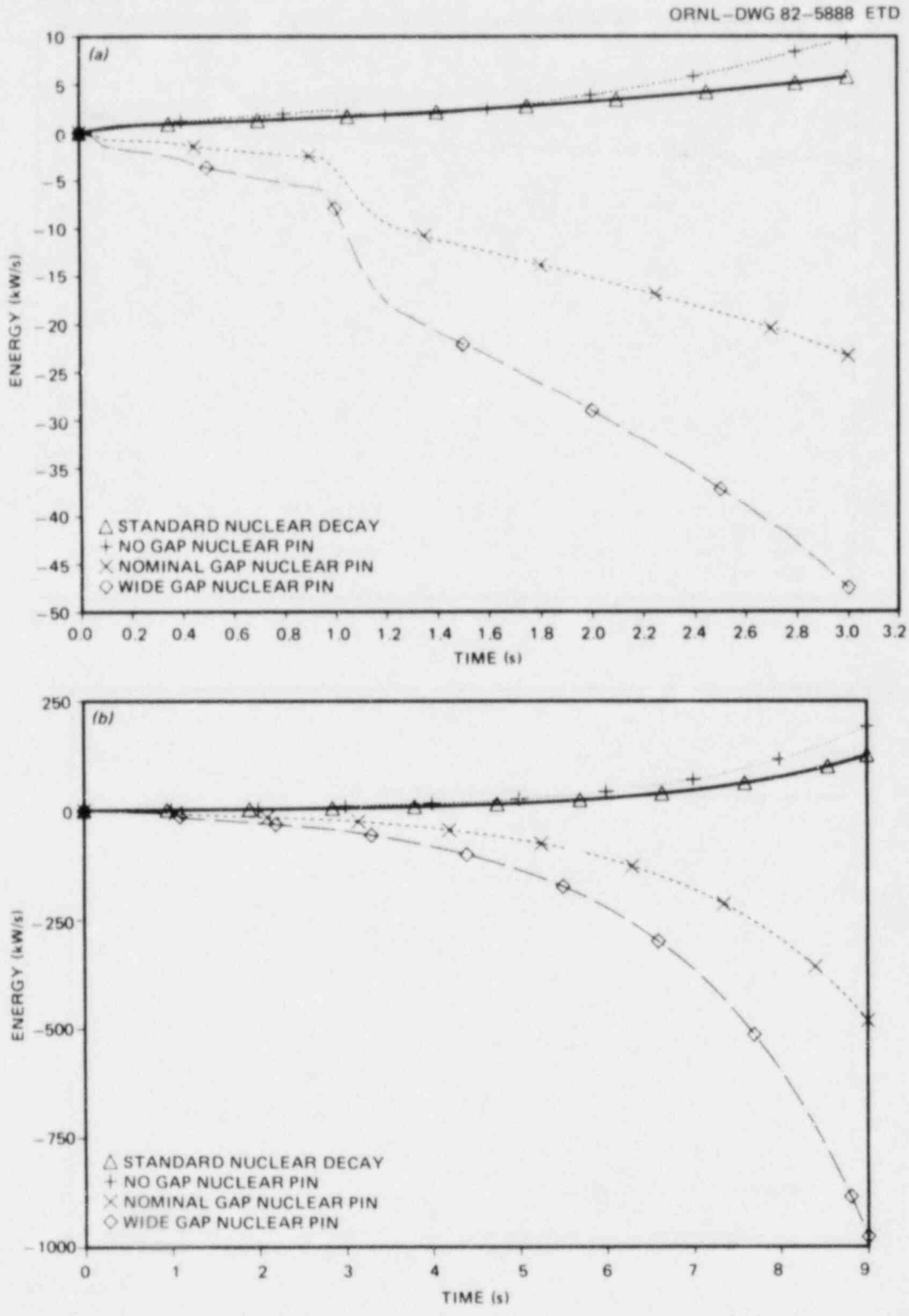

Fig. 3.3. Integrated internal power generation (energy) for axial level C.

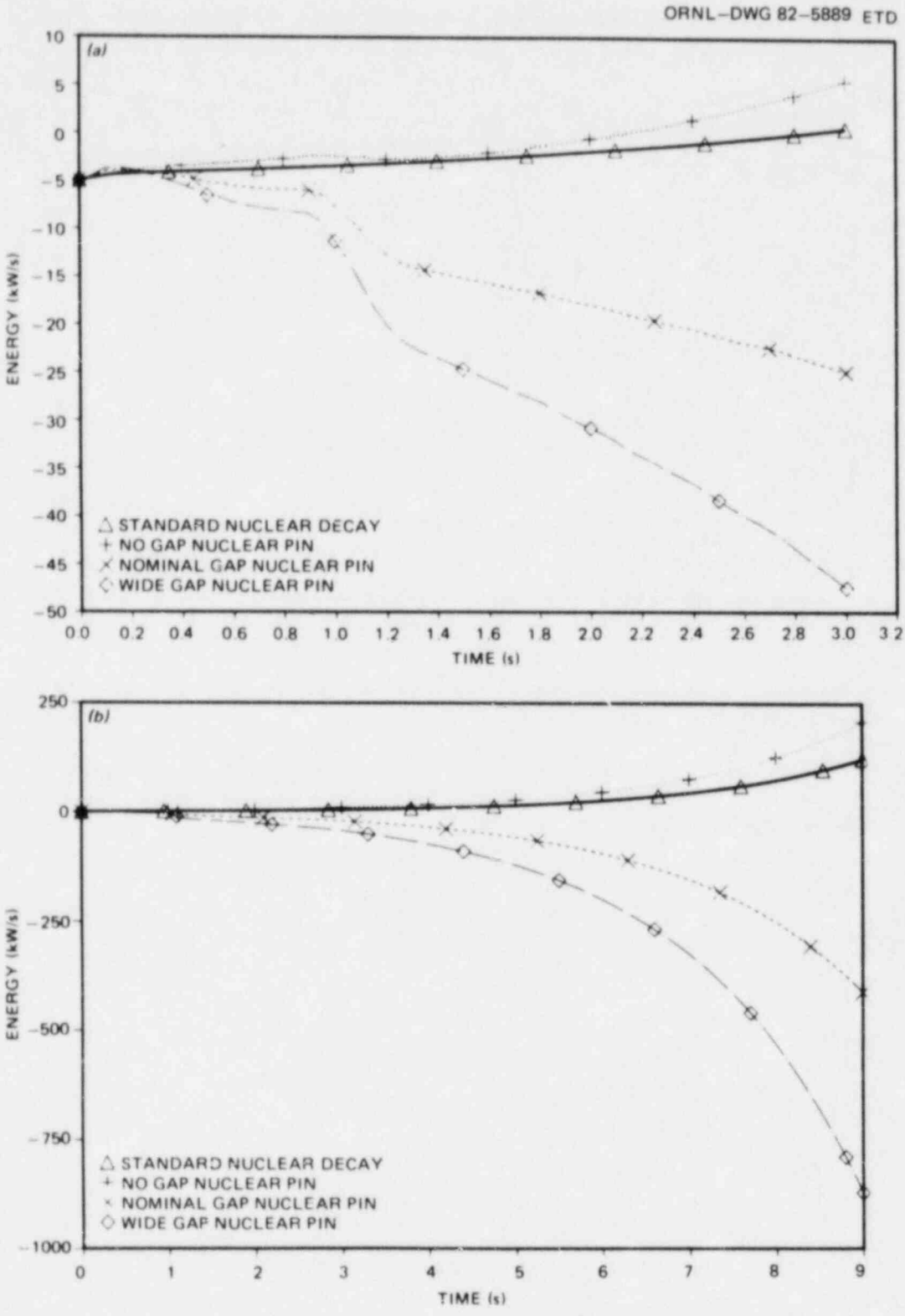

Fig. 3.4. Integrated internal power generation (energy) for axial level D.

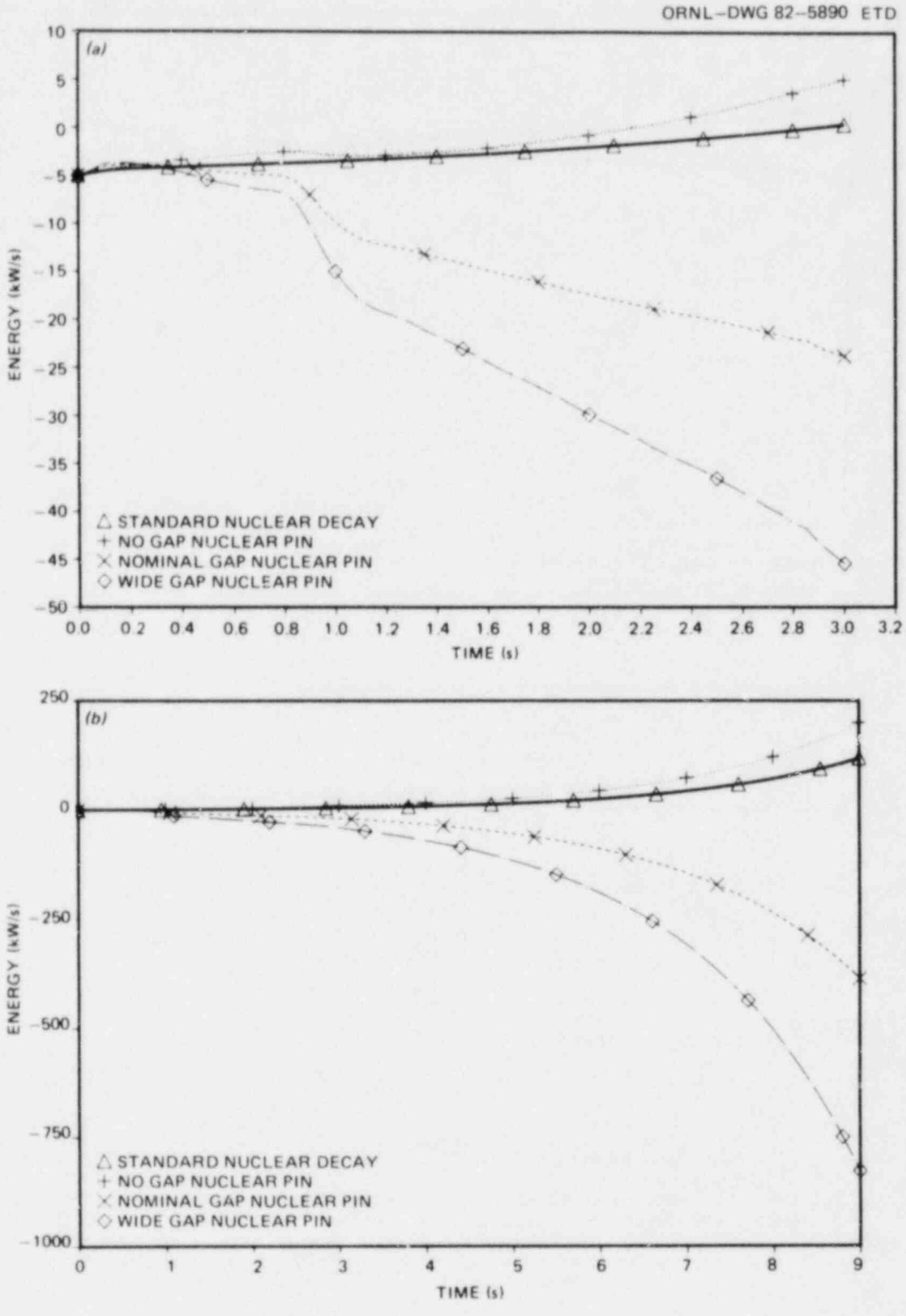

Fig. 3.5. Integrated internal power generation (energy) for axial level E.

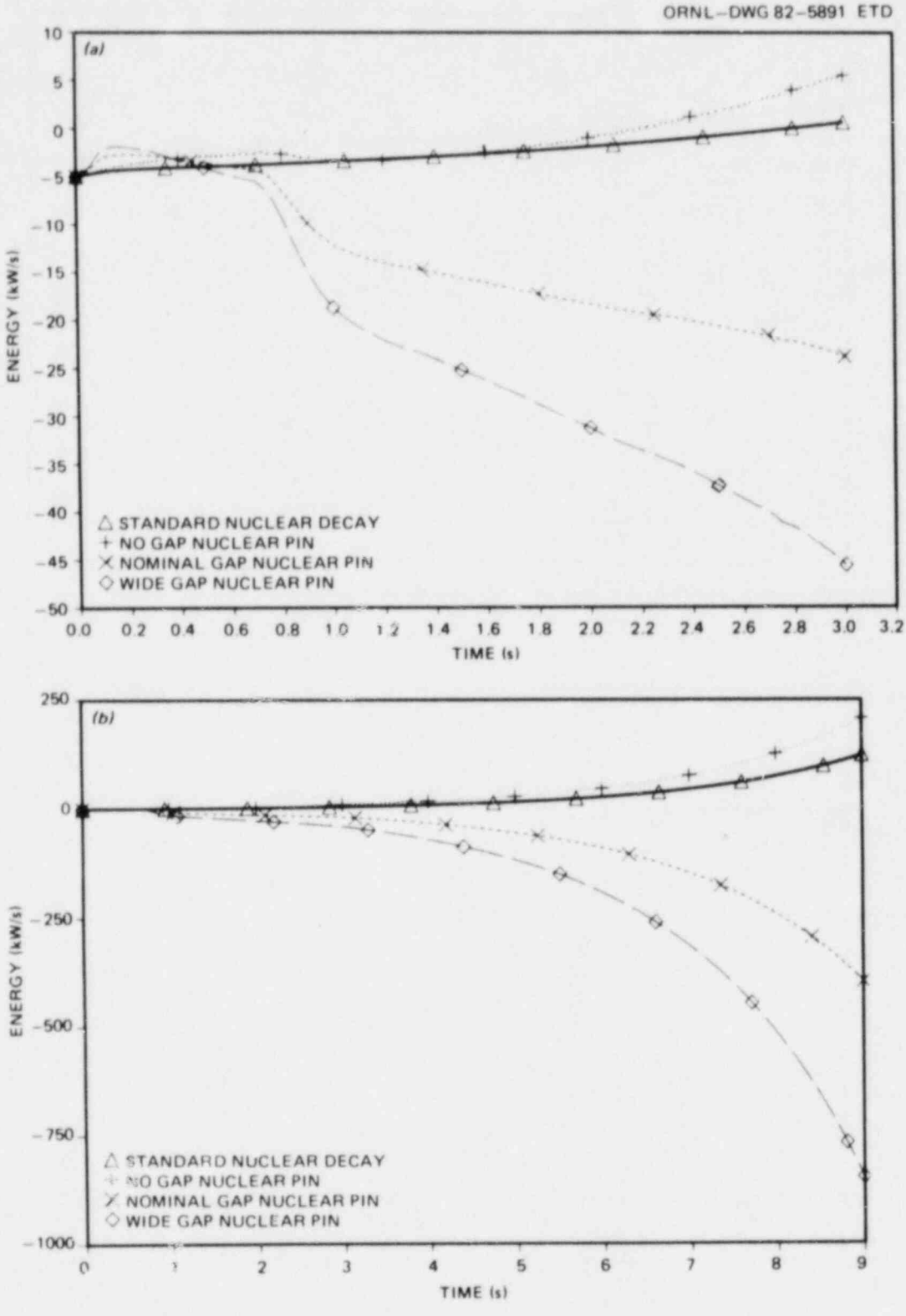

Fig. 3.6. Integrated internal power generation (energy) for axial level F.

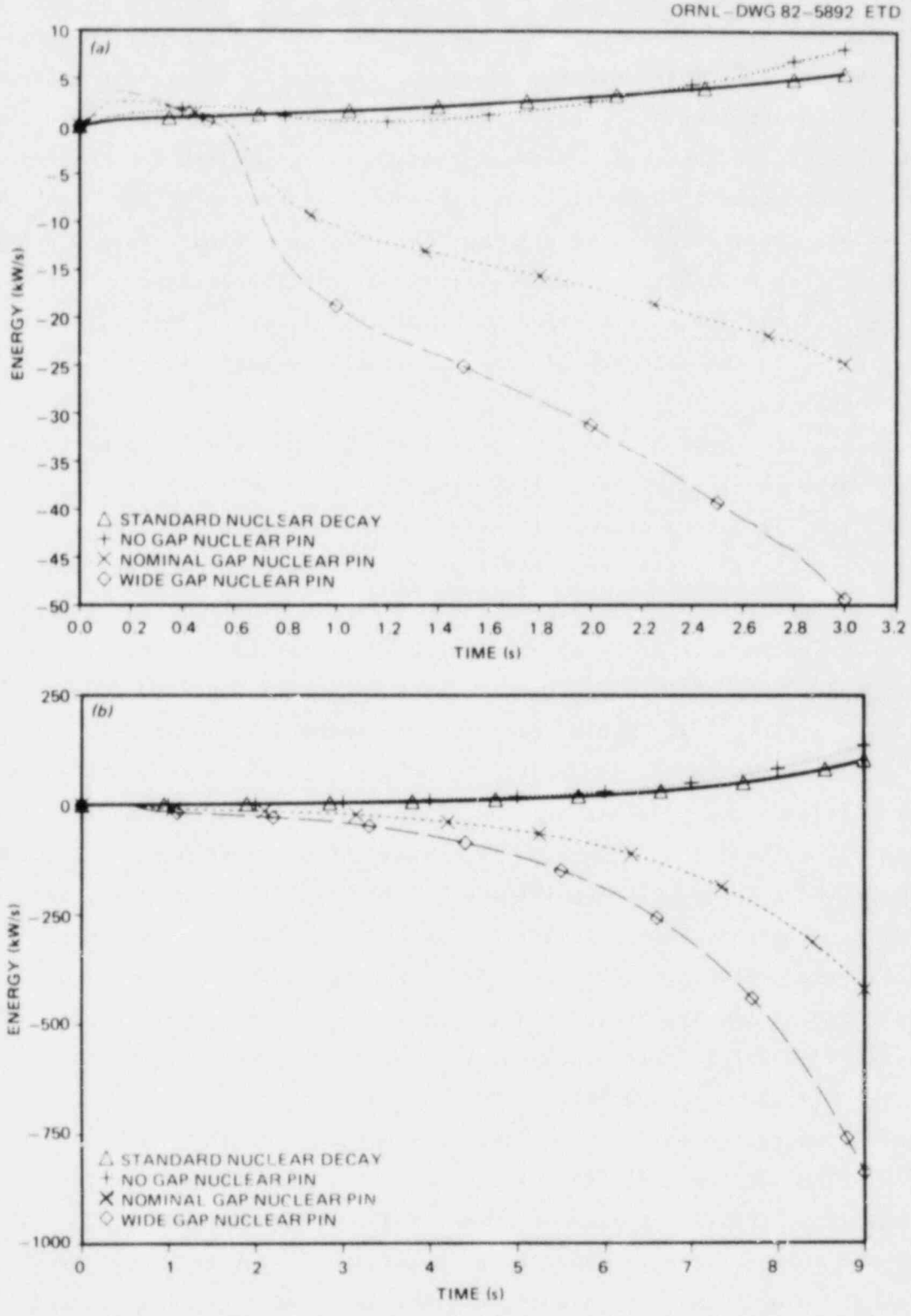

Fig. 3.7. Integrated internal power generation (energy) for axial level G.

reference curve is as expected, a slow, almost linear increase caused by the nuclear fuel's decay heat following scram. Both the nominal- and the wide-gap back-calculated, integrated powers at all levels almost immediately become negative. A negative integrated power means that energy would have had to have been consumed rather than generated by the nuclear fuel. This obviously unphysical result indicates that a nuclear fuel rod with either a nominal or wide gas gap could not have experienced the surface heat flux and surface temperature transients experienced by the electric FRS. Thus, the electric FRS behavior in this experiment did not accurately simulate the behavior of a nuclear fuel rod with either a nominal or wide gas gap.

Only in the case of the no-gap nuclear fuel rod model did the integrated power remain positive. This is a logical result; the absence of a gas gap would reduce substantially the stored energy in the nuclear fuel by lowering the internal temperature profile. Thus, the energy that needed to be removed in the nominal- and wide-gap models is never present in the no-gap model. In fact, in Figs. 3.1-3.7 the no-gap model's integrated power appears fairly close to the reference integrated power for most of the first 2 s. These appearances are somewhat deceiving, however, because the scale of the graphs had to be quite large to show the enormous discrepancies of the nominal- and wide-gap models. Thus, substantial discrepancies between the no-gap and reference calculations may still appear small on the graphs. The significance of the apparent similarity between the no-gap and reference calculations is further reduced when one considers that the percentage of nuclear fuel in an actual reactor having no pellet-to-clad thermal resistance is likely to be quite small. The nominal-gap model is more representative of the majority of nuclear fuel rods than is the no-gap model.

In summary, we may conclude that the behavior of the electric FRS in Test 3.05.5B (in terms of its surface heat flux and surface temperature) was not representative of the behavior of a nuclear fuel rod. These calculations do not directly address the question of whether a nuclear fuel rod in the same hydrodynamic environment as existed in the experiment would have experienced DNB earlier or later than the FRS. This question is addressed by the forward calculations described in Chap. 4. The fact

that the integrated power of the nominal- and wide-gap calculations was negative implies that too much energy would exist in the nuclear fuel for the nuclear rods to experience the same surface transients as the FRS. Because this "excess" energy would exist in the nuclear fuel, this suggests that the surface heat flux of such a nuclear fuel rod would be higher than that experienced by an FRS. This speculation is confirmed in Chap. 4.

4. FORWARD CALCULATION

4.1 Concept

The forward calculation is another means of attempting to answer the question of how a nuclear fuel rod would have behaved if exposed to the same hydrodynamic environment that existed during the experiment. In general, the determination of the hydrodynamic conditions that existed within the rod bundle during a test such as this one is extremely difficult. However, one quantity may be determined with considerable precision. The saturation temperature can be determined from state searches using the measured pressure. Because pressure can be measured accurately, the saturation temperature can be determined accurately. Combining the saturation temperature with experimentally determined FRS surface temperature and surface heat flux, one can calculate an experimental value for the heat transfer coefficient h. Using a calculational model of a nuclear fuel rod and a power curve determined from a standard nuclear kinetics calculation, one can solve the conduction equation in a standard ("forward") manner using the experimental values of h and the saturation temperature as boundary conditions. One can then compare the calculated values for the nuclear surface temperature and nuclear surface heat flux to the actual surface heat flux and surface temperature experienced by the electric FRSs.

In general, a gas gap will exist in a nuclear fuel rod between the fuel pellets and the cladding. Because the results of the forward calculation are sensitive to the size of the gap and because the precise size of the gap for any particular fuel rod in a given reactor at any point during its life is uncertain, three nuclear fuel rod models were used in the forward calculations. One fuel rod model contained a nominal gap of .010 cm (0.004 in.). A second fuel rod model contained no gas gap, and a third fuel rod model contained a gap twice as large as the original gap. If the results of the calculations for all three nuclear fuel rod models bear a consistent relationship to the experimental behavior of the electric FRSs, then conclusions about the relative behavior of nuclear fuel rods and electric FRSs in a particular case may be drawn independent of details of the gas gap.

A principal objective of Test 3.05.5B was to gain information about time to DNB in an environment similar to that of a reactor accident. Forward calculations in some cases may be used to directly address the relationship of time to DNB for electric and nuclear fuel rods exposed to the same environment. Such analyses rely on certain assumptions about the mechanism that produces DNB. Many reactor analysis codes determine when a rod departs from nucleate boiling by using a correlation to predict the critical heat flux (CHF) and assuming that DNB occurs when the rod's surface heat flux exceeds the CHF. A variety of correlations, often giving contradictory results, exist for predicting the CHF, given the bundle fluid conditions. In general, the conditions in the test section during the first few seconds of Test 3.05.5B may be characterized as being of increasing void fraction and decreasing flow. Under such conditions, most correlations would predict that the CHF decreases with time. Consider a specific location on a specific rod in Test 5B (Fig. 2.24). At one moment in time, we know the approximate value of the CHF for this specific location on this specific rod (1.20 s in Fig. 2.24). Because the rod departs from nucleate boiling at this time, we may assume that the rod heat flux just prior to departure is approximately equal to the value of the CHF.

Suppose that the experimentally determined surface heat flux for an electric FRS is given by the curve labeled "Pin 1" in Fig. 4.1. Suppose further that the results of a forward calculation on a nuclear pin model produce the results labeled as "Pin 2" in this figure. If we then assume that the CHF has a generally negative slope and intersects the curve of Pin 1 at the point shown, we may then conclude that a nuclear fuel rod in the same environment would have departed from nucleate boiling later than the electric FRS because its flux just prior to DNB is lower than the electric pin model. Conversely, if the electric pin flux was as shown on the curve labeled "Pin 2" and the nuclear heat flux produced by the forward calculation was as shown by the curve labeled "Pin 1," we would conclude that the nuclear fuel rod would have experienced DNB earlier than the FRS. How much earlier or later the nuclear fuel rod would have experienced DNB compared with the electric FRS would depend on the precise slope of the CHF curve, which is unknown.

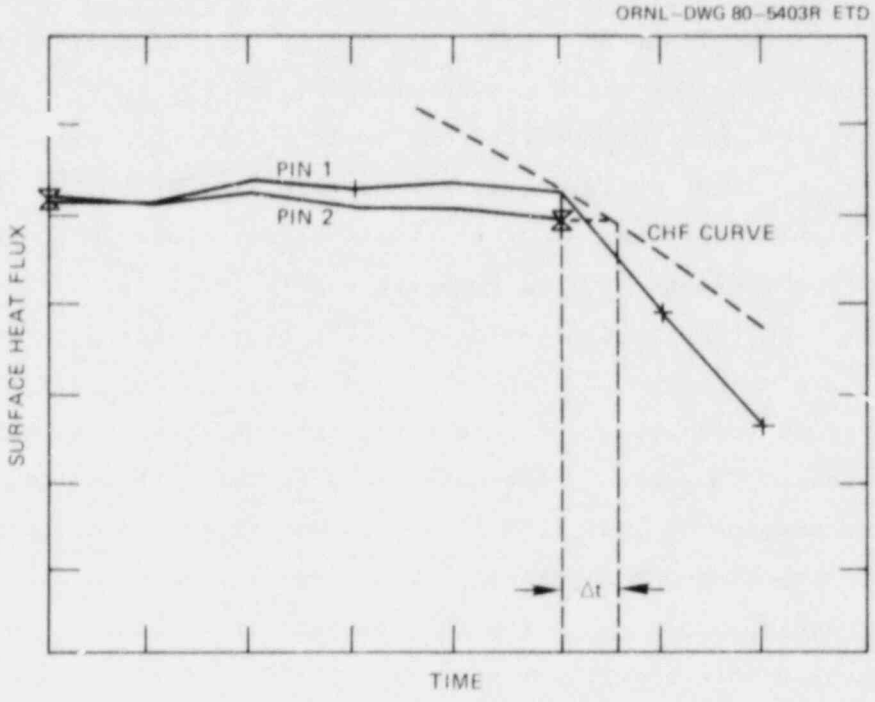

Fig. 4.1. Illustration of relationship between a difference in surface heat flux at a specific time and the difference in time to DNB.

The forward calculations are performed with three nuclear fuel rod models having gas gaps of varying sizes. If the heat fluxes calculated for the nuclear fuel rod models "straddle" the heat flux from the electric FRS, then the question of whether the nuclear rod would have experienced DNB earlier or later would depend on the details of the gas gap size for any particular nuclear fuel rod.

It is enlightening to consider in more detail the assumptions being made in this analysis. It is assumed that any rod exposed to the same hydrodynamic environment as the FRS would experience the same heat transfer coefficient h as the FRS prior to DNB. Thus, we assume that h depends only on the local fluid conditions. This assumption, while not exact, is believed to be sufficiently accurate for this application; note that the correlations for pre-DNB heat transfer regimes used by most transient, thermal-hydraulic, reactor analysis codes do not use the wall composition, wall surface temperature, or wall surface heat flux. The heat transfer

coefficient is calculated from the experimental data as

$$h = \frac{\text{FRS heat flux}}{(\text{FRS temperature} - \text{saturation temperature})}$$

and is applied to the nuclear models as

surface heat flux = h x (surface temperature − saturation temperature).

Using this definition, the assumption that h does not depend on the wall temperature is probably fairly good for the forced-convection-to-liquid heat transfer regime. For the nucleate boiling regime, obtaining a quantity that does not depend on the wall temperature could be done more accurately by defining h as

$$h = \frac{\text{FRS heat flux}}{(\text{FRS temperature} - \text{saturation temperature})^2}$$

and applying it as

surface heat flux = h x (surface temperature − saturation temperature)^2

However, in a similar analysis performed for an earlier THTF test [see Appendix F, (Ref. 12)], calculations were performed in both ways, and the differences between them were much smaller than the differences between the FRS and nuclear model results. Thus, the procedure used here is suitable for this application. The assumption is also being made that the value of the CHF depends only on the local fluid conditions. Once again, although this probably is not strictly correct, it is a commonly made assumption (e.g., all five CHF correlations available in RELAP4 Mod5 Update 2 depend only on local fluid conditions) and is believed to be a reasonable approximation for this calculation. Given these assumptions, the approach presented here allows one to examine whether a nuclear fuel rod exposed to the same hydrodynamic environment as the FRS would have a longer or shorter time to DNB, through the use of quantities (saturation temperatures and FRS heat fluxes and temperatures) that can be calculated more accurately than those needed to apply various correlations (i.e., the bundle fluid conditions).

4.2 Results

As in the previous chapter, at each axial level (Fig. 2.7) one FRS sheath thermocouple is selected whose behavior is representative of that level. The heat transfer coefficient h is calculated from the ORINC-calculated surface heat flux and surface temperature and the saturation temperature as determined from the measured pressure. Three nuclear fuel rod models (no-gap, nominal-gap, and wide-gap) are supplied with h, the saturation temperature, and a nuclear power decay curve as calculated for a reactor scram by the RELAP4 Mod5 Update 2 model of a DECLB [described in Sect. 2.2 (Fig. 2.11)]. The resulting nuclear-model surface heat fluxes and surface temperatures are then compared with the experimentally determined (by ORINC) FRS surface heat fluxes and surface temperatures.

Three separate cases are considered. In the first case, the nuclear fuel rod models are supplied with the same initial power as the FRS had in the experiment. Thus, differences between the nuclear fuel rod models and FRS behavior are due solely to the differences in the rods themselves. Recall that the axial power profile in the FRS is flat, while in a reactor the axial power profile is a chopped-cosine. This difference provides the motivation for the other two cases. One approach to considering the effects introduced by this difference would be to compare the response of the FRS at a specific axial location with the responses of the nuclear fuel rod models supplied with the initial power that they would have had at the same axial location in a nuclear core. If we had confidence that our experimental fluid conditions closely matched those of an actual reactor accident, this approach would permit us to draw conclusions about how different portions of the nuclear core would behave by comparison with their corresponding portions of the electric rod bundle. In fact, we have no such confidence (this is discussed in more detail in Sect. 4.3). The fluid conditions extant in the lower bundle in the experiment might, for example, be more representative of the upper core than the lower core in a nuclear accident. Therefore, the approach chosen compared the actual FRS response at each location to the responses of nuclear fuel rod models with initial powers at both the highest (center of the core) and the lowest (ends of the core) levels that would be present in a nuclear core. These

comparisons constitute the second and third cases. The values for the high and low powers were chosen after reviewing the data presented in a Westinghouse report on 17 x 17 fuel assemblies.[13] Comparisons using the same initial powers will be presented first (Figs. 4.2–4.15).

Note that DNB is marked by a sharp drop in the FRS surface heat flux. Note also that all of the nuclear models experience a similar drop at the same time. These drops occur because we are using the heat transfer coefficient as seen by the FRS to bound all of the models. Because DNB is marked by a sharp drop in heat transfer coefficient, we are, in effect, forcing all of the models to experience DNB at the same time. The assessment of whether a nuclear fuel rod would have experienced DNB earlier or later than the FRS is based on the value of the CHF, taken to be the value of the FRS heat flux at the moment of DNB. If the nuclear-model surface heat flux at that moment is higher than the CHF, it would have experienced DNB sooner; if it is lower, it would have experienced DNB later. Because we force all of the models to undergo DNB at the same moment, the nuclear-model calculations beyond the time of DNB are of little physical significance. Therefore, Figs. 4.2–4.15 present the calculational results for only the first few seconds of the transient.

The calculational results at all levels are similar. The nominal-gap and wide-gap results show that the nuclear fuel rod surface heat fluxes for these models would have been higher than the FRS surface heat fluxes at the times of DNB, thus implying that they would have experienced DNB sooner than the FRS did in the experiment. The no-gap results indicate that such a nuclear fuel rod would have had a surface heat flux close to but slightly lower than the FRS at the time of DNB, implying a later time to DNB. These results are consistent with the speculations prompted by the results of the previous chapter.

Next, we compare the response of the FRS with that of nuclear fuel rod models exposed to the same fluid conditions as in the experiment (as represented by h and the saturation temperature) but having initial powers characteristic of those at the ends of a nuclear core. Because the results at all axial levels of the FRS were similar, results will only be shown for the bottom, middle, and top. The results of these low-power cases are shown in Figs. 4.16–4.18. Not surprisingly, when DNB occurs the

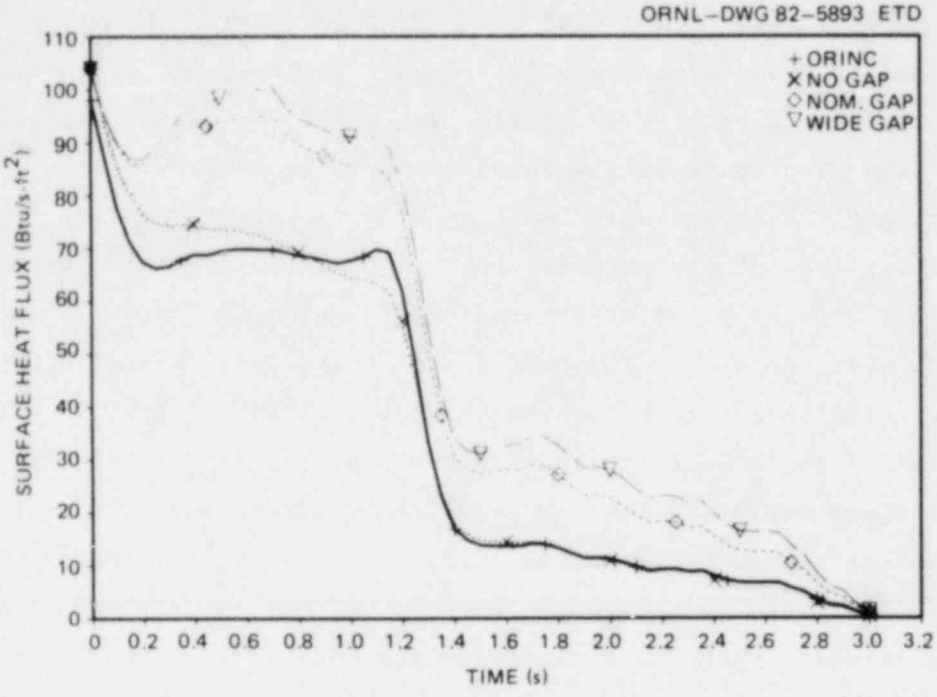

Fig. 4.2. Comparison of surface heat fluxes for FRS (ORINC) and nuclear fuel rod models with different gap sizes – axial level A.

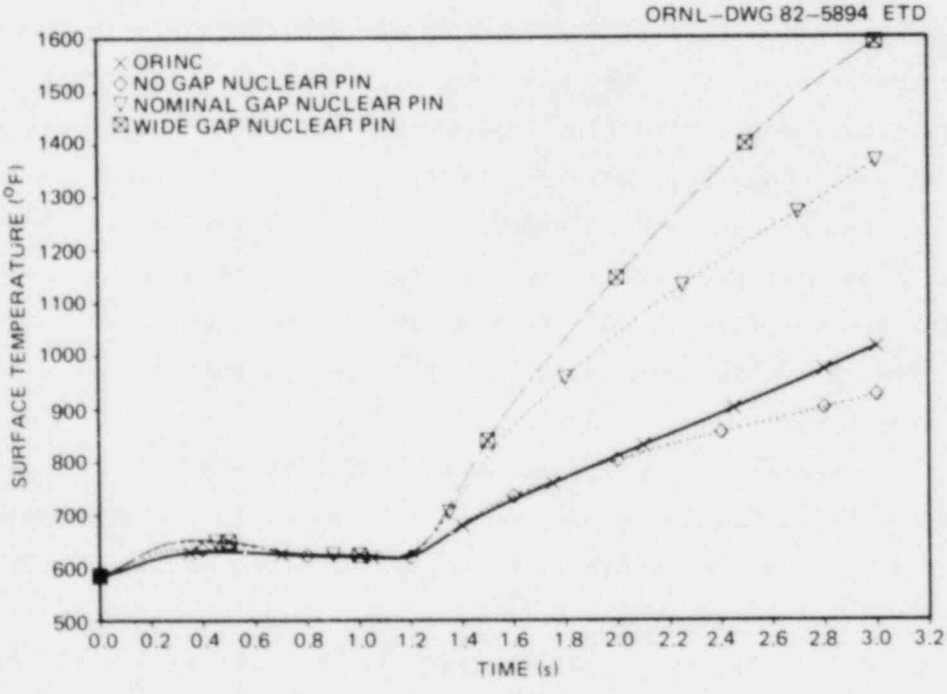

Fig. 4.3. Comparison of surface temperatures for FRS (ORINC) and nuclear fuel rod models with different gap sizes – axial level A.

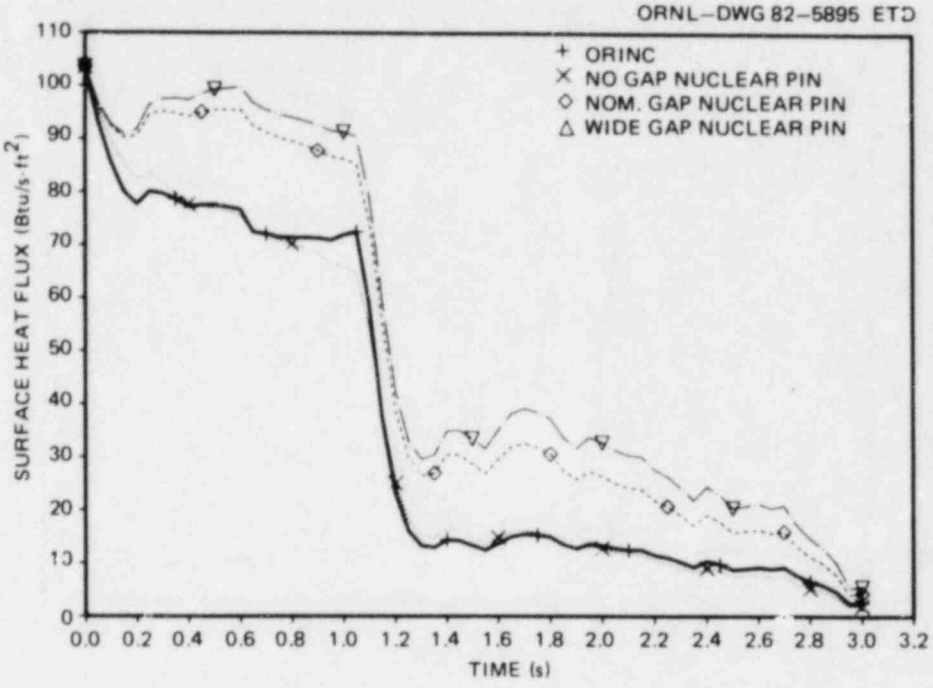

Fig. 4.4. Comparison of surface heat fluxes for FRS (ORINC) and nuclear fuel rod models with different gap sizes – axial level B.

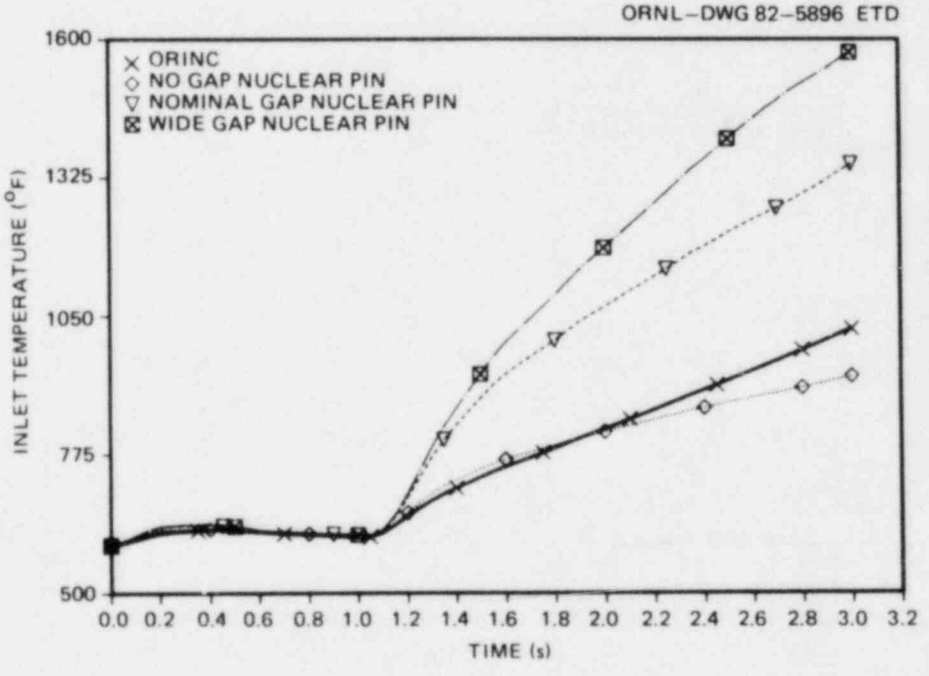

Fig. 4.5. Comparison of surface temperatures for FRS (ORINC) and nuclear fuel rod models with different gap sizes – axial level B.

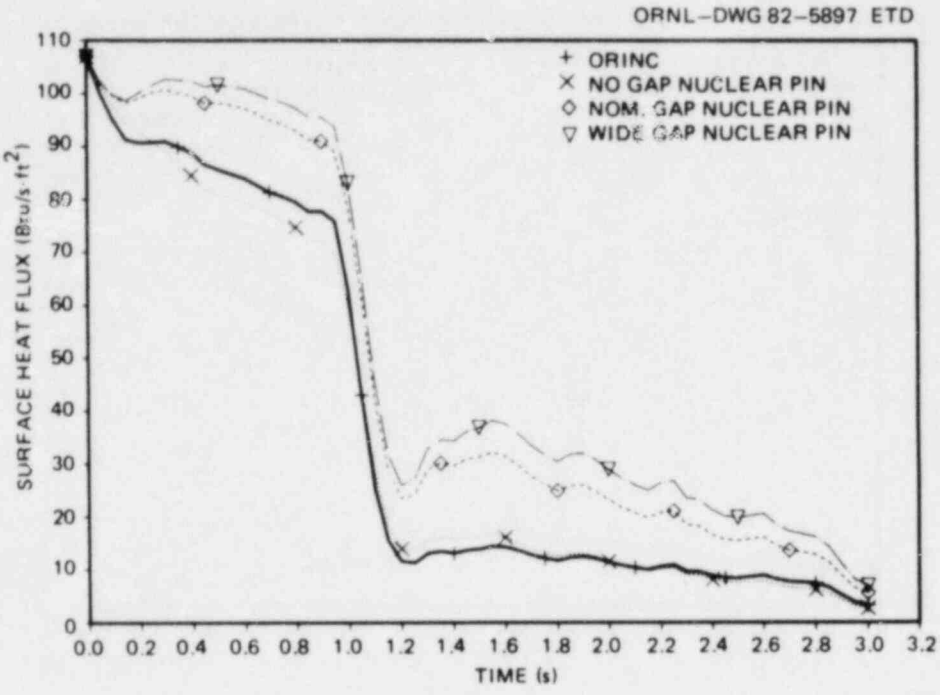

Fig. 4.6. Comparison of surface heat fluxes for FRS (ORINC) for nuclear fuel rod models with different gap sizes – axial level C.

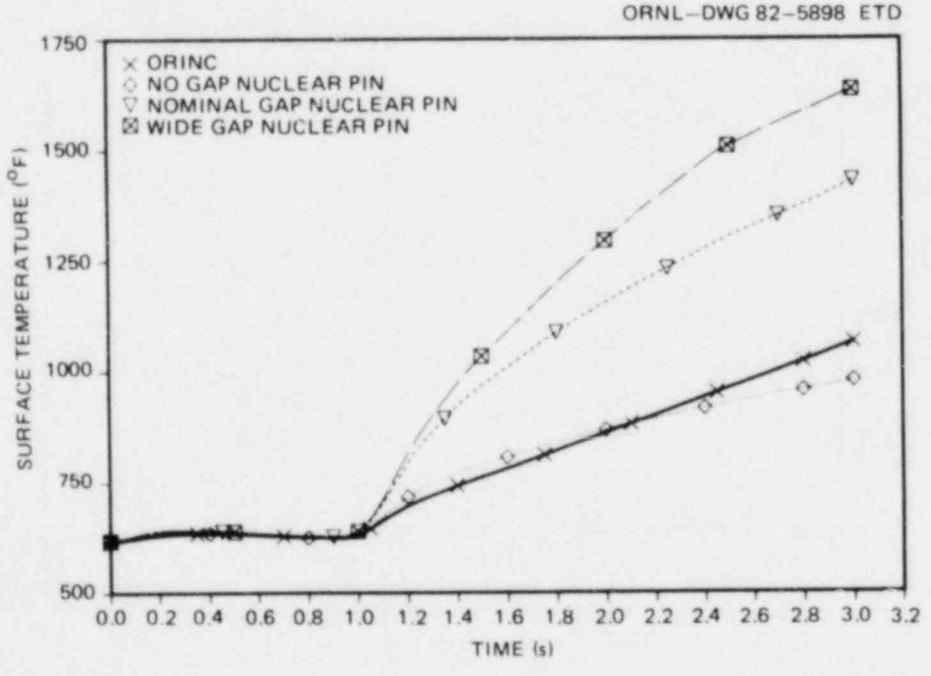

Fig. 4.7. Comparison of surface temperatures for FRS (ORINC) and nuclear fuel rod models with different gap sizes – axial level C.

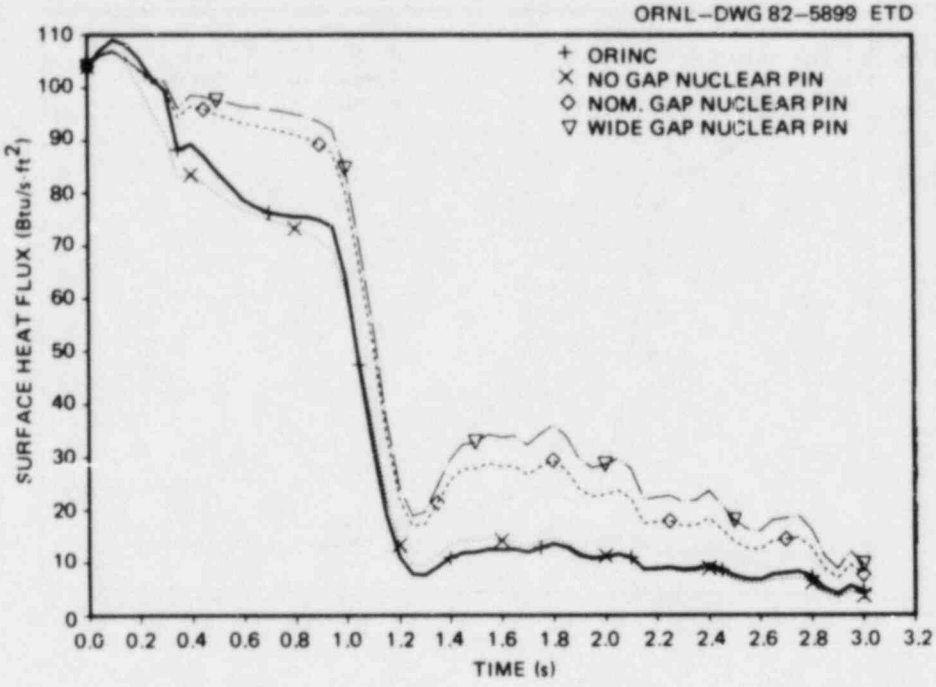

Fig. 4.8. Comparison of surface heat fluxes for FRS (ORINC) for nuclear fuel rod models with different gap sizes – axial level D.

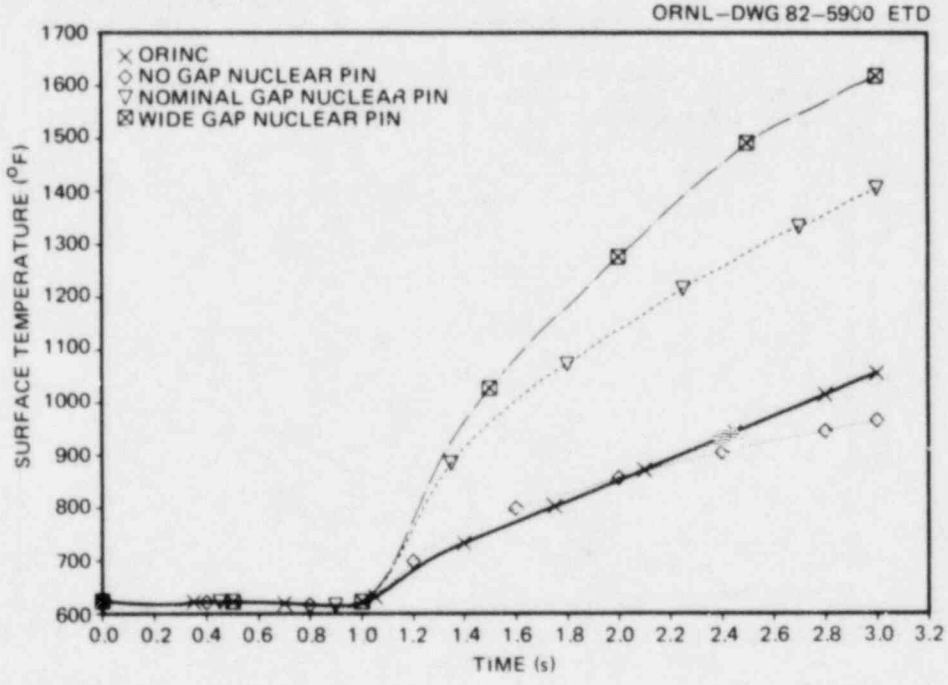

Fig. 4.9. Comparison of surface temperatures for FRS (ORINC) and nuclear fuel rod models with different gap sizes – axial level D.

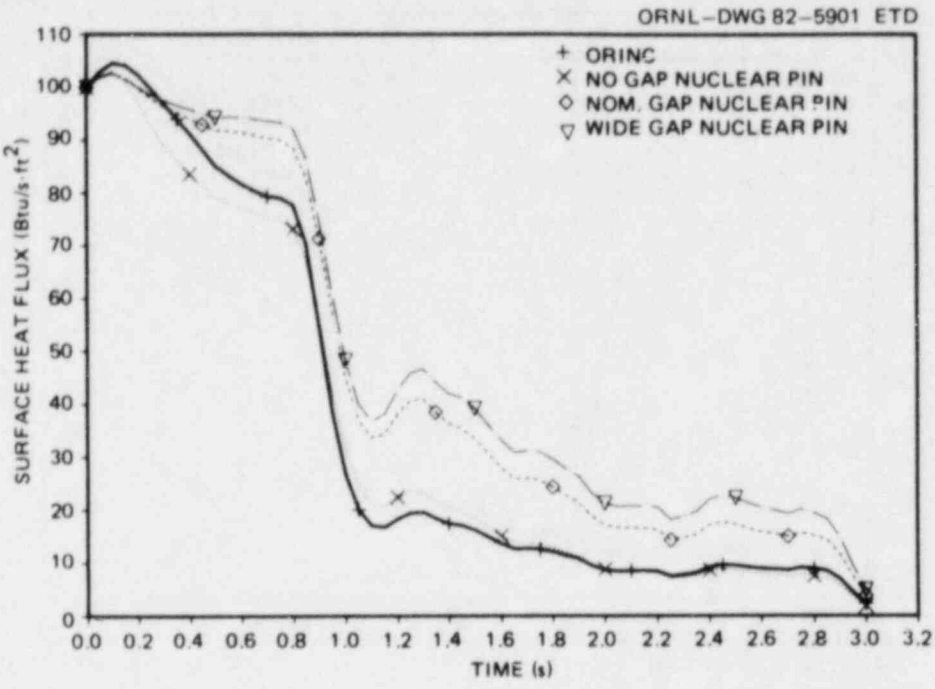

Fig. 4.10. Comparison of surface heat fluxes for FRS (ORINC) for nuclear fuel rod models with different gap sizes – axial level E.

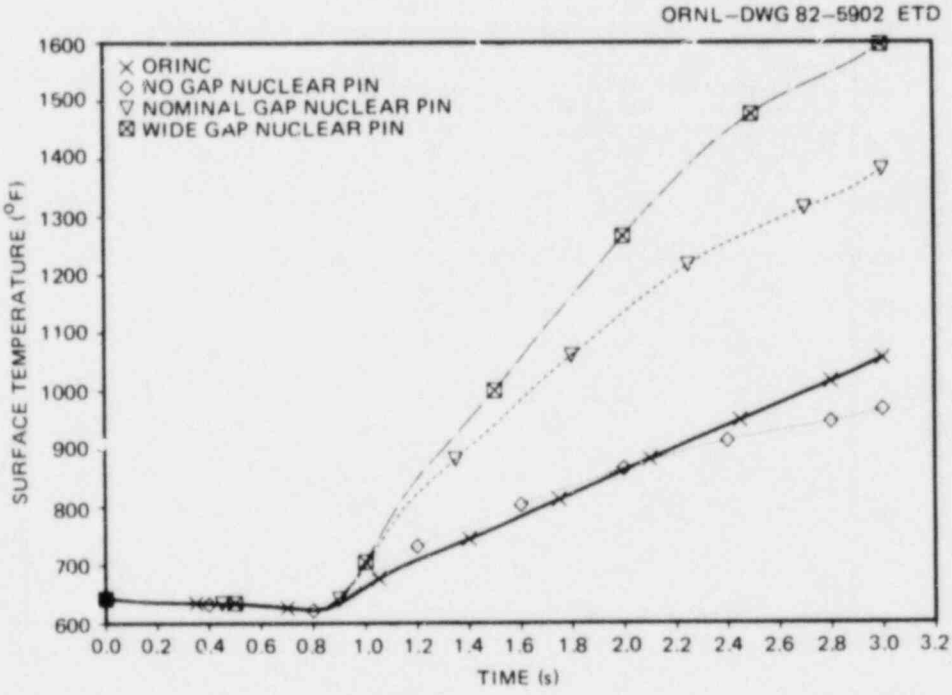

Fig. 4.11. Comparison of surface temperatures for FRS (ORINC) and nuclear fuel rod models with different gap sizes – axial level E.

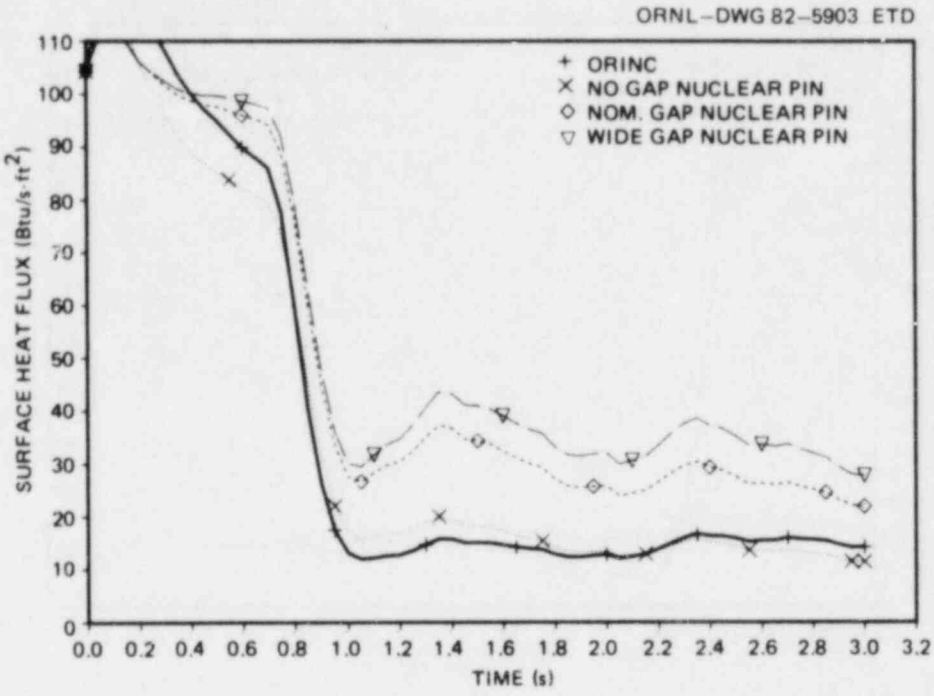

Fig. 4.12. Comparison of surface heat fluxes for FRS (ORINC) and nuclear fuel rod models with different gap sizes – axial level F.

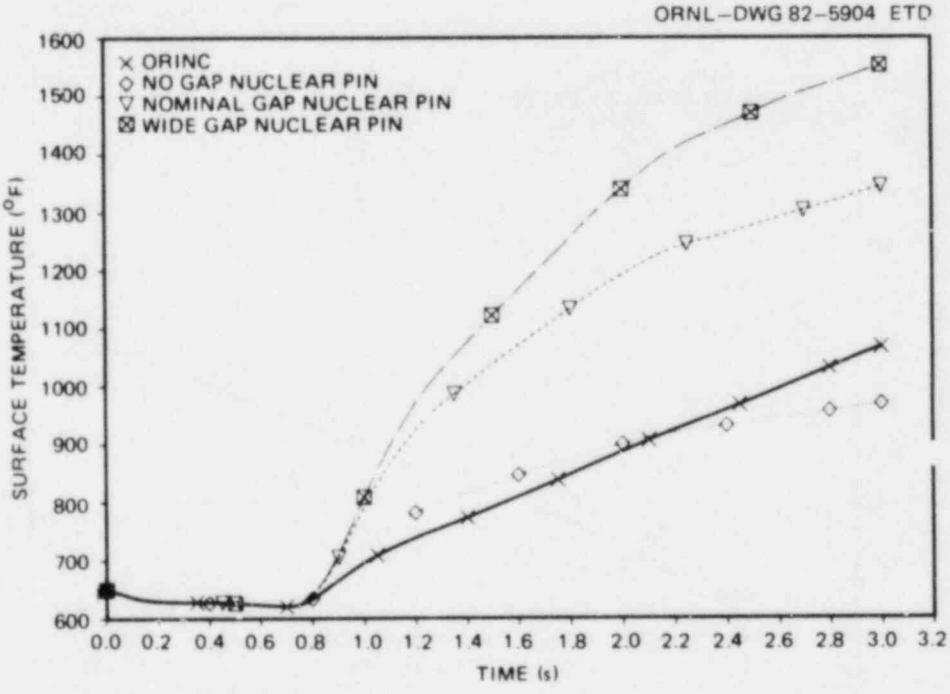

Fig. 4.13. Comparison of surface temperatures for FRS (ORINC) and nuclear fuel rod models with different gap sizes – axial level F.

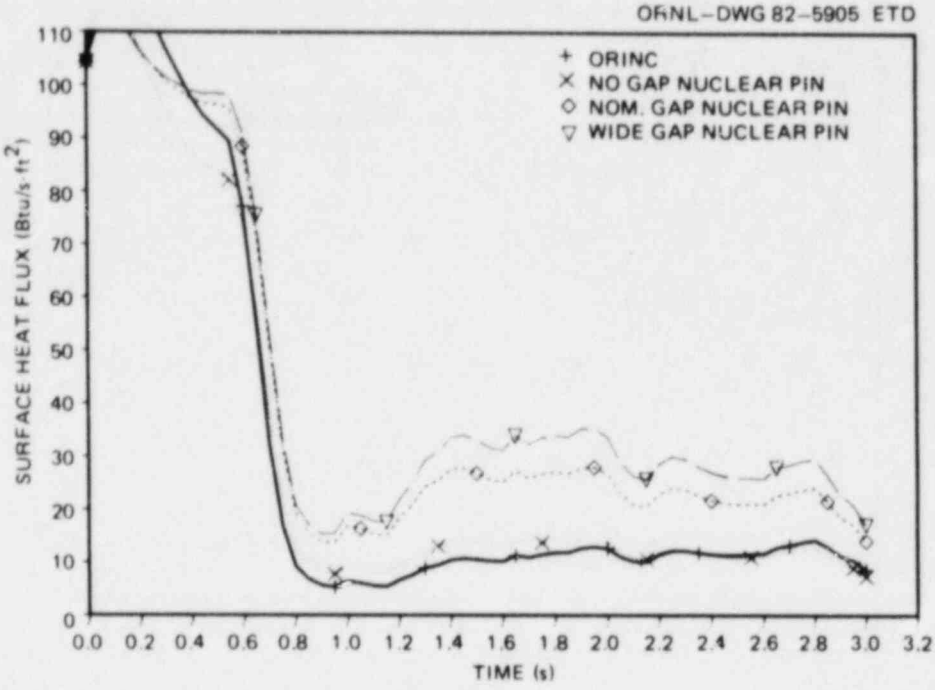

Fig. 4.14. Comparison of surface heat fluxes for FRS (ORINC) and nuclear fuel rod models with different gap sizes – axial level G.

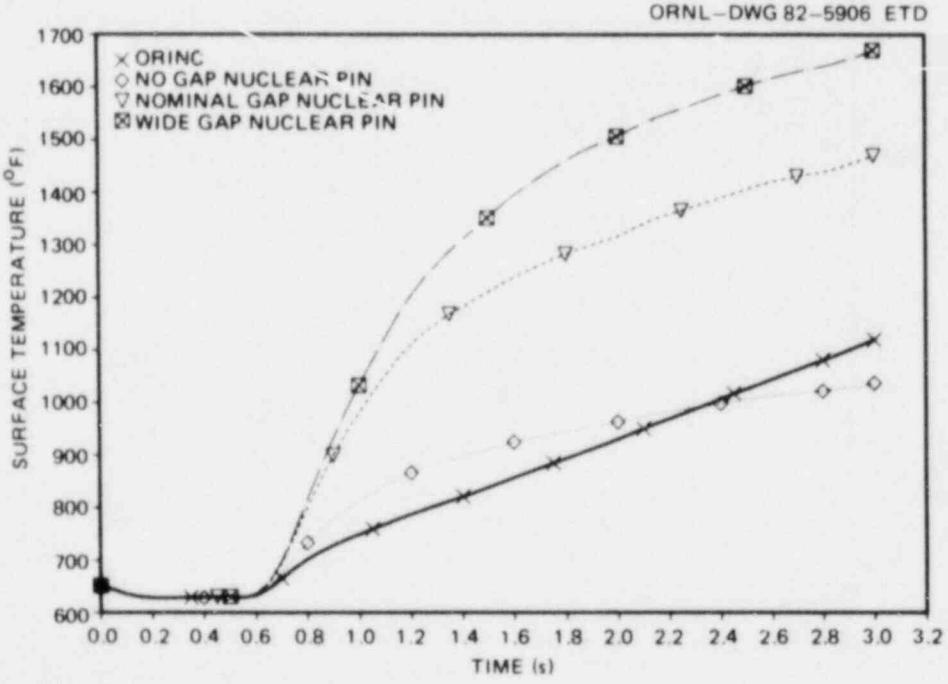

Fig. 4.15. Comparison of surface temperatures for FRS (ORINC) and nuclear fuel rod models with different gap sizes – axial level G.

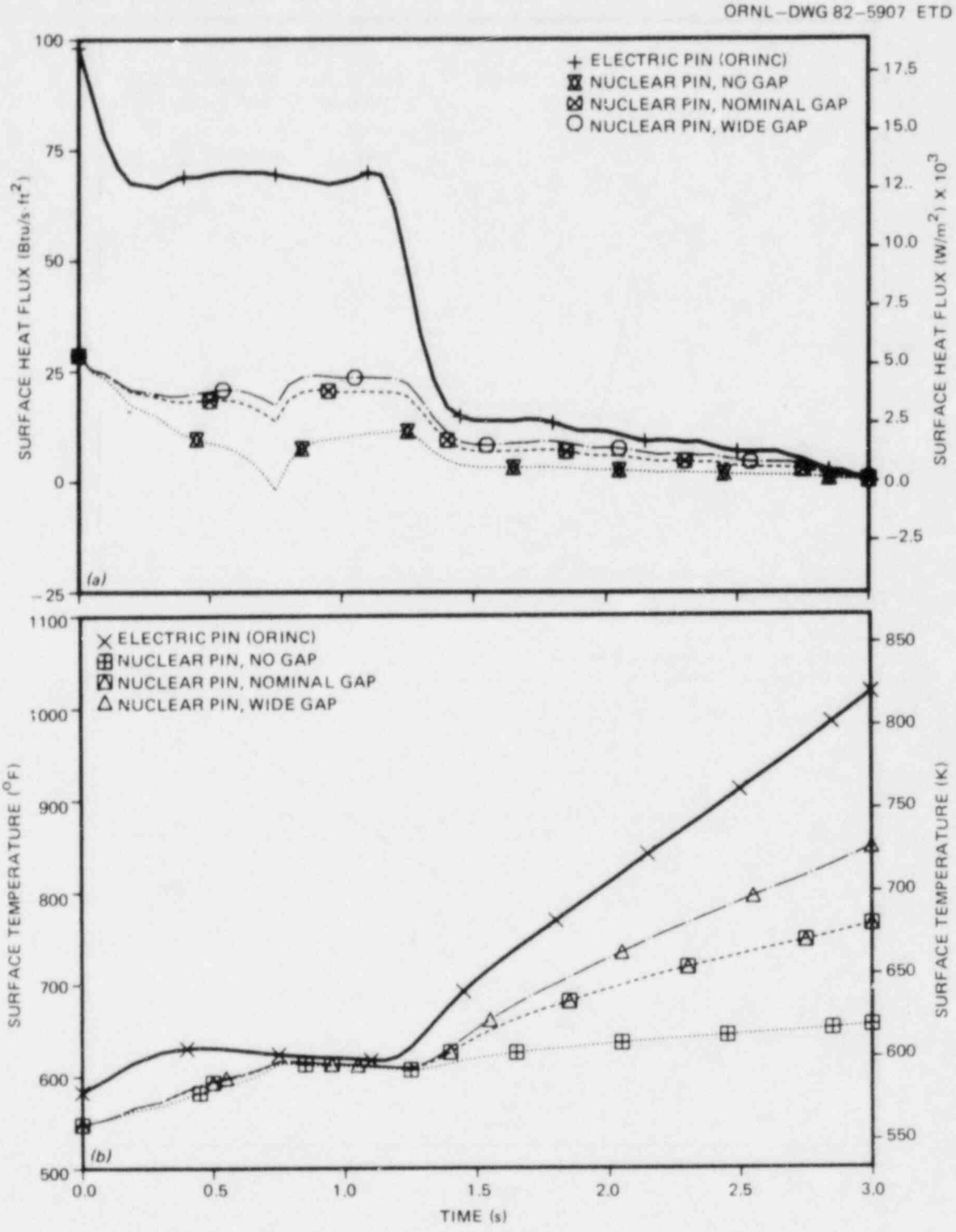

Fig. 4.16. Comparison of (a) surface heat fluxes and (b) temperatures for FRS (ORINC) and nuclear fuel rod models with different gap sizes and low initial power – axial level A.

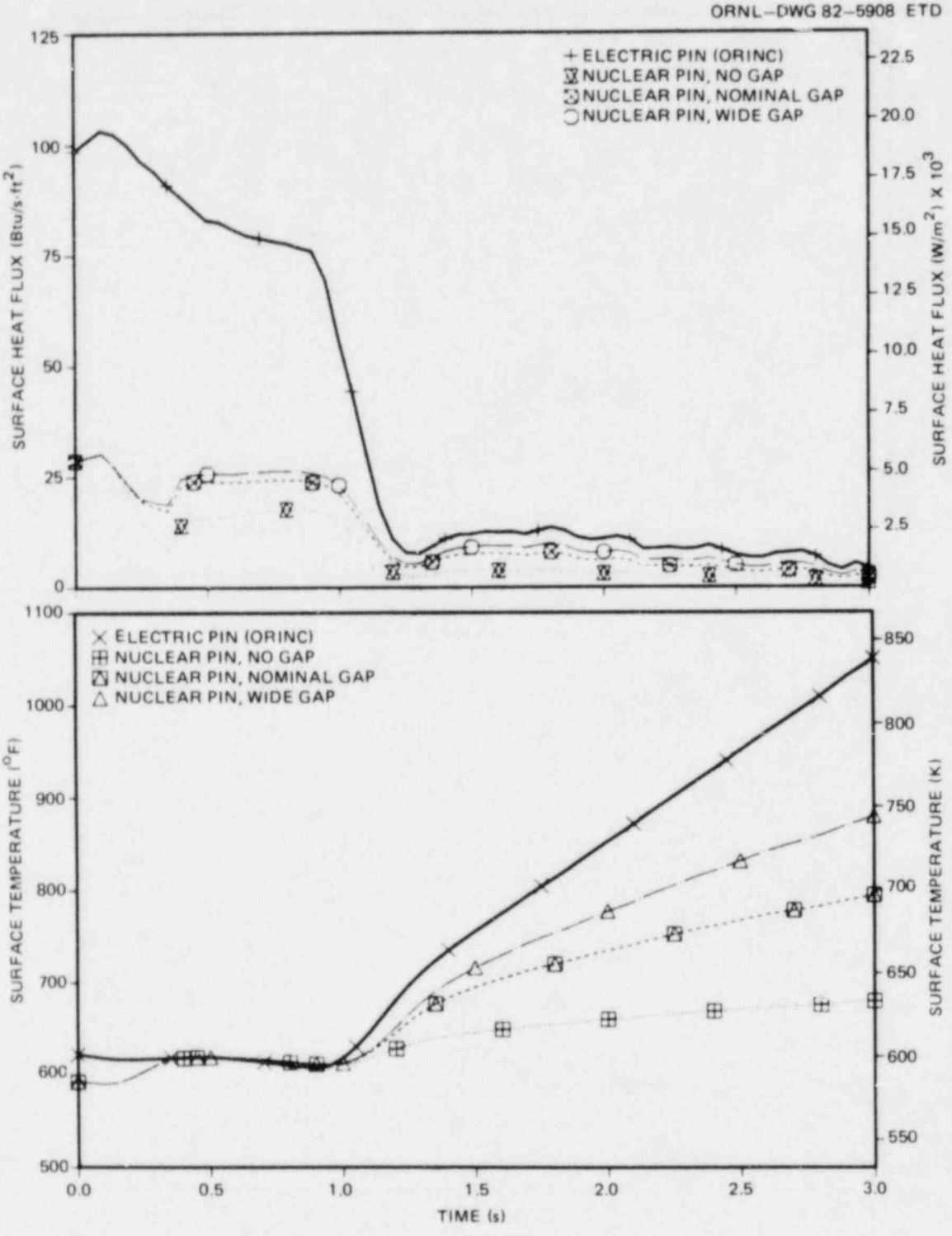

Fig. 4.17. Comparison of (a) surface heat fluxes and (b) temperatures for FRS (ORINC) and nuclear fuel rod models with different gap sizes and low initial power – axial level D.

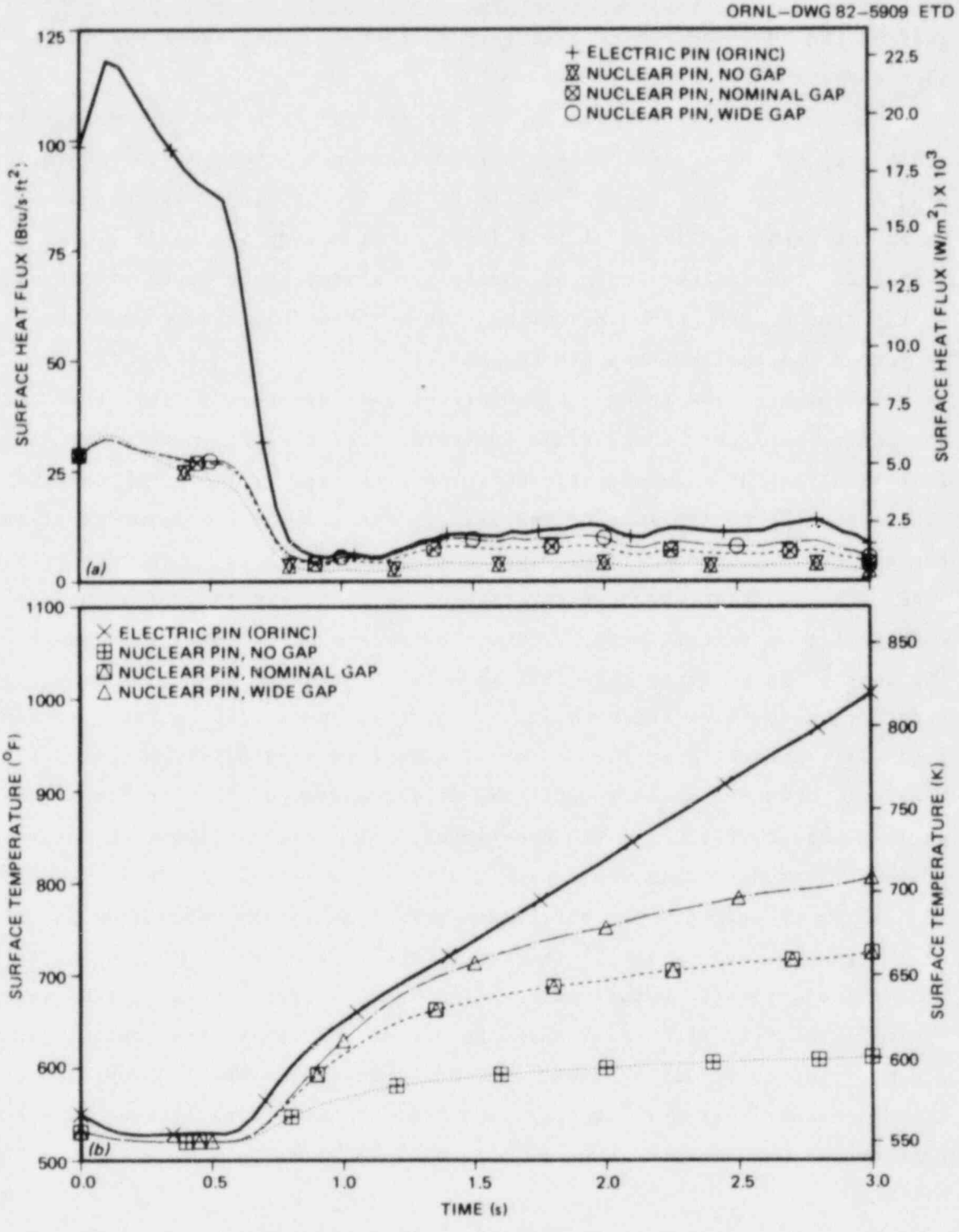

Fig. 4.18. Comparison of (a) surface heat fluxes and (b) temperatures for FRS (ORINC) and nuclear fuel rod models with different gap sizes and low initial power – axial level G.

surface heat flux for the nuclear fuel rod models is always much less than that of the FRS, indicating that they would have experienced DNB later than did the FRS.

Finally, we compare the response of the FRS with that of nuclear fuel rod models having initial powers characteristic of those at the center of a nuclear core. Once again, results at all levels are similar, and only three are presented (Figs. 4.19–4.21). As expected, the surface heat fluxes for the nuclear fuel rod models are always above those of the FRSs at the time of DNB, thus indicating that nuclear fuel rods would have experienced DNB earlier than did the FRS.

In summary, the forward calculations indicate that nuclear fuel rods exposed to the same hydrodynamic environment as that which occurred in Test 3.05.5B could have experienced either earlier or later DNB than the FRS, depending on the size of the gas gap and the initial power level in the nuclear fuel rod. If the fluid conditions anywhere in the electric bundle can be taken as representative of those at the ends of a nuclear core during an actual accident, then the nuclear rods' DNB at the ends of the core would be later than that seen in the experiment. Similarly, if the fluid conditions anywhere in the electric bundle can be taken as representative of those at the center of a nuclear core during an actual accident, then the nuclear rods' DNB at the center of the core would be earlier than that seen in the experiment. At those positions in the core where nuclear fuel rods would have had the same initial power as did the FRS in the experiment, the relationship of time to DNB depends on the size of the gas gap. Because (1) the no-gap model is probably not characteristic of the majority of nuclear fuel rods and (2) even in that case, the nuclear heat flux is only slightly below the CHF, where the nominal-gap and wide-gap model calculations were well above the CHF, it is probably fair to assume that most nuclear fuel rods at these locations would have experienced DNB earlier than did the FRS in Test 3.05.5B.

4.3 Comparison of Reactor and THTF Bundle Fluid Conditions

The question of how the behavior of FRSs in an experimental facility such as the THTF relates to the behavior of nuclear fuel rods during an actual reactor accident can be broken into two parts. First, what is the

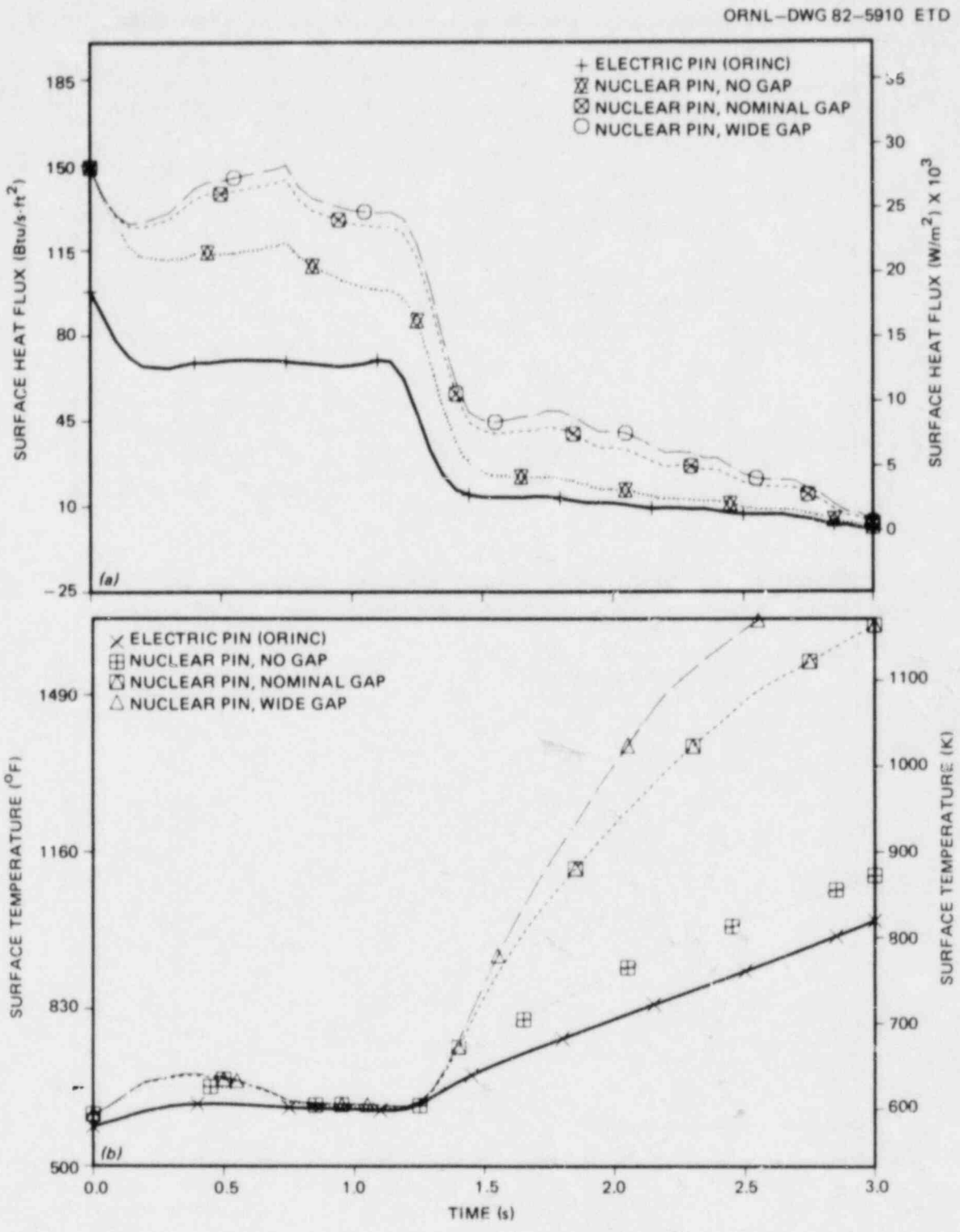

Fig. 4.19. Comparison of (a) surface heat fluxes and (b) temperatures for FRS (ORINC) and nuclear fuel rod models with different gap sizes and high initial power – axial level A.

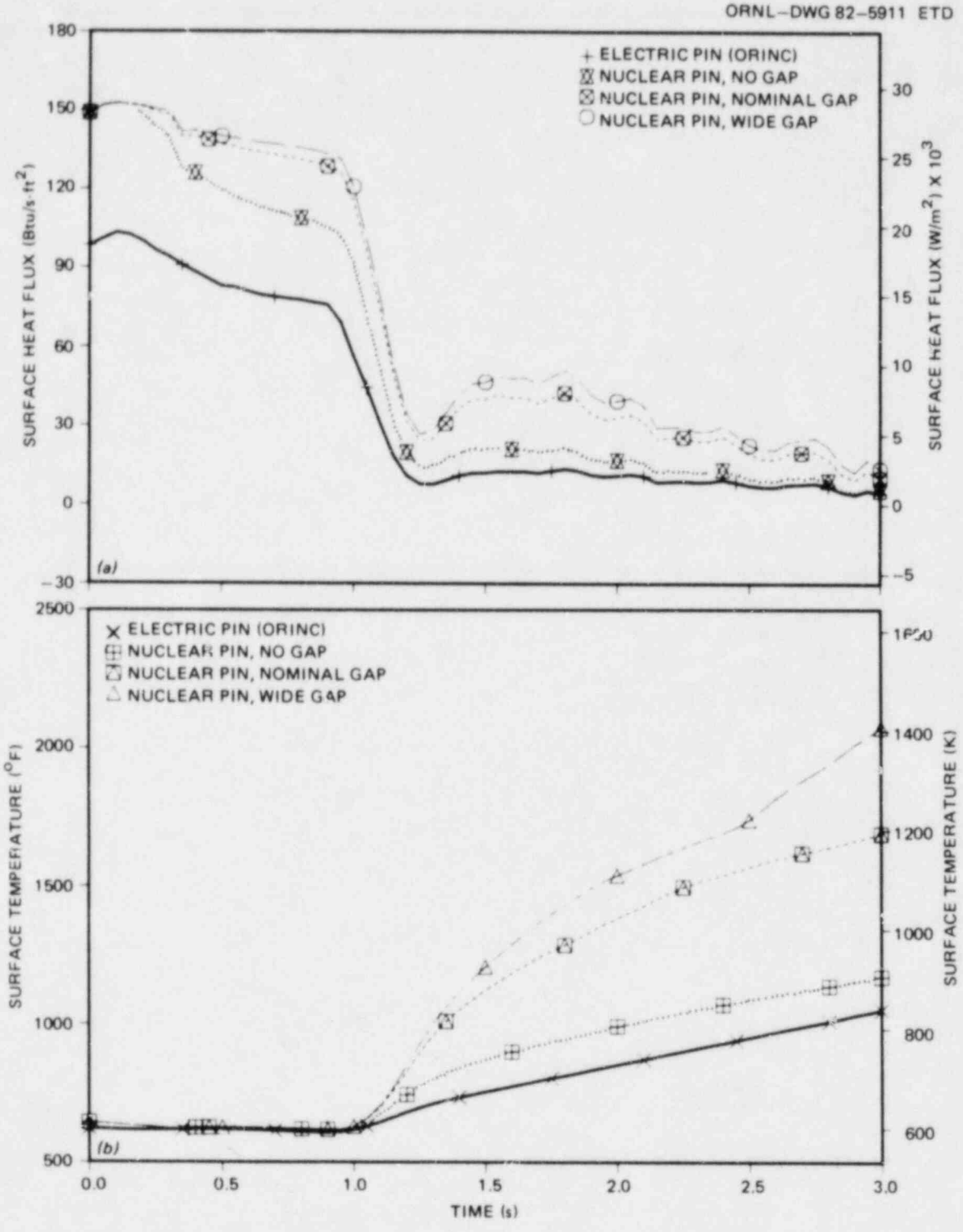

Fig. 4.20. Comparison of (a) surface heat fluxes and (b) temperatures for FRS (ORINC) and nuclear fuel rod models with different gap sizes and high initial power – axial level D.

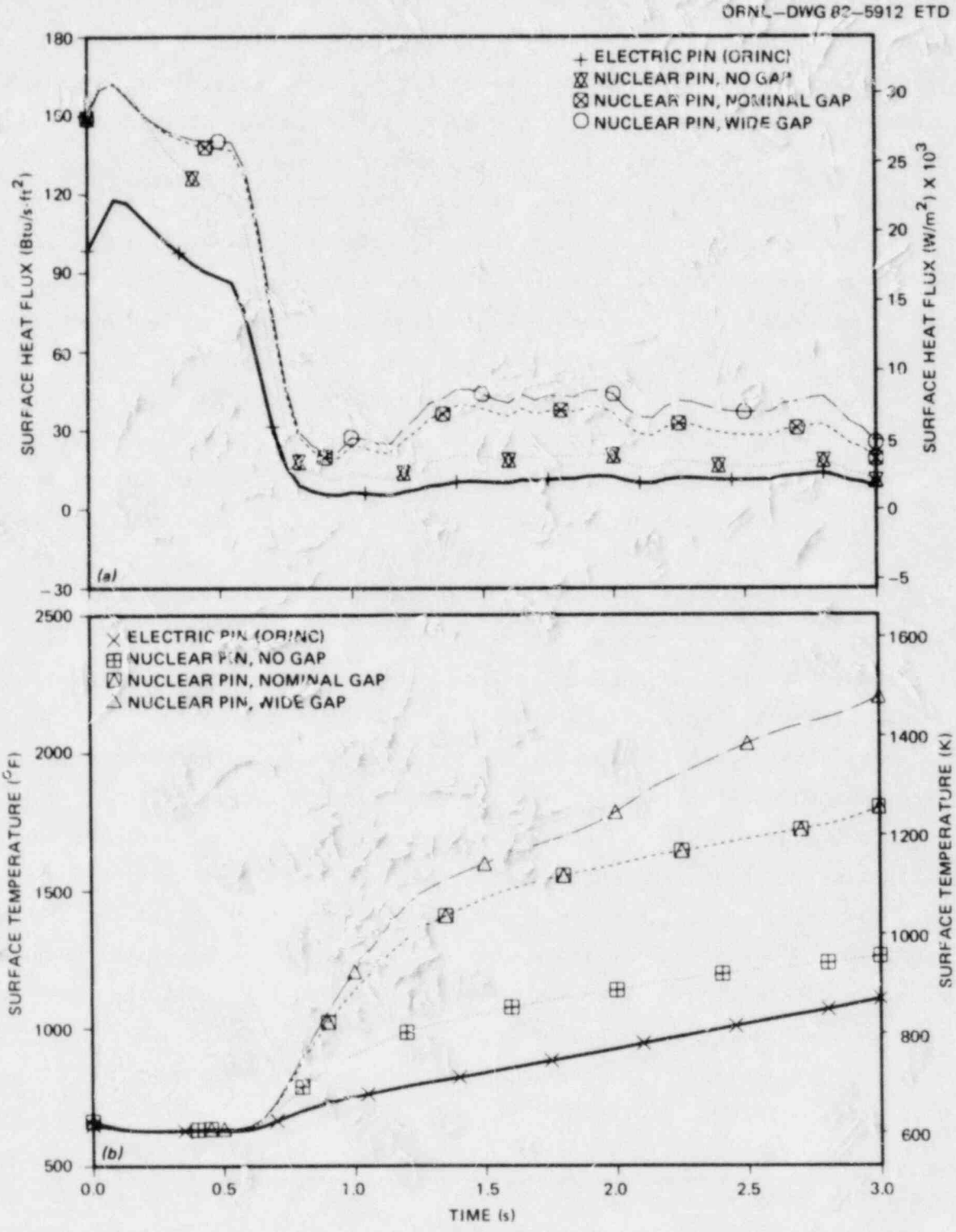

Fig. 4.21. Comparison of (a) surface heat fluxes and (b) temperatures for FRS (ORINC) and nuclear fuel rod models with different gap sizes and high initial power – axial level G.

relationship of the behavior of an electric FRS to the behavior of a nuclear fuel rod exposed to identical hydrodynamic environments? Second, to what extent did the hydrodynamic environment in the experiment match the hydrodynamic environment that would occur during an actual reactor accident? The analytical effort described thus far in this report has addressed the first of these two questions. As mentioned previously, the second question is much more difficult to address. This difficulty stems both from the difficulty in determining accurate bundle fluid conditions for an experiment such as this one and from the difficulty in determining what conditions would have existed during an actual accident.

A calculation of reactor conditions during a 200% cold-leg break has been made using RELAP4 MOD5 Update 2 as described in Sect. 2.2 (Fig. 2.11). In addition, calculations have been made of the conditions that existed in the bundle in the THTF during Test 3.05.5B. These calculations were made with a locally modified version of RELAP4 MOD5 Update 2 (Ref. 14). The modification consisted of removing the code's own heat transfer package and replacing it with the experimentally determined surface heat fluxes for the FRSs. Thus, the heat transfer correlations and switching logic normally used by the code are superseded. A model of the THTF test section was constructed (Fig. 4.22) and used in a calculation bounded by the experimentally determined rod surface heat fluxes, the mass flux, and fluid enthalpy calculated from instrument responses at the test section outlet and the pressure, temperature, and quality calculated from instrument responses at the test section inlet. Because the calculation of THTF bundle fluid conditions relies on the determination of transient two-phase mass flows (a task made even more difficult by the fact that the flow reverses and therefore periodically becomes too small to measure accurately), the accuracy of the results of such calculations must be viewed with considerable suspicion.

This section presents comparisons of the calculated reactor core hydrodynamic conditions with the calculated THTF bundle hydrodynamic conditions. Because large and unquantified uncertainties must be associated with both sets of conditions, no attempt is made to draw conclusions from these comparisons. These comparisons are presented because the relationship of hydrodynamic environments between the experiment and a reactor

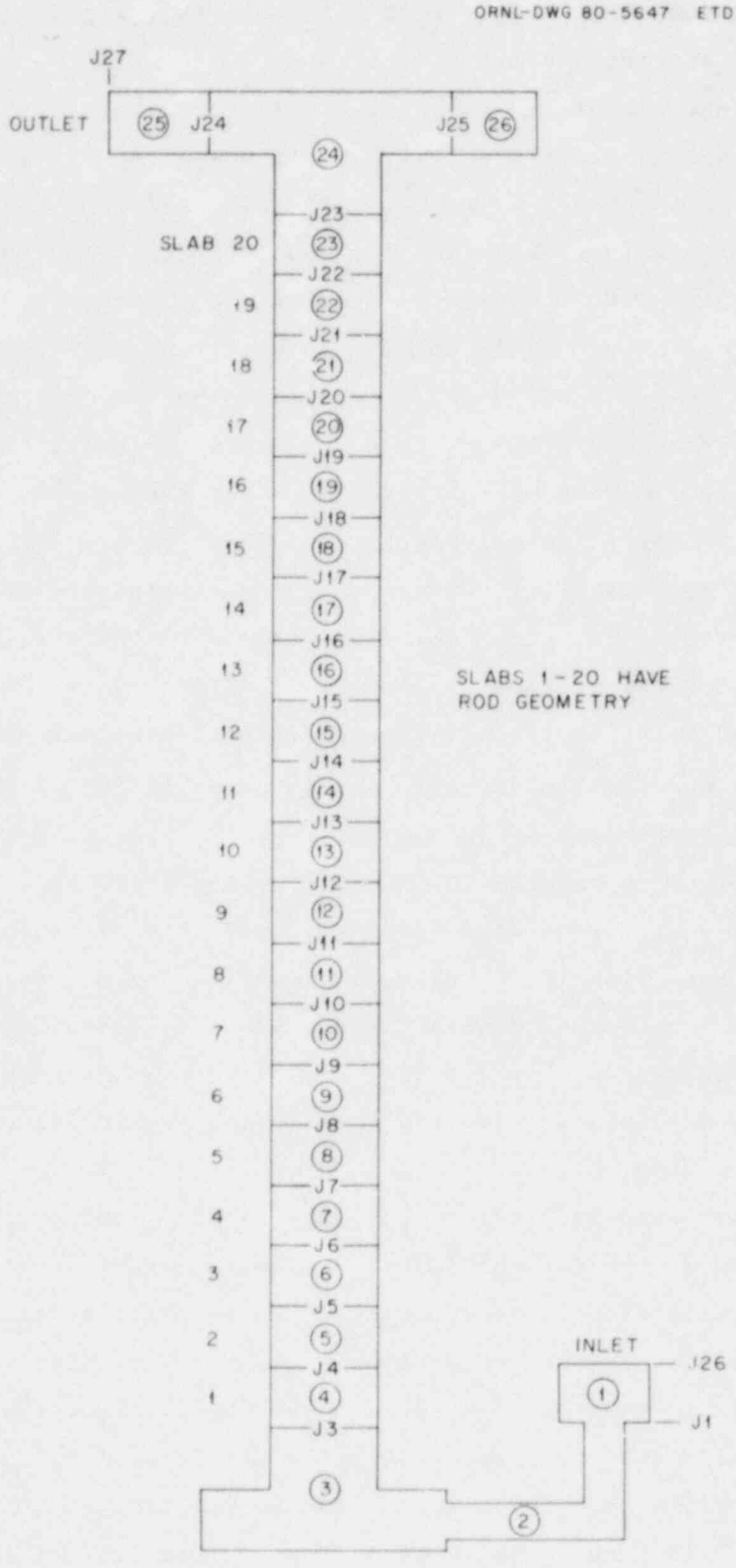

Fig. 4.22. RELAP4 MOD5 Update 2 nodalization of THTF test section.

accident is important, and the calculational results presented here are the best ones currently available.

Because the variations in absolute pressure along either bundle were not calculated to be large, a single graph comparing variations of pressure with time is presented in Fig. 4.23. The model of the reactor (Fig. 2.11) used three volumes to model the reactor core: one for the lower core, one for the middle core, and one for the upper core. The model of the THTF test section used 20 volumes to model the THTF bundle. Thus, for most of these comparisons, results from more than one volume in the THTF model will be compared with a single volume of the reactor model. The volumes from the THTF model selected for these comparisons contained primary FRS thermocouple levels (Fig. 2.7). Thus, in Fig. 4.24, which compares fluid temperatures, the temperature calculated for the lower core in the reactor (volume 34, Fig. 2.11) is compared to the fluid temperatures calculated for three volumes in the lower portion of the THTF bundle (volumes 4, 6, and 8 in Fig. 4.22). The relationship between THTF RELAP4 model volumes and the thermocouple levels shown in Fig. 2.7 is as follows: volume 4-TC level A, volume 6-TC level B, volume 8-TC level C, volume 11-TC level D, volume 14-TC level E, volume 18-TC level F, and volume 23-TC level G. Figures 4.23-4.41 show comparisons of fluid temperature, quality, and mass flux for the lower, middle, and upper cores for both the average and hot reactor channels. Each figure contains two graphs; one presents the comparisons over a time period from 0-15 s, and one shows the comparison on an expanded time scale extending from 0-3 s, during which the majority of DNBs occur.

To provide some qualitative feeling for the accuracy of the fluid conditions calculated for the THTF rod bundle, graphical comparisons are presented between calculated conditions and selected instrument responses that were not used in the computation of boundary conditions for the calculation. The parameters compared are the inlet volumetric flow (Fig. 4.42), the inlet density (Fig. 4.43), the bundle outlet fluid temperature (Fig. 4.44) [note that these are thermocouples located in the bundle ~2.54 cm (~1.0 in.) above the heated length; they are not thermocouples at the test section outlet spool piece], and test section outlet pressure (Fig. 4.45).

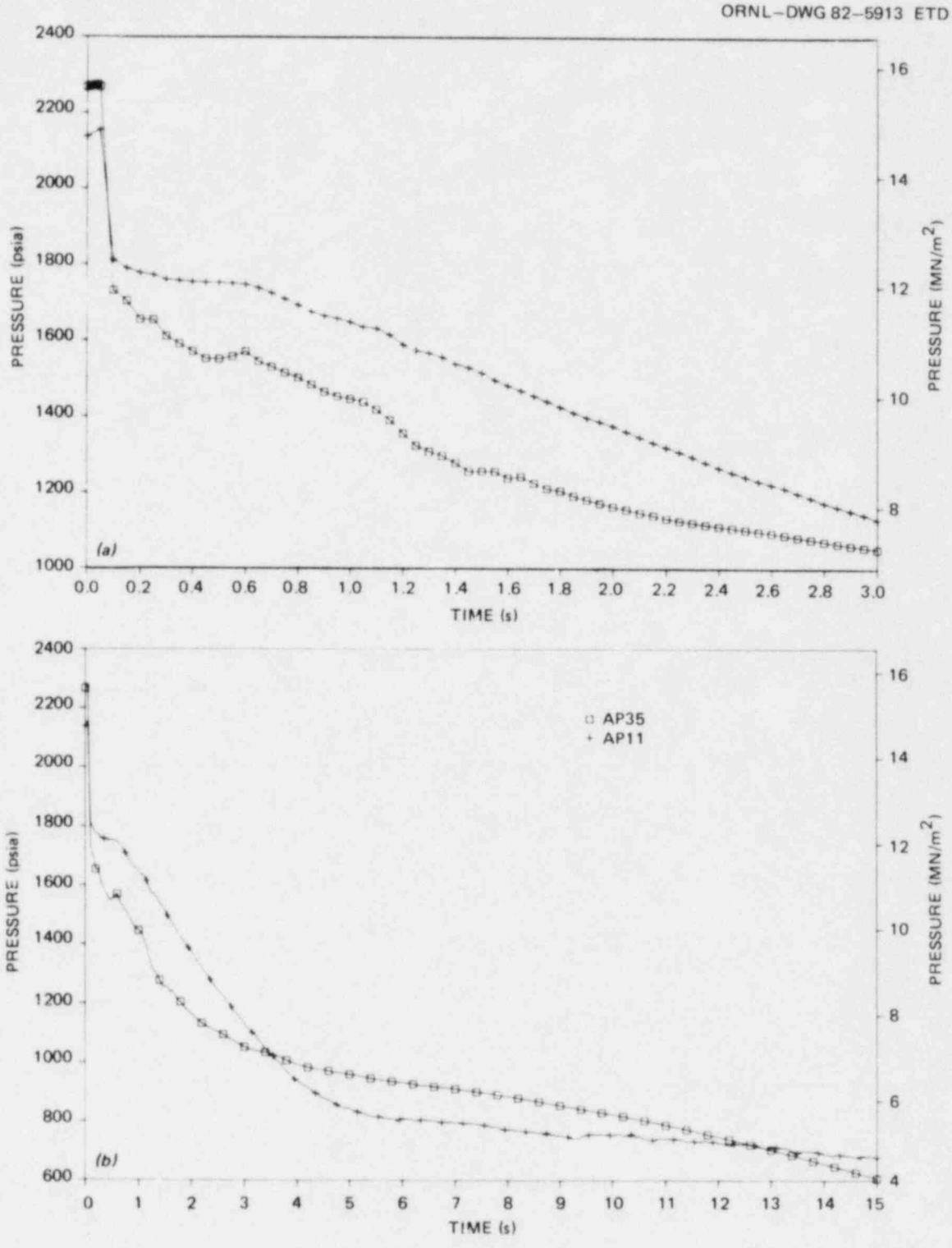

Fig. 4.23. Comparison of calculated THTF conditions and RELAP4 reactor DECLB prediction (square symbols) – pressure: (a) 0–3 s and (b) 0–15 s.

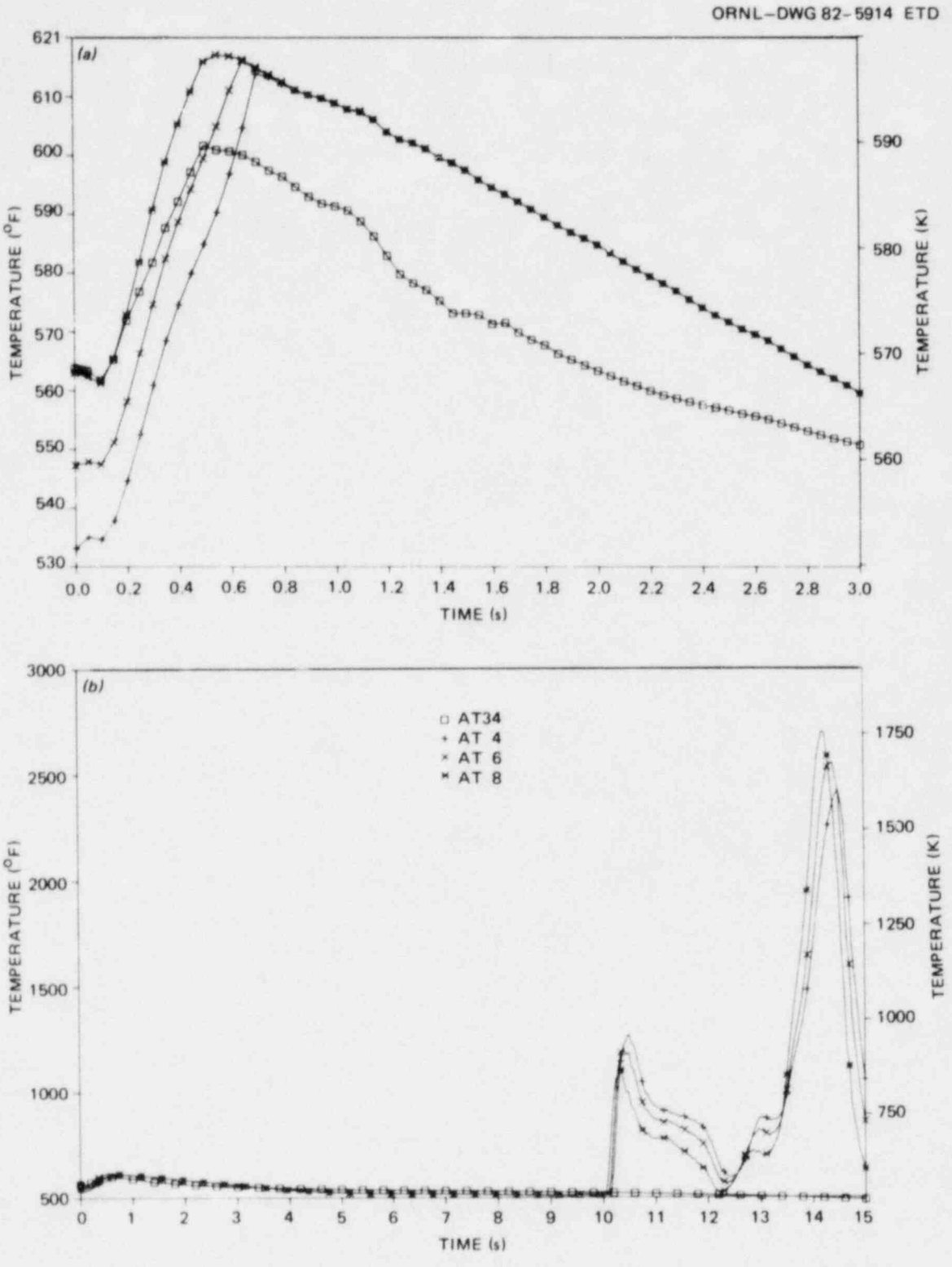

Fig. 4.24. Comparison of calculated THTF conditions and RELAP4 reactor average-power channel DECLB prediction (square symbols) - lower core fluid temperature: (a) 0-3 s and (b) 0-15 s.

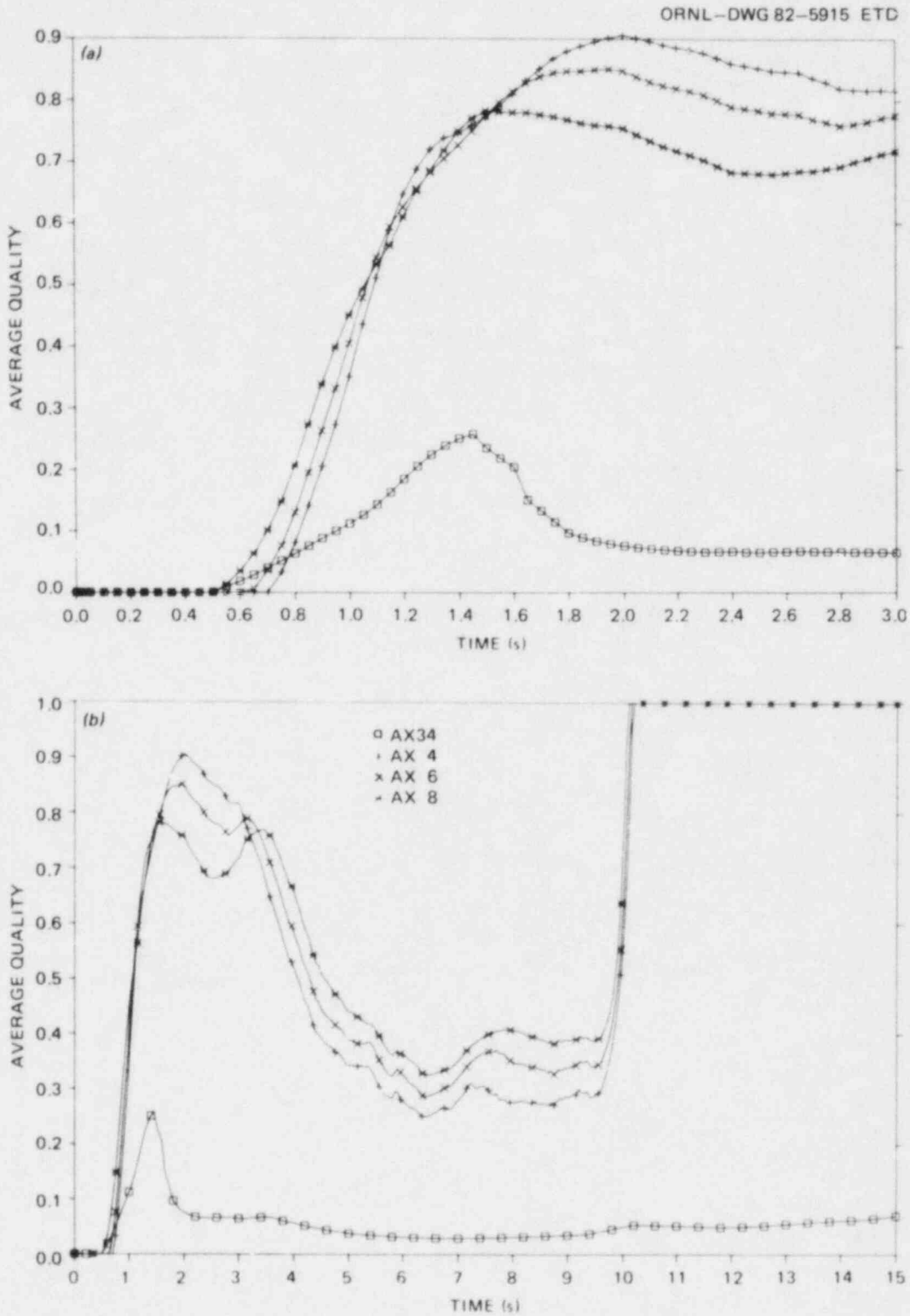

Fig. 4.25. Comparison of calculated THTF conditions and RELAP4 reactor average-power channel DECLB prediction (square symbols) - lower core fluid quality: (a) 0-3 s and (b) 0-15 s.

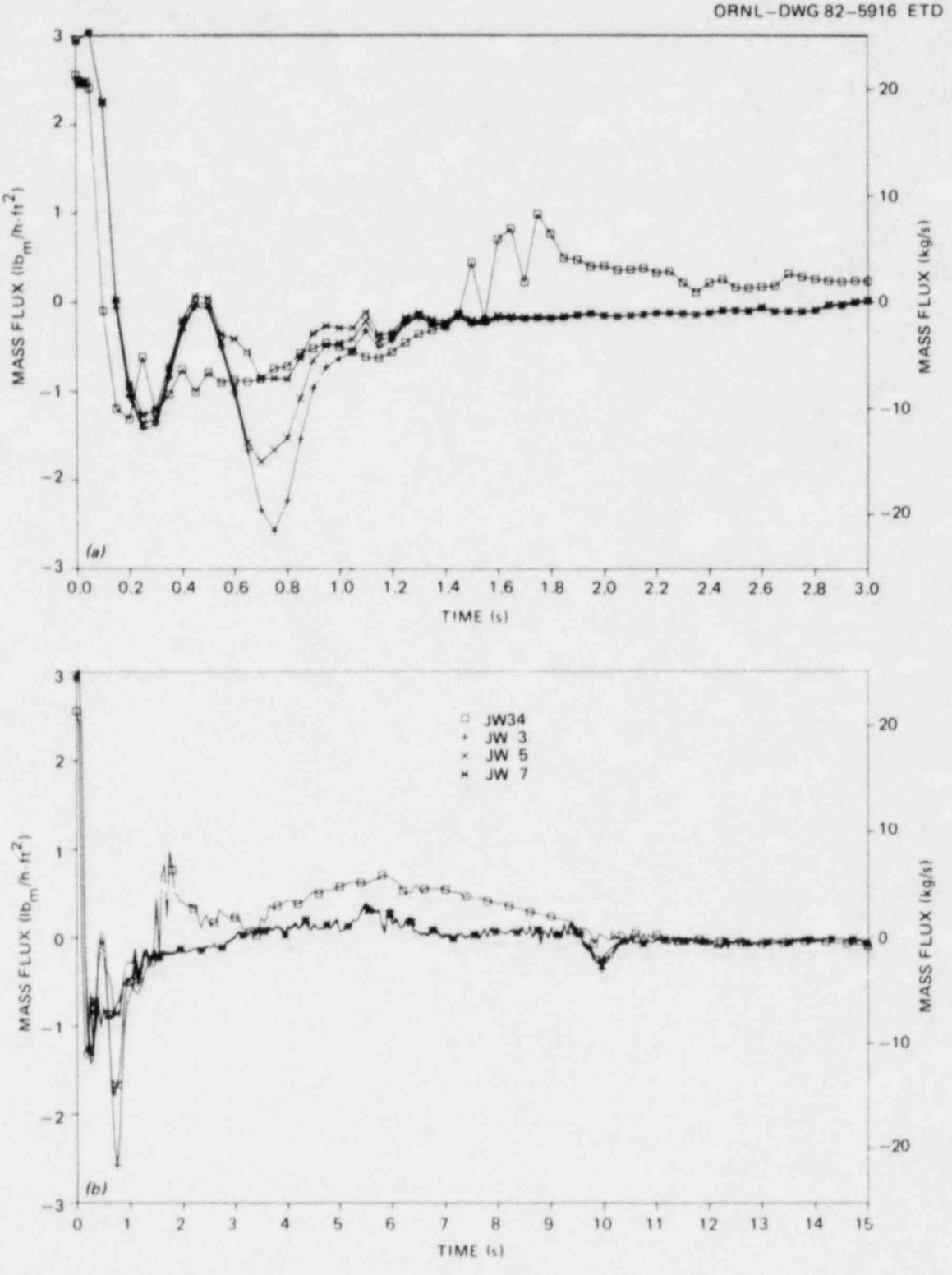

Fig. 4.26. Comparison of calculated TUTF conditions and RELAP4 reactor average-power channel DECLB prediction (square symbols) – lower core mass flux: (a) 0–3 s and (b) 0–15 s.

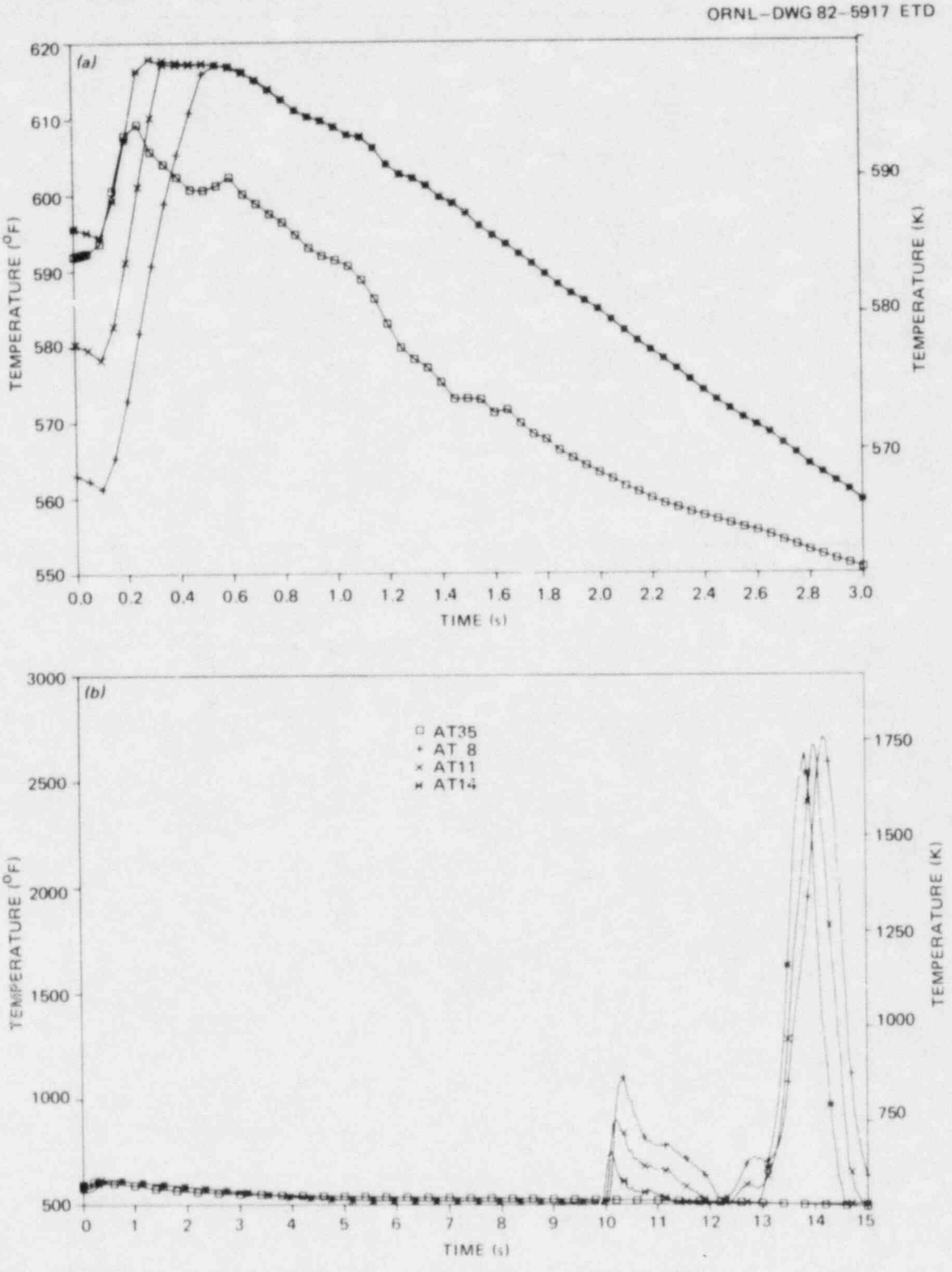

Fig. 4.27. Comparison of calculated THTF conditions and RELAP4 reactor average-power channel DECLB prediction (square symbols) – middle core fluid temperature: (a) 0–3 s and (b) 0–15 s.

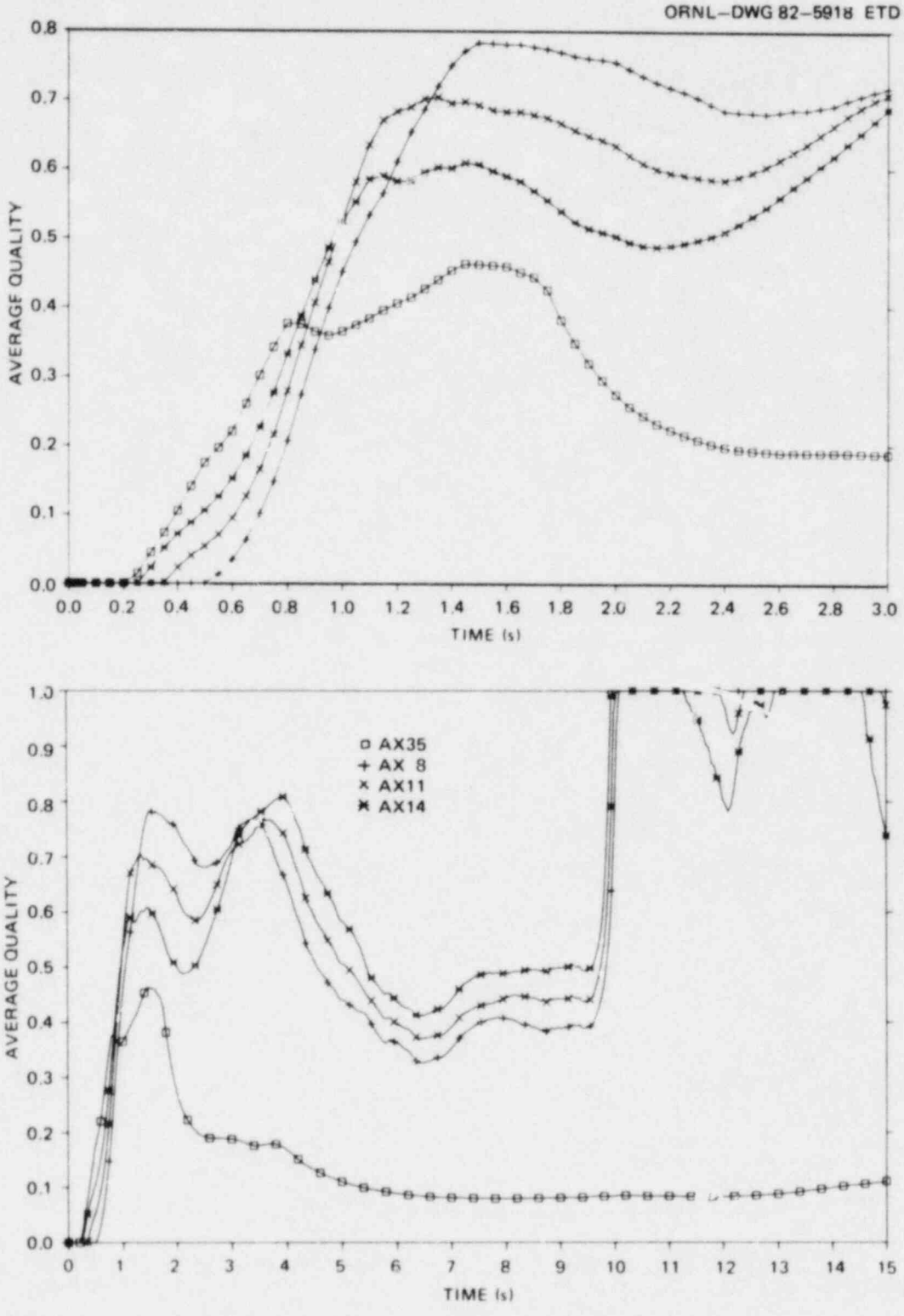

Fig. 4.28. Comparison of calculated THTF conditions and RELAP4 reactor average-power channel DECLB prediction (square symbols) - middle core fluid quality: (a) 0-3 s and (b) 0-15 s.

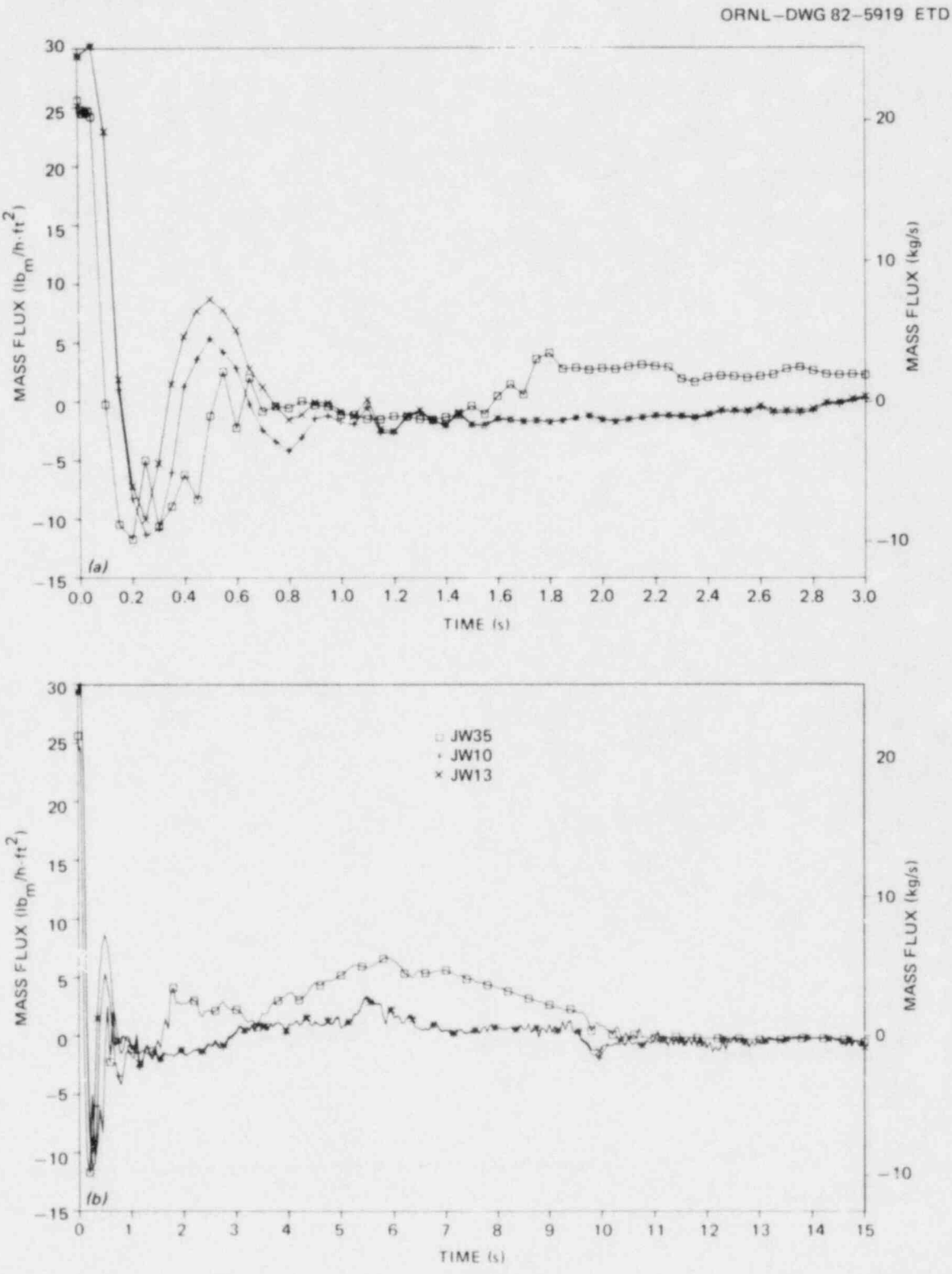

Fig. 4.29. Comparison of calculated THTF conditions and RELAP4 reactor average-power channel DECLB prediction (square symbols) - middle core mass: (a) 0-3 s and (b) 0-15 s.

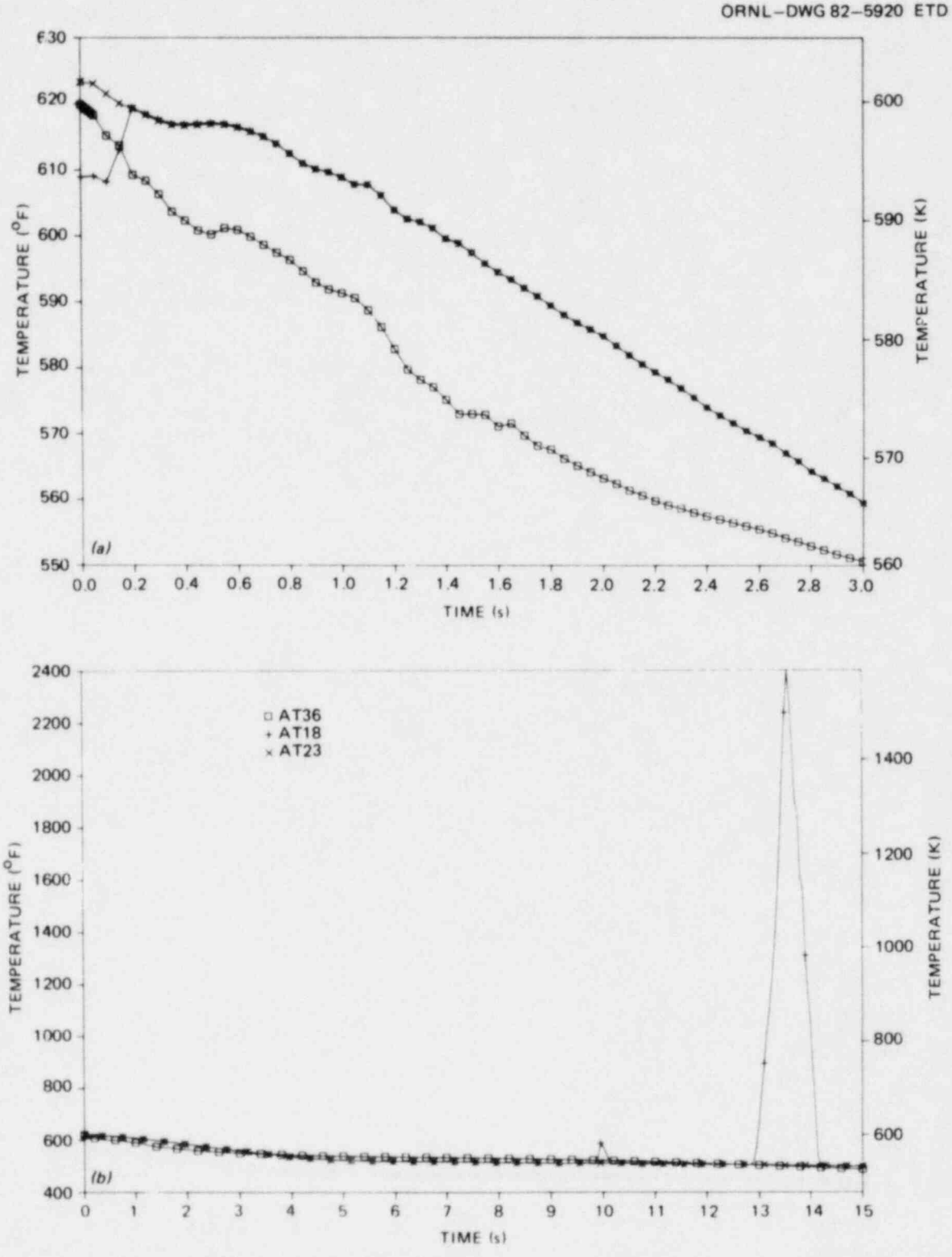

Fig. 4.30. Comparison of calculated THTF conditions and RELAP4 reactor average-power channel DECLB prediction (square symbols) – upper core fluid temperature: (a) 0–3 s and (b) 0–15 s.

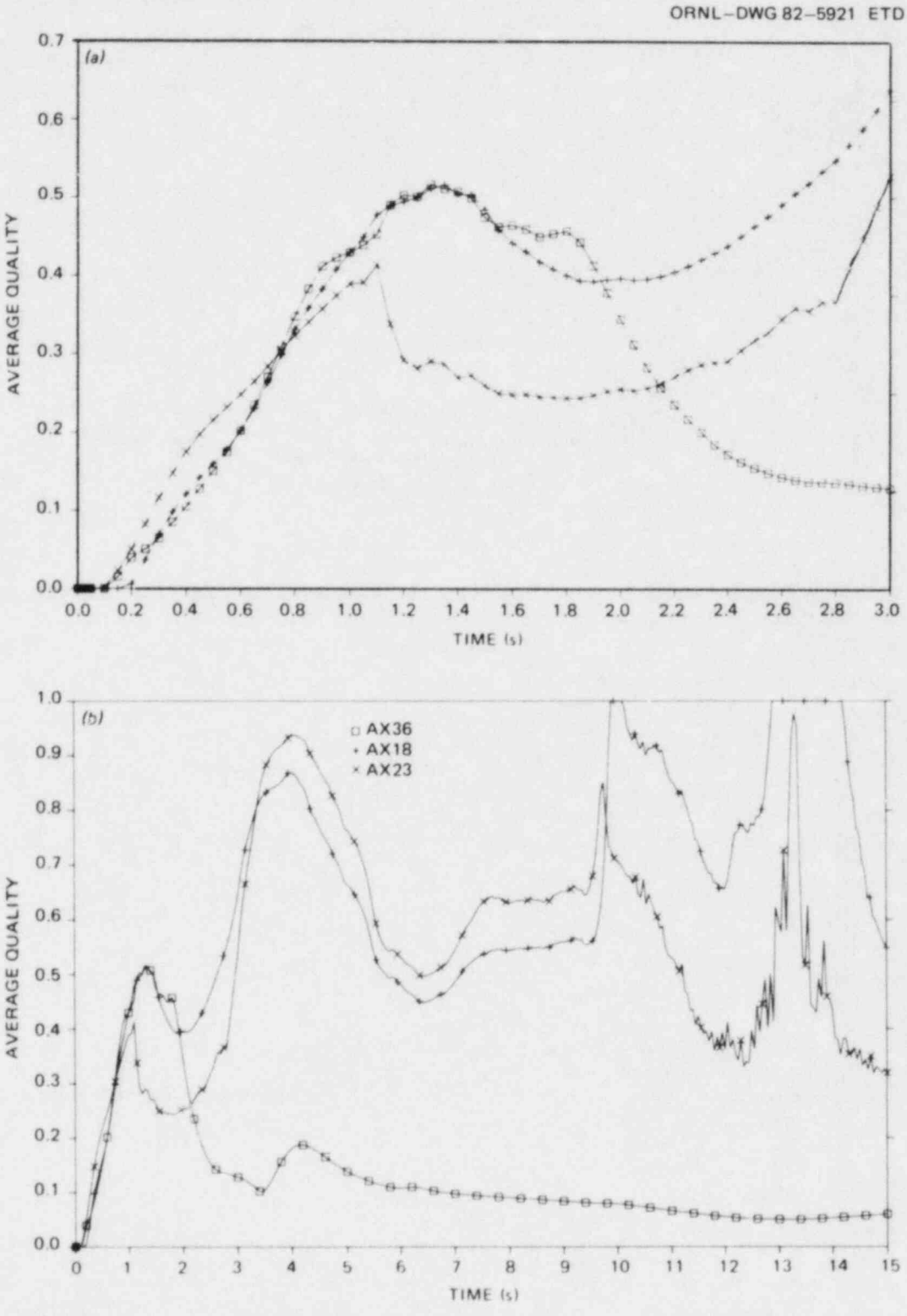

Fig. 4.31. Comparison of calculated THTF conditions and RELAP4 reactor average-power channel DECLB prediction (square symbols) – upper core fluid quality: (a) 0–3 s and (b) 0–15 s.

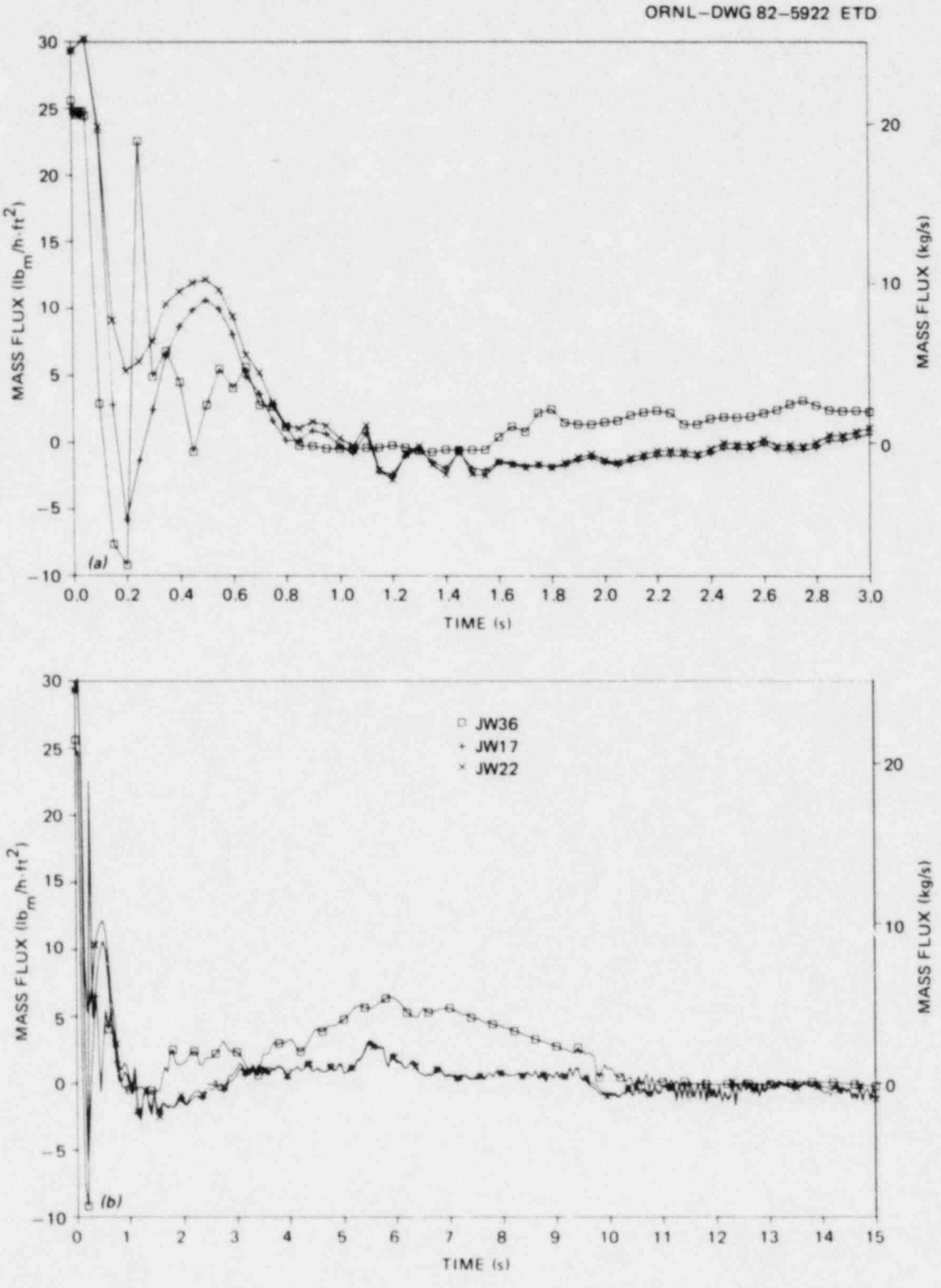

Fig. 4.32. Comparison of calculated THTF conditions and RELAP4 reactor average-power channel DECLB prediction (square symbols) – upper core mass flux: (a) 0–3 s and (b) 0–15 s.

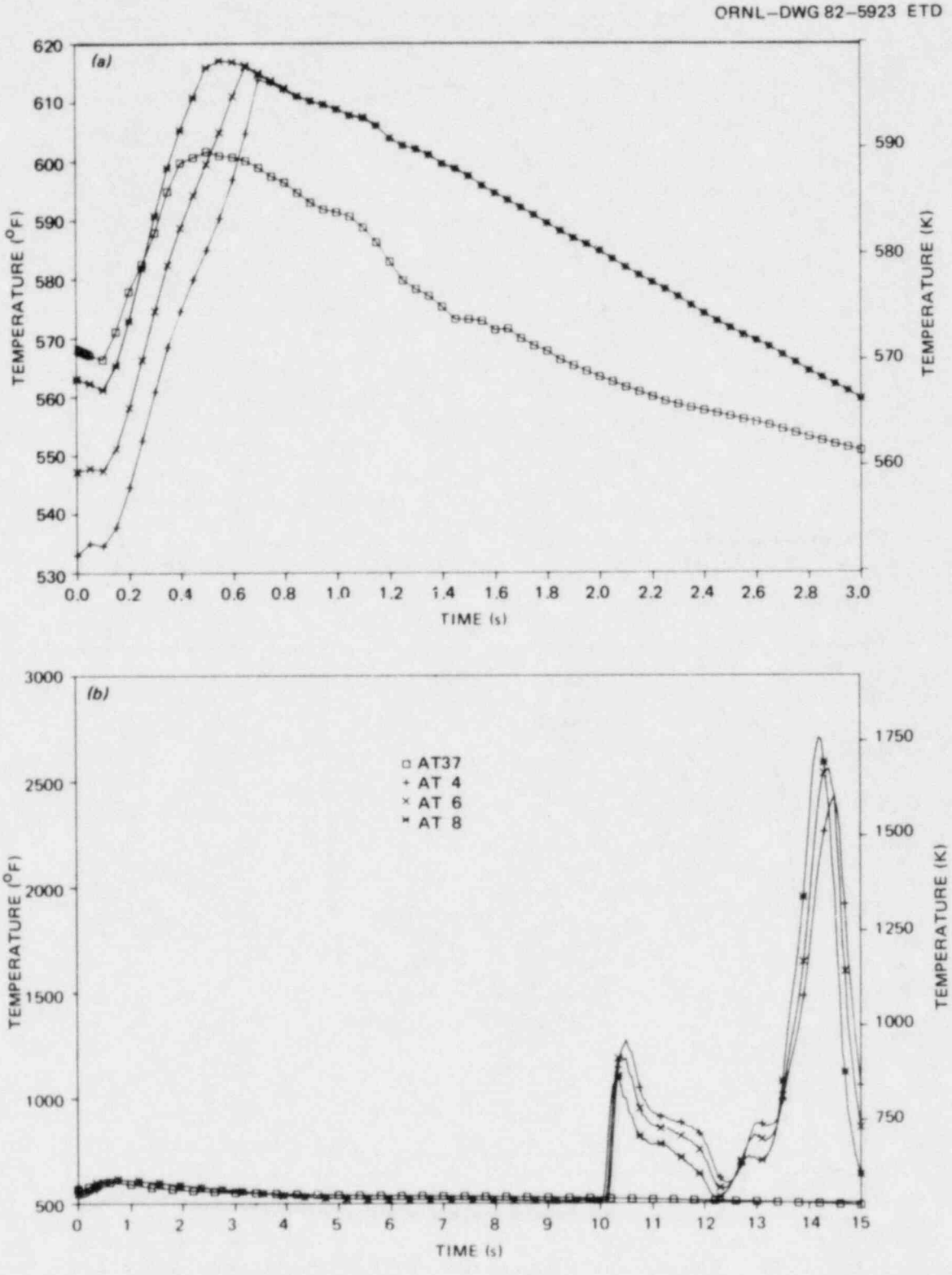

Fig. 4.33. Comparison of calculated THTF conditions and RELAP4 reactor hot channel DECLB prediction (square symbols) - lower core fluid temperature: (a) 0-3 s and (b) 0-15 s.

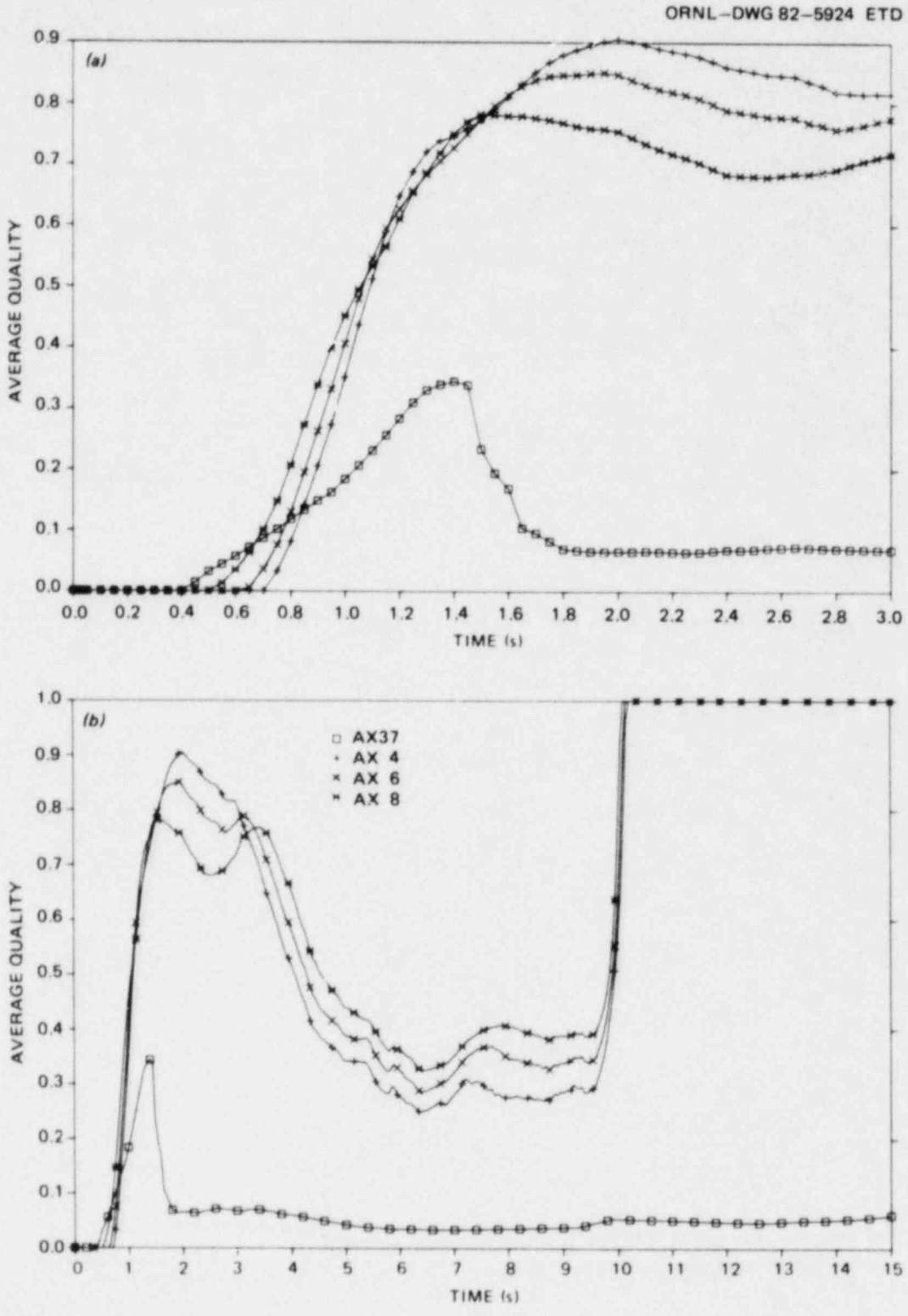

Fig. 4.34. Comparison of calculated THTF conditions and RELAP4 reactor hot channel DECLB prediction (square symbols) – lower core fluid quality: (a) 0–3 s and (b) 0–15 s.

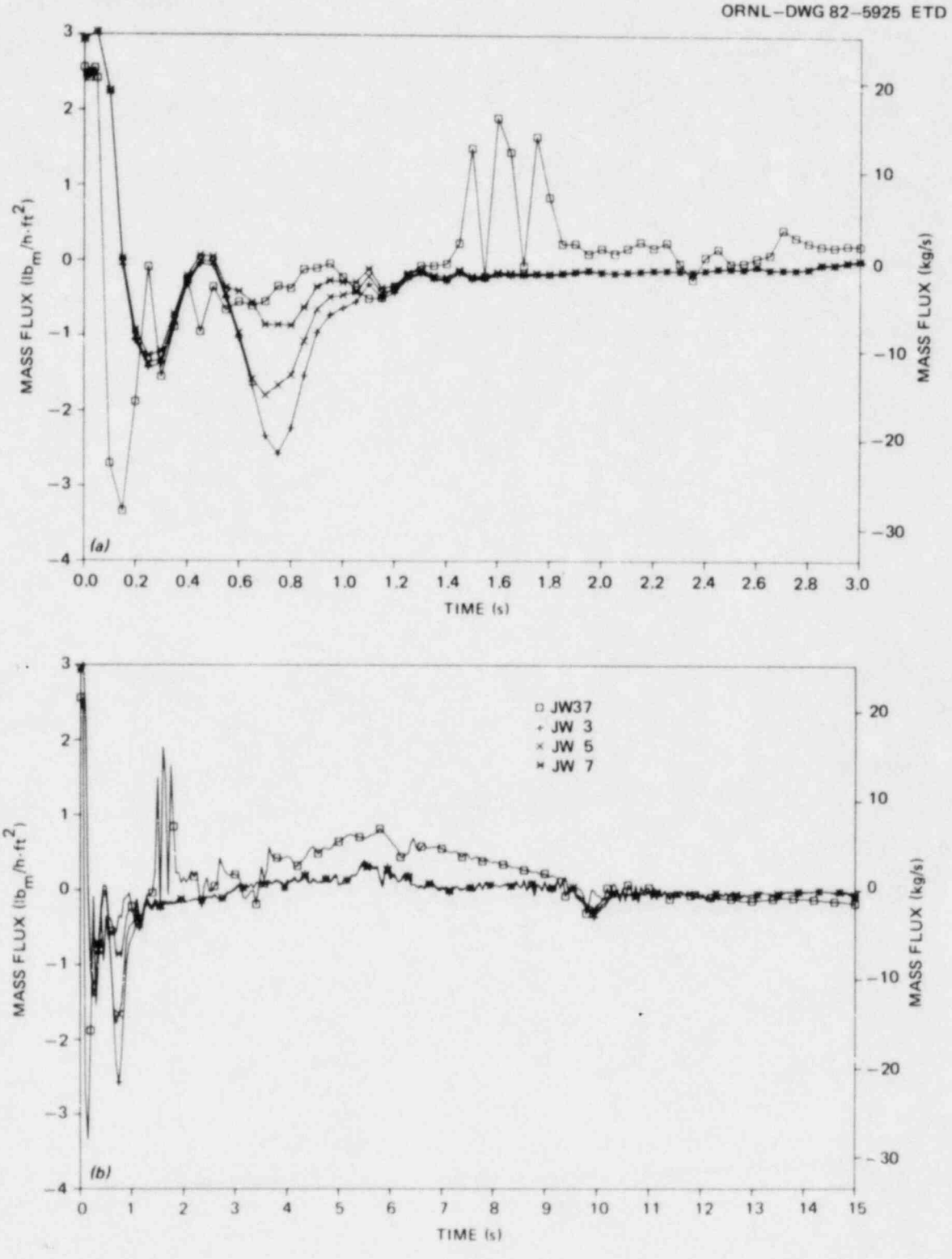

Fig. 4.35. Comparison of calculated THTF conditions and RELAP4 reactor hot channel DECLB prediction (square symbols) – lower core mass flux: (a) 0–3 s and (b) 0–15 s.

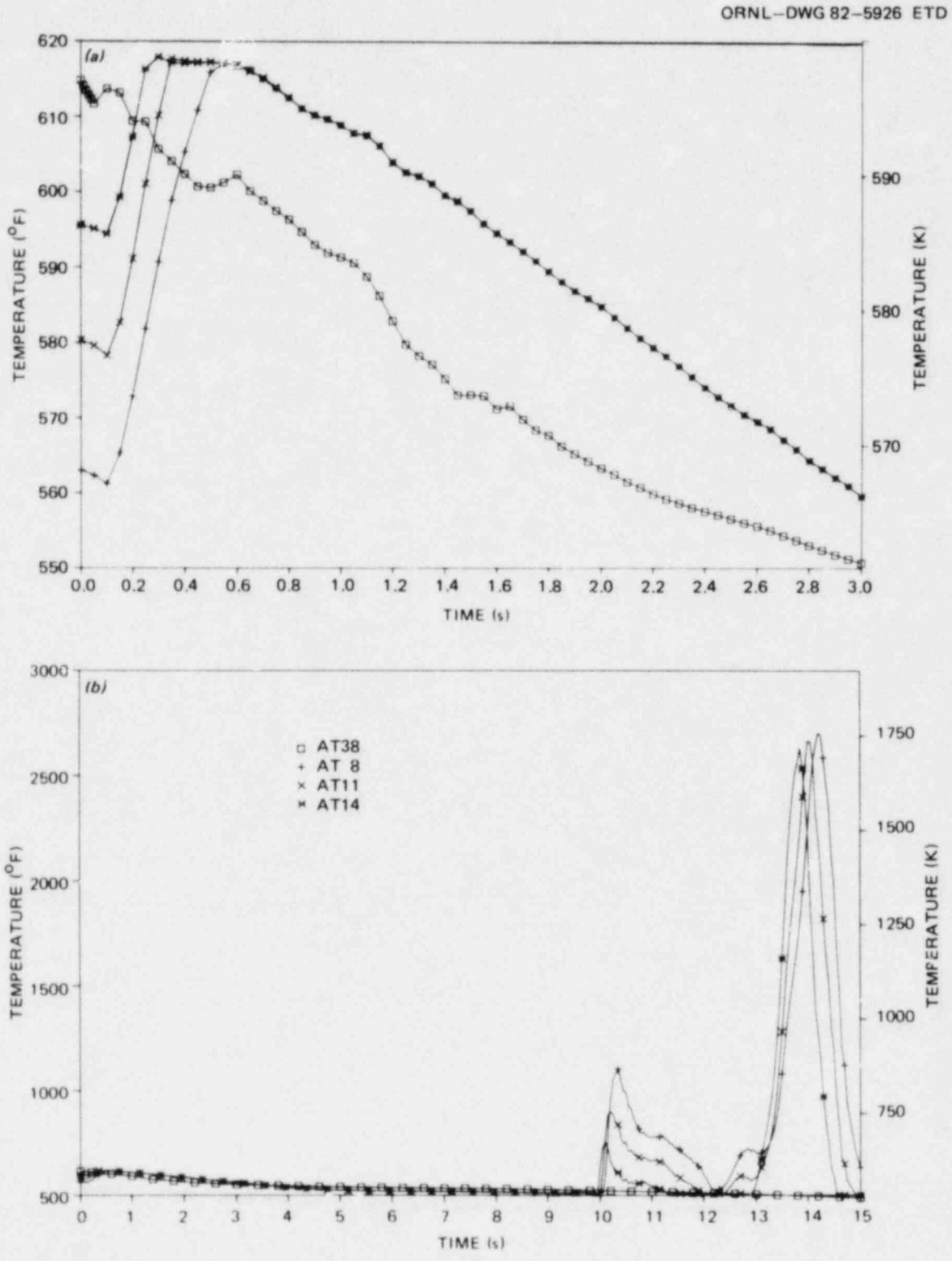

Fig. 4.36. Comparison of calculated THTF conditions and RELAP4 reactor hot channel DECLB prediction (square symbols) - middle core fluid temperature: (a) 0-3 s and (b) 0-15 s.

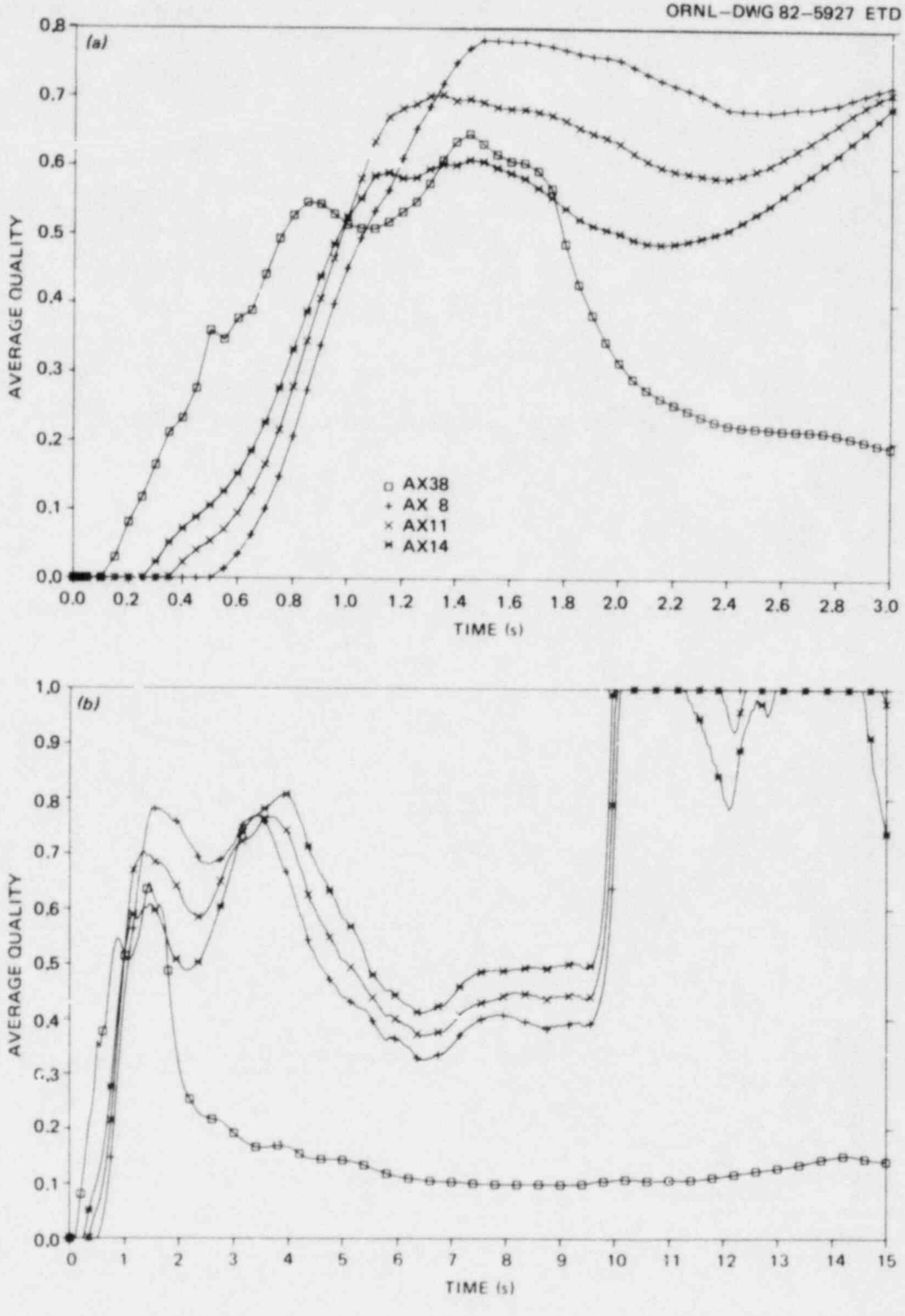

Fig. 4.37. Comparison of calculated THTF conditions and RELAP4 reactor hot channel DECLB prediction (square symbols) – middle core fluid quality: (a) 0–3 s and (b) 0–15 s.

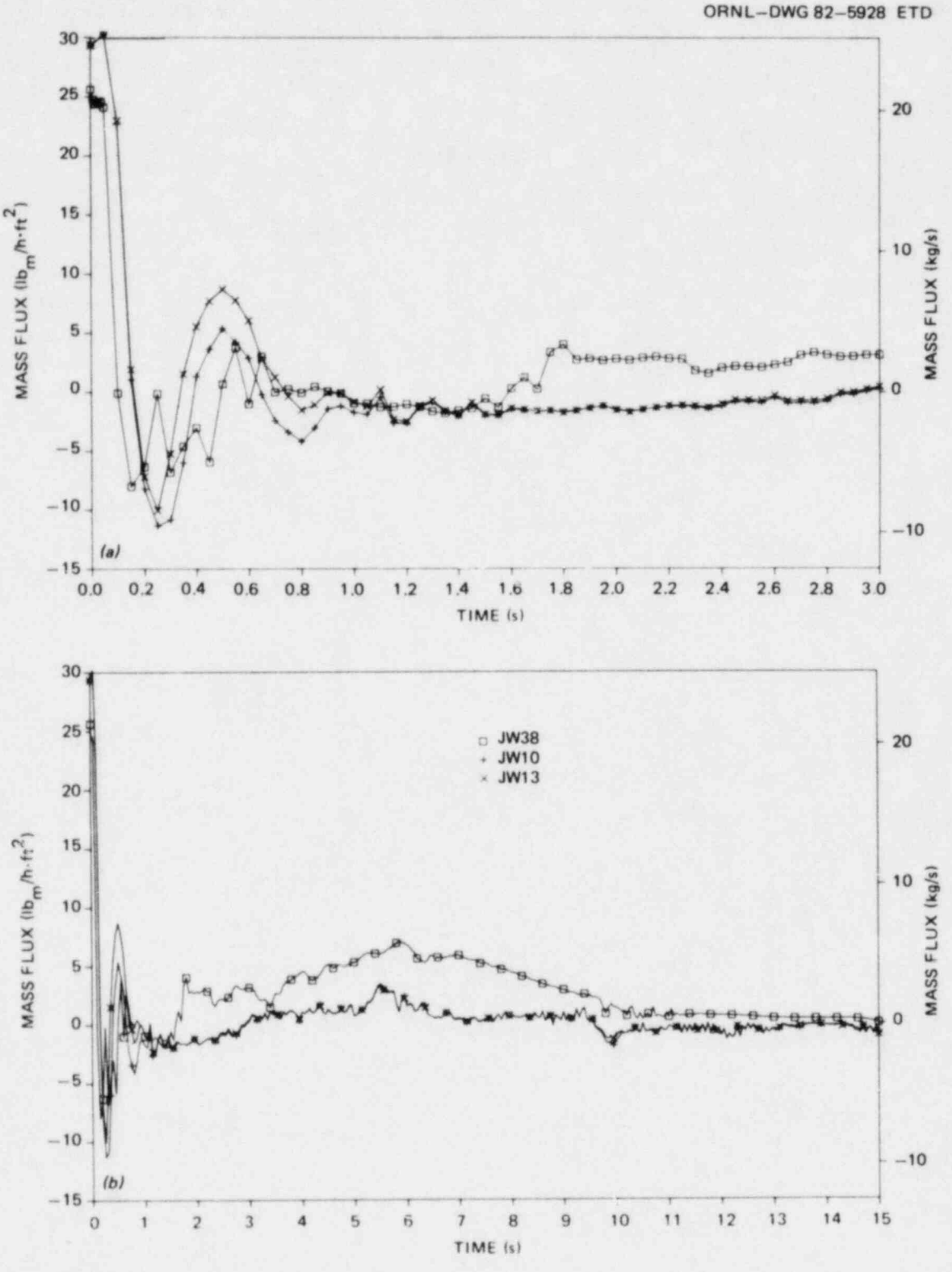

Fig. 4.38. Comparison of calculated THTF conditions and RELAP4 reactor hot channel DECLB prediction (square symbols) – middle core mass flux: (a) 0–3 s and (b) 0–15 s.

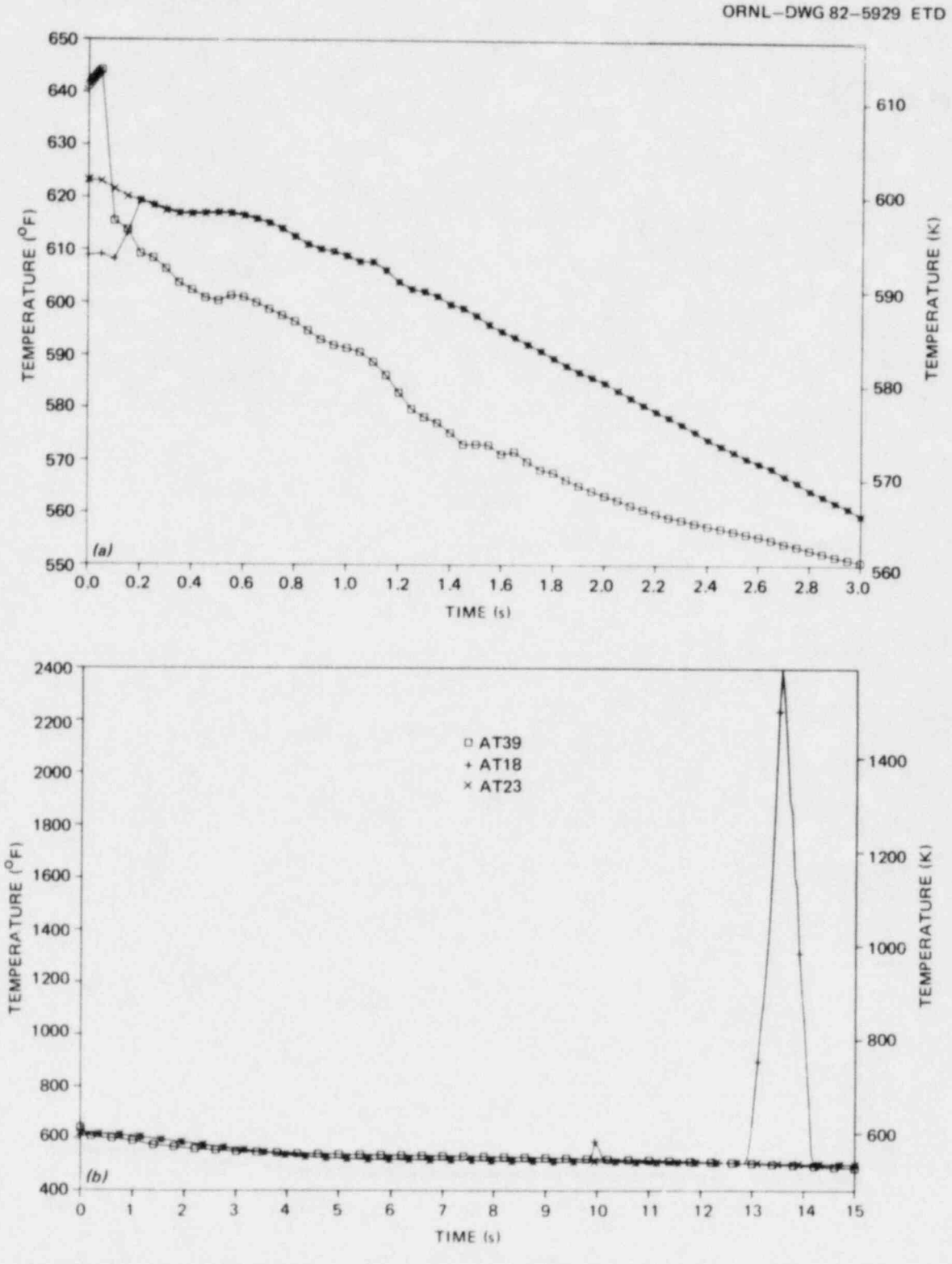

Fig. 4.39. Comparison of calculated THTF conditions and RELAP4 reactor hot channel DECLB prediction (square symbols) – upper core fluid temperature: (a) 0–3 s and (b) 0–15 s.

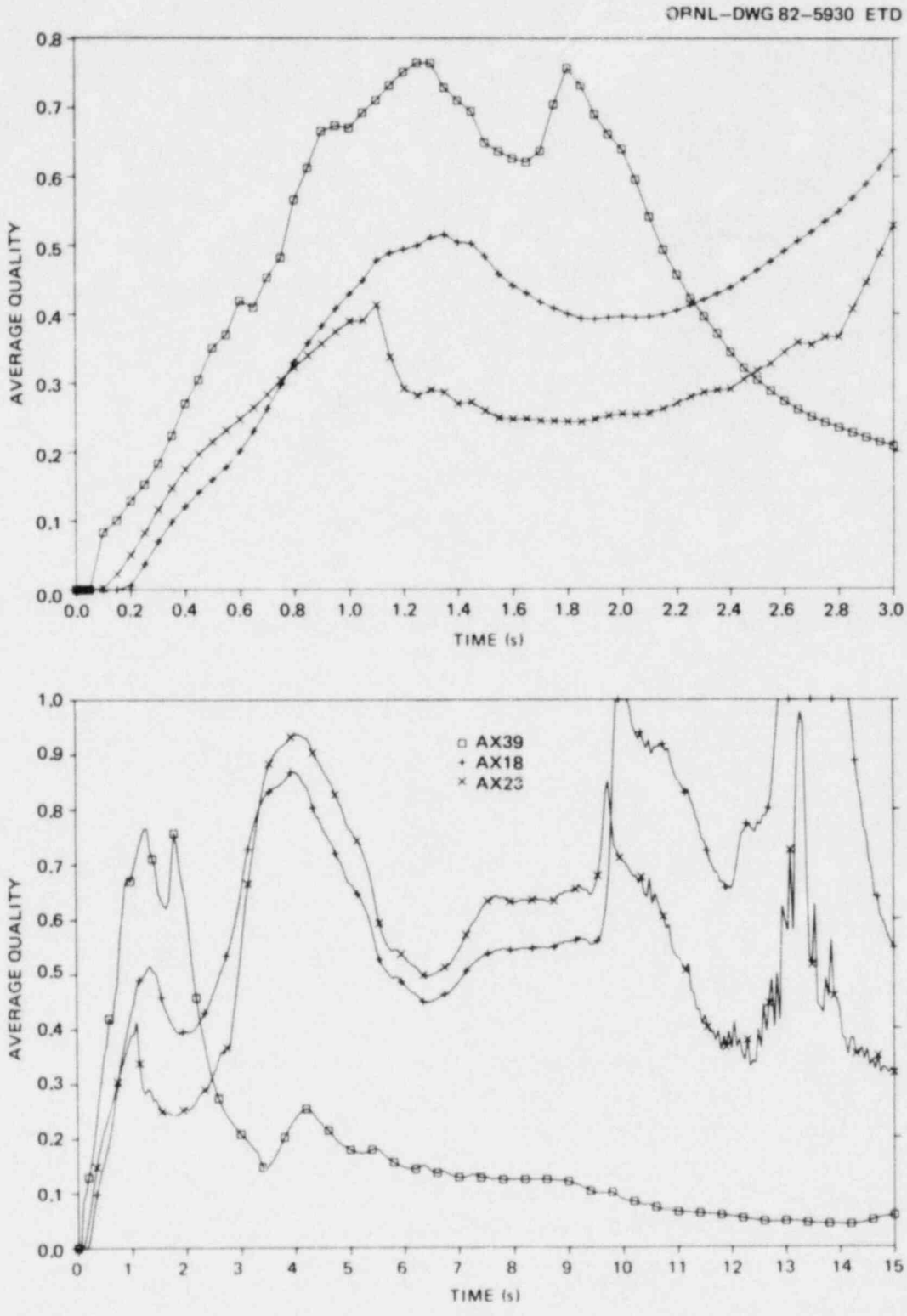

Fig. 4.40. Comparison of calculated THTF conditions and RELAP4 reactor hot channel DECLB prediction (square symbols) – upper core fluid quality: (a) 0–3 s and (b) 0–15 s.

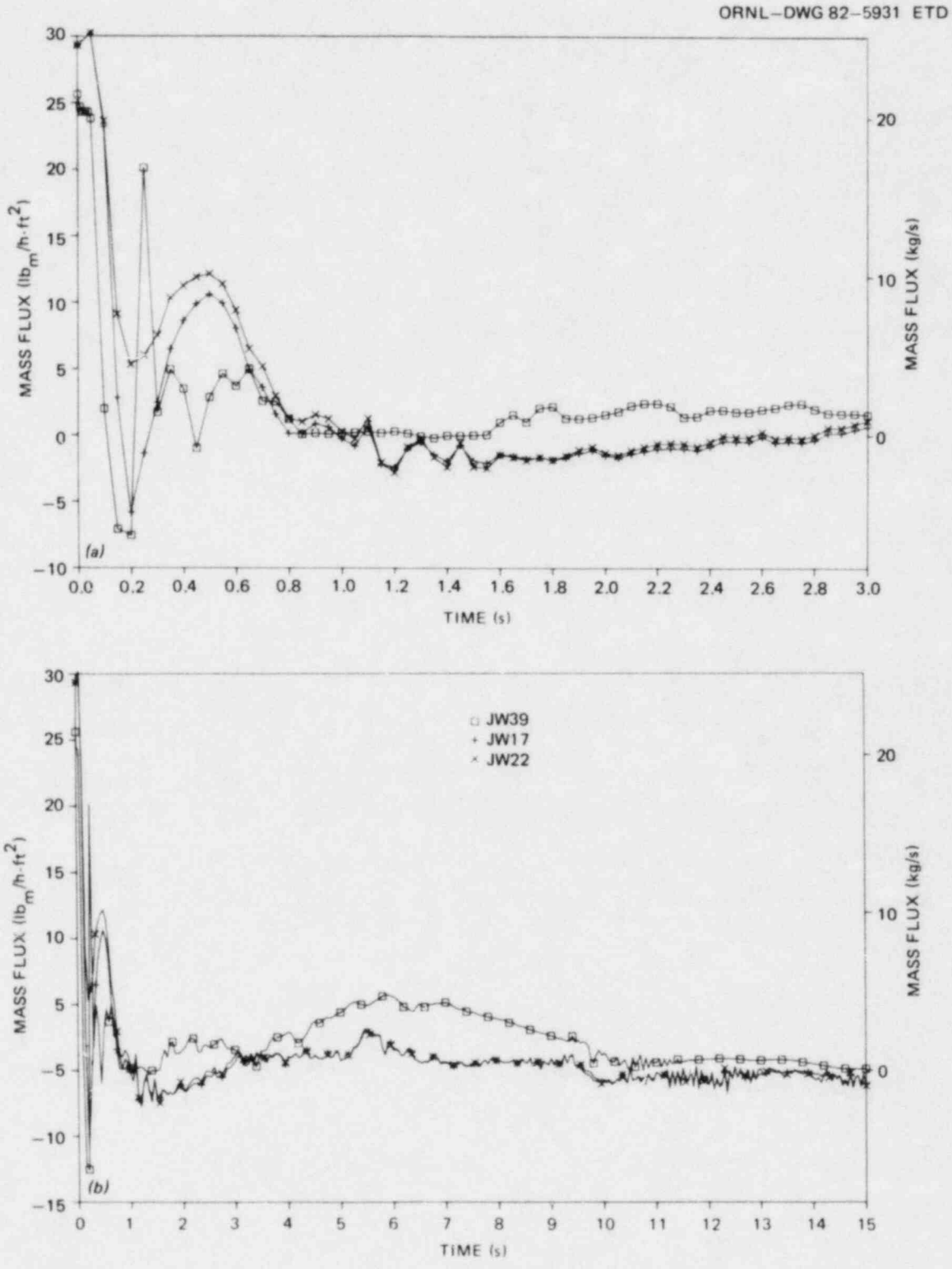

Fig. 4.41. Comparison of calculated THTF conditions and RELAP4 reactor hot channel DECLB prediction (square symbols) -- upper core mass flux: (a) 0-3 s and (b) 0-15 s.

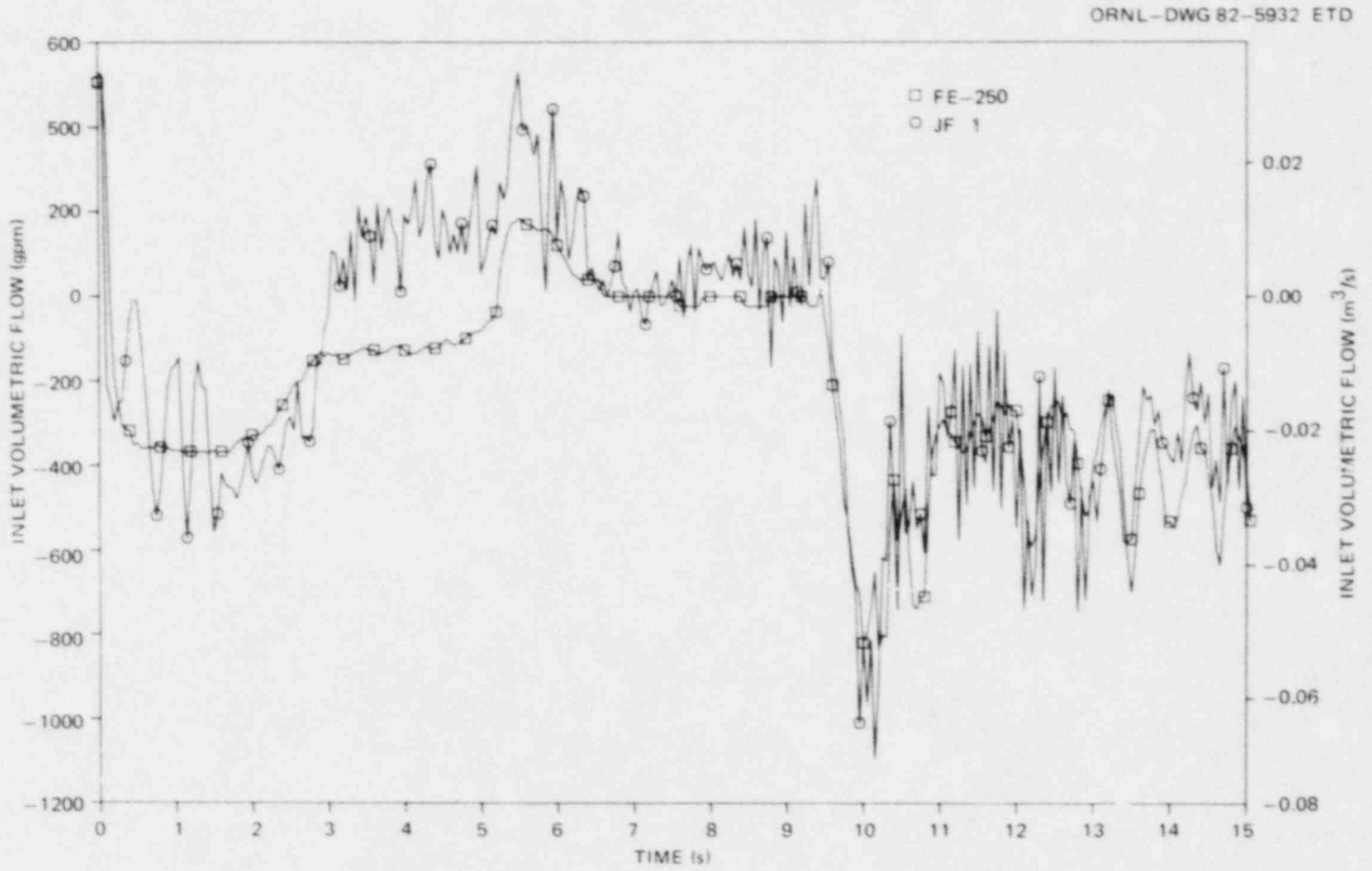

Fig. 4.42. Comparison of measured (square symbols) and calculated THTF fluid conditions – inlet spool-piece volumetric flow (gpm).

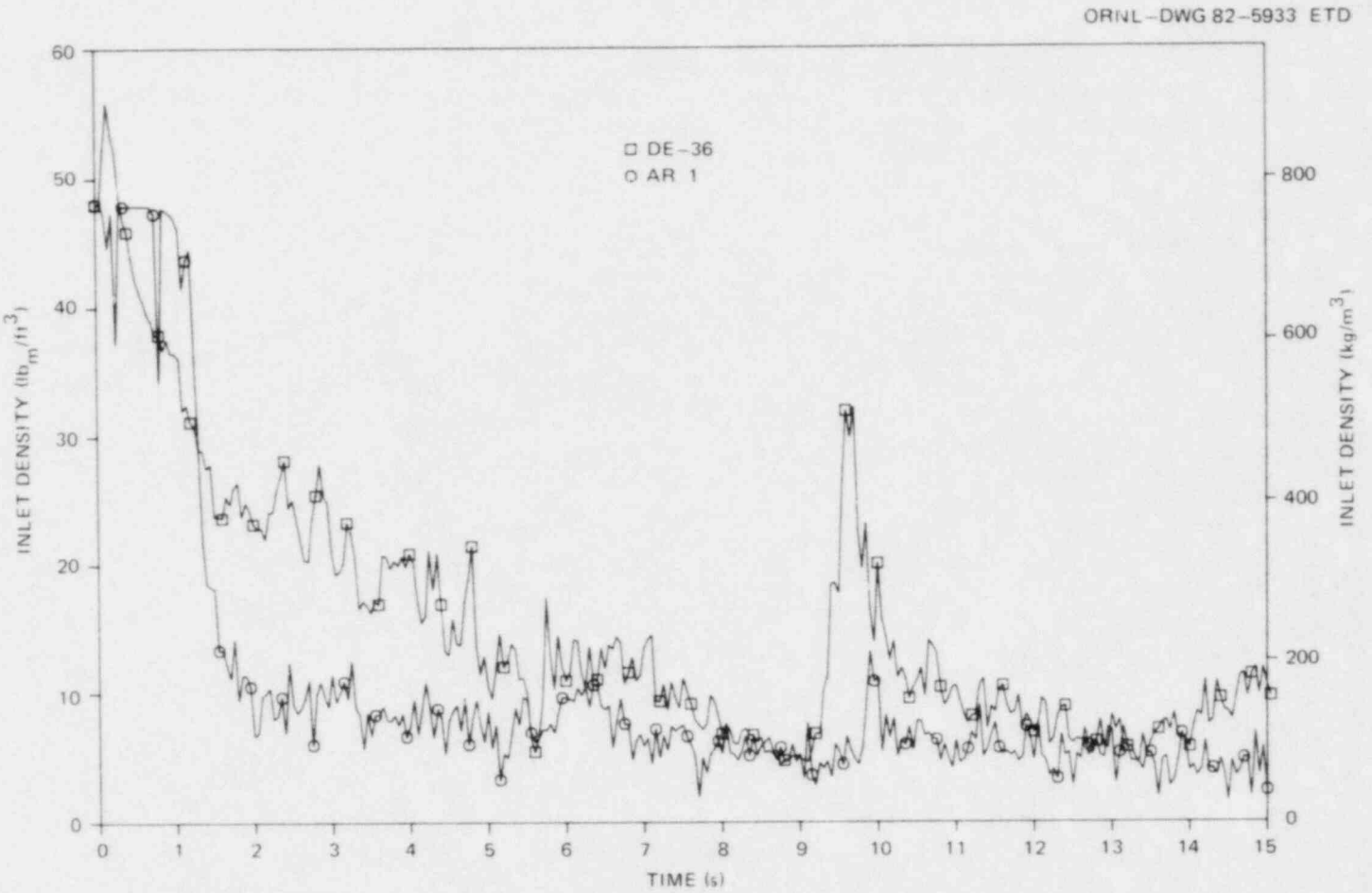

Fig. 4.43. Comparison of measured (square symbols) and calculated THTF fluid conditions – inlet spool-piece fluid density.

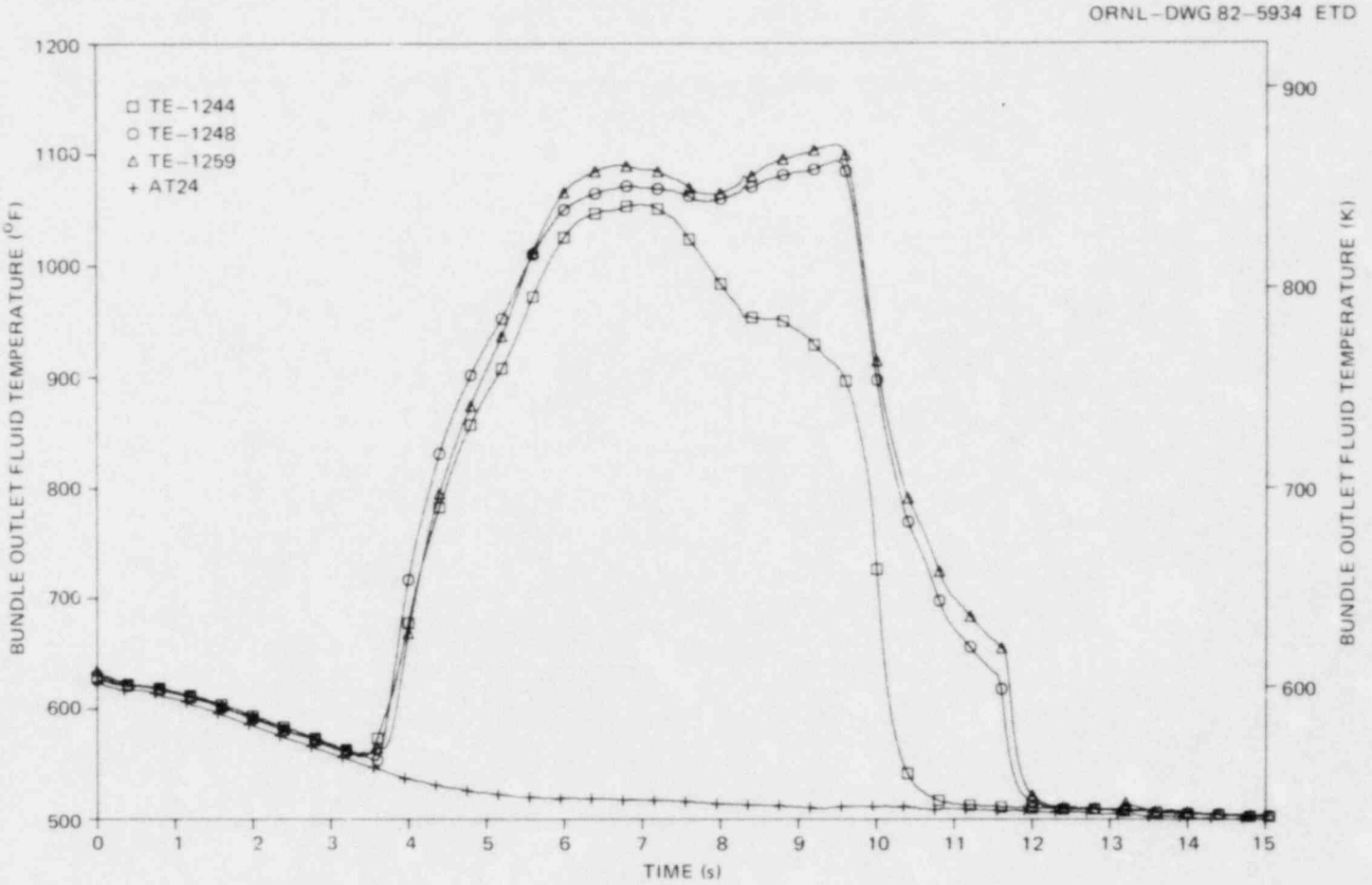

Fig. 4.44. Comparison of measured (square, octagon, and triangle symbols) and calculated THTF fluid conditions – fluid temperatures in bundle just above [2.54-cm (1-in.)] heated length.

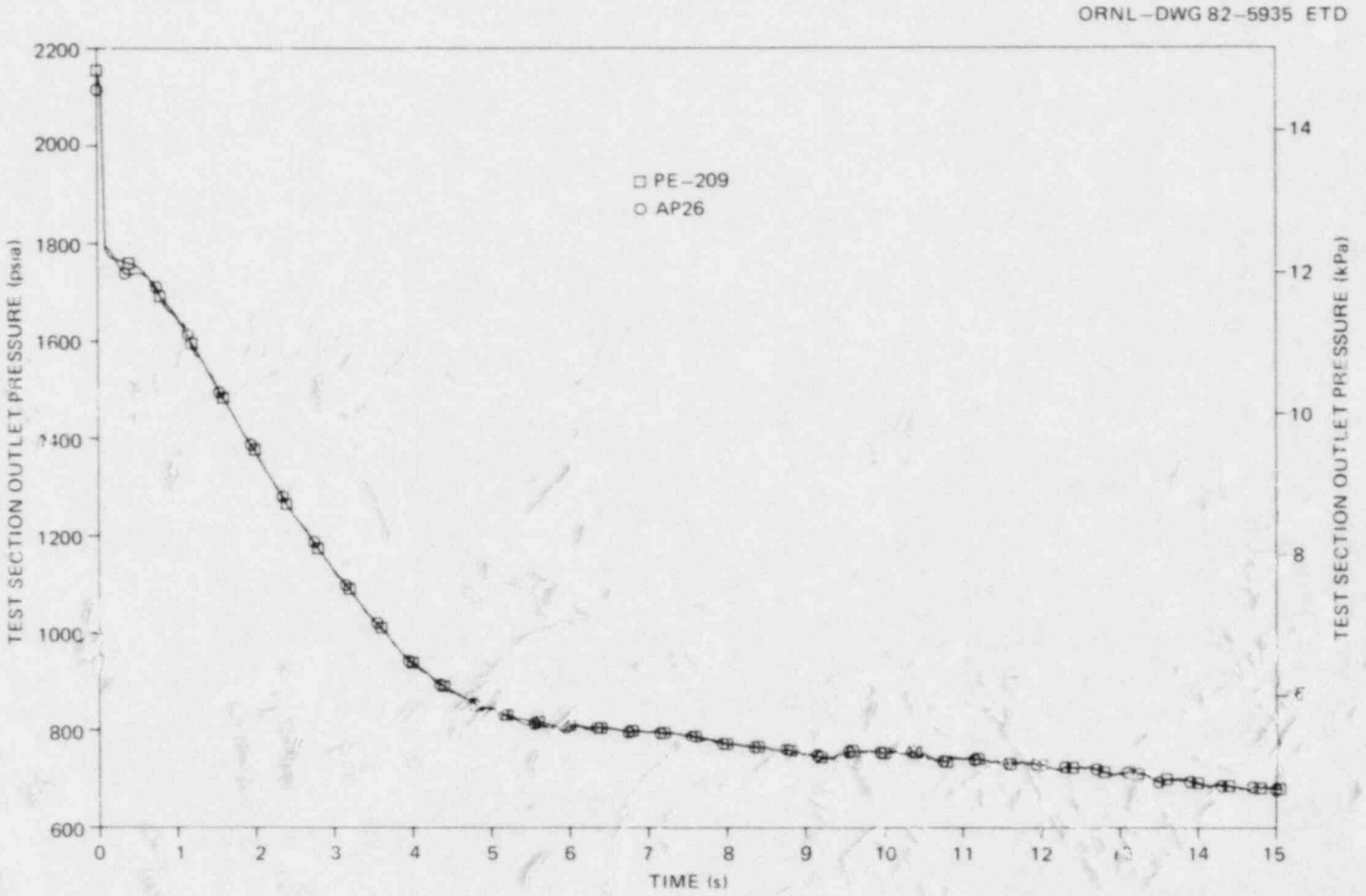

Fig. 4.45. Comparison of measured (square symbols) and calculated THTF fluid conditions – outlet spool-piece pressure.

5. COMPARISON OF TEST 3.05.5B WITH EARLIER THTF TESTS

Prior to 1980, a number of DECLB simulations had been performed in the THTF (Refs. 4, 15, and 16). Most of these tests were aimed at determining the effects of various parameters, such as bundle outlet temperature and power, on the behavior of the FRS. As described in Sec. 2.1, the bundle in the THTF for these tests had rod diameter and pitch characteristic of 15 x 15 PWR fuel assemblies. The rod bundle that was installed in the latter part of 1979 has rod diameter and pitch characteristic of 17 x 17 PWR fuel assemblies. A question of interest to the NRC is whether this difference in geometry produced any significant variations in FRS behavior. This question is addressed in this chapter.

Representative FRS surface heat fluxes and surface temperatures for Test 3.05.5B were presented in Figs. 2.23–2.36. A statistical summary of the key features of the FRS behavior in Test 3.05.5B is contained in Table 5.1, and a description of the FRS rod/path thermocouple naming convention is contained in Table 5.2. Restrictions must be placed on the power supplied to the FRS to avoid exceeding the rod temperature safety limit of 1089 K (1500°F). These restrictions make it impossible to attempt to simulate maximum nuclear fuel rod clad temperatures with our FRS. The remainder of this discussion will therefore be focused on time to DNB.

Upon break initiation, subcooled depressurization causes the system pressure to drop precipitously until it saturates the fluid at the test section outlet (Fig. 2.18). Flow at the test section inlet reverses itself (Fig. 2.17) immediately and begins to flow toward the inlet break (at the inlet, negative flow implies flow out of the test section; positive flow indicates flow in the same direction as at steady state). During the first 2 s, the outlet flow (Fig. 2.21), while dipping low, remains out of the test section (i.e., positive, the same direction as the steady state). Because flow at both the inlet and the outlet is out of the test section, a region of zero flow must exist somewhere inside the test section. One would expect this region of low flow to be conducive to DNB.

Because the times to DNB form a uniform progression from shortest to longest as one moves from the top to the bottom of the bundle, one might

Table 5.1. Time-to-DNB summary: all levels

Level	Number of sheath thermocouples			Average time to DNB (s)	Standard deviation
	At this level	Indicating DNB	To DNB < 1 s		
A	19	19	2	1.1319	0.10953
B	40	40	8	1.0835	0.14538
C	47	46	31	1.0004	0.10590
D	79	70	46	0.9777	0.14753
E	75	75	61	0.9040	0.14740
F	43	42	38	0.7429	0.13658
G	20	20	19	0.6175	0.15067

Level	Maximum time to DNB (s)	Thermocouple in maximum time	Maximum temperature (°F)	Time to maximum temperature (s)	Thermocouple to maximum temperature
A	1.3362	TE-325BA	1365.4	20.8986	TE-343BA
B	1.3759	TE-305AB	1387.4	17.9993	TE-343BB
C	1.2773	TE-321BC	1404.3	18.0493	TE-355BC
D	1.3427	TE-321BD	1435.8	21.2985	TE-350AD
E	1.5388	TE-362AE	1359.4	16.7496	TE-353BE
F	1.1725	TE-328CF	1335.0	14.9998	TE-353BF
G	1.1868	TE-342AG	1276.2	9.4999	TE-358CG

Table 5.2. Rod sheath thermocouple designations

Rod sheath thermocouples are designated according to the following scheme:

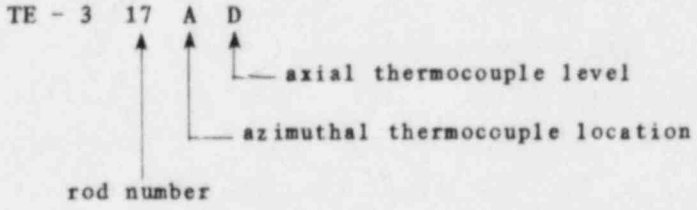

Thus, this designation refers to the sheath thermocouple in rod 17 at level D, azimuthal location A. (Rod numbers are shown in Fig. 2.4.)

be inclined to suggest that the low-flow region is near the top of the bundle. However, other factors may be responsible for the earliest time to DNB being at the uppermost level of the bundle (level G). Fluid at the top of the bundle is hotter at break initiation and will saturate more quickly than fluid at the bottom of the bundle. Because the bundle's axial power profile is uniform, this would lead one to expect higher fluid enthalpies and qualities in the upper bundle, and therefore earlier times to DNB. Thus, it seems reasonable to attribute the DNB behavior in the experiment to a combination of the flow pattern, initial fluid temperature profile, and flat axial power profile.

The times to DNB listed in Table 5.1 are all within the range of times to DNB observed in the tests performed with the earlier (15 x 15-type) FRS bundle. The axial profiles of these times to DNB were, however, somewhat different. In the first bundle, the upper portion tended to experience a relatively late DNB and in some cases no DNB at all. The lower portions of the bundle experienced DNB earlier, but still not as soon as the middle of the bundle, which had the shortest times to DNB. This difference in the locations that first experienced DNB between the earlier and current bundles is probably due to the difference in axial power profiles.

The axial power profile in the earlier bundle (Fig. 2.10) is a sharply peaked cosine distribution having a local-to-average power ratio of 1.67 at the center and dropping all the way to 0.422 at the ends. The flow pattern and inlet and outlet temperature for Test 3.05.5B were similar to those of the earlier tests. However, in the earlier tests the input power at the upper end of the bundle was too low to achieve the early DNB seen in this test. Rather, the center of the earlier bundle, with its high-power region, had times to DNB similar to those seen in the upper bundle in Test 3.05.5B. In the earlier tests, the lower portion of the bundle experienced earlier DNB than the upper portion, even though they had the same local power levels, because of the flow pattern. In the earlier tests, the region of low-to-zero flow was believed to reside slightly above the middle of the bundle; as fluid flowed down through the high heat flux zone, it gained sufficient enthalpy and quality to eventually produce DNB in the lower bundle, in spite of its lower local power. Thus, the

difference in power profiles appears to be the probable cause for the observed differences in time to DNB.

Because the times to DNB of Test 3.05.5B fall within the times to DNB of tests with the earlier bundle and because the difference in the location of the earliest times to DNB seems to be due to the difference in axial power profiles, we may conclude that no differences in behavior have been seen between the 15 x 15-type bundle and the 17 x 17-type bundle that can be attributed to the difference in geometries. This does not mean that such effects do not exist. A series of eight parametric tests was needed with the earlier bundle to discern the effects of outlet temperature and power.[16] A similar parametric series might reveal some geometric effects. All that can be said at this point is that any such effects are not large enough to manifest themselves in the single DECLB simulation test conducted with a 17 x 17-type bundle.

6. CONCLUSIONS

On July 3, 1980, an experiment, designated Test 3.05.5B, was performed at the ORNL THTF that was intended to simulate the conditions that would occur in the core of a PWR during a DECLB accident. The objectives of the experiment were to obtain data on time to DNB and to provide data that can be used to assess transient reactor analysis codes. The analysis documented in this report is directed at the first of these objectives.

Two types of calculations were performed to determine the relationship of the times to DNB of the FRS in the experiment to the times to DNB that would be experienced by a nuclear fuel rod exposed to the same hydrodynamic environment. Back calculations showed that nuclear fuel rods with nominal or wide gas gaps between fuel pellet and clad could not have experienced the surface heat flux and surface temperature transients experienced by the FRS. Forward calculations indicated that such nuclear fuel rods would have experienced DNB earlier than did the FRS in the experiment, if the nuclear fuel rods had the same initial power as did the FRS. The forward calculation showed that a nuclear fuel rod with no gas gap and with the same initial power would have experienced DNB later than the FRS. When the initial power of the nuclear fuel rod differed from that of the FRS, the results on time to DNB corresponded to the power: higher power implied earlier times to DNB, and lower power implied later times to DNB. If the hydrodynamic conditions that existed during the experiment could be taken as characteristic of those of an actual DECLB accident, then these results would indicate that the ends of the reactor core would experience DNB later than the experiment (i.e., later than 1.1 s), while the middle of the reactor core would experience DNB earlier than the experiment (i.e., earlier than 0.6 s).

Calculations were made of the hydrodynamic conditions extant in the THTF during the experiment and predicted to occur during an actual reactor accident. However, the uncertainties associated with these calculations are believed to be much too large to allow any conclusions to be drawn.

A comparison of the results of this experiment, which used an FRS bundle with 17 x 17-type geometry, to the results of earlier experiments,

which used an FRS bundle with 15 x 15-type geometry, revealed no differences in FRS behavior that could be attributed to the difference in geometry. However, our ability to discern such effects is limited given only one test in 17 x 17-type geometry.

REFERENCES

1. D. K. Felde et al., *Facility Description — Thermal-Hydraulic Test Facility (THTF) Mod 3*, ORNL/TM-7842 (1982).

2. R. C. Hagar and R. A. Hedrick, *PINSIM — MOD 1: A Nuclear Fuel Pin/Electric Fuel Pin Simulator Transient Analysis Code*, ORNL/NUREG/TM-291 (1980).

3. D. J. Varacalle, Jr. et al., *Local Conditions and Uncertainty Band Calculations for Semiscale Test S-02-9*, CDAP-TR-048 (1979).

4. W. G. Craddick et al., *PWR Blowdown Heat Transfer Separate-Effects Program Data Evaluation Report — Heat Transfer for THTF Test Series 100*, ORNL/NUREG-45 (1978).

5. *Project Description, ORNL PWR Blowdown Heat Transfer Separate-Effects Program — Thermal-Hydraulic Test Facility (THTF)*, ORNL/NUREG/TM-218 (1978).

6. *Addendum 1, Project Description: ORNL PWR Blowdown Heat Transfer Separate-Effects Program — Thermal-Hydraulic Test Facility (THTF)*, ORNL/NUREG/TM-218/A1 (1979).

7. M. Berman et al., "UHI RELAP Model Development," *Light-Water Reactor Safety Research Program, Quart. Prog. Rep. July-September 1978, Vol. 9*, SAND79-0359, R3 (1979).

8. C. B. Mullins et al., *ORNL Rod Bundle Heat Transfer Test Data, Vol. 6. Thermal-Hydraulic Test Facility Experimental Data Report for Test 3.05.5B — Double-Ended Cold-Leg Break Simulation*, ORNL/NUREG/TM-407/V6 (1982).

9. L. J. Ott and R. A. Hedrick, *ORINC — A One-Dimensional Implicit Approach to the Inverse Heat Conduction Problem*, ORNL/NUREG-23 (1977).

10. L. J. Ott and R. A. Hedrick, *ORTCAL — A Code for THTF Heater Rod Thermocouple Calibration*, ORNL/NUREG-51 (1979).

11. R. C. Hagar, *Developmental Verification of PINSIM-MOD2*, ORNL/NUREG/TM-431 (1981).

12. R. C. Hagar, *Nuclear Pin Simulation Analysis of THTF Test 105*, ORNL/NUREG/TM-400 (1981).

13. Westinghouse, *Reference Core Report, 17 x 17, Optimized Fuel Assembly, Vol. 1*, WCAP-9500 (1980).

14. S. B. Cliff, *RLPSFLUX, RELAP with Surface Flux Modifications*, ORNL/NUREG/CSD-5 (1978).

15. R. A. Hedrick et al., *PWR Blowdown Heat Transfer Separate-Effects Program Data Evaluation Report — System Response for Thermal-Hydraulic Test Facility Test Series 100*, ORNL/NUREG-19 (1977)

16. C. B. Mullins et al., *PWR Blowdown Heat Transfer Separate-Effects Program Data Evaluation Report — THTF Test Series II*, ORNL/NUREG-53 (1979).

Appendix A

BACK-CALCULATION METHOD

(Reproduced from ORNL/NUREG/TM-400, Reference 12)

A unique feature of PINSIM is its ability to determine the power required to force a user-defined pin model to experience user-supplied surface conditions. Relevant to this report is its ability to determine the power required to force a model of a nuclear fuel pin to experience surface heat flux and surface temperature transients of an electric FPS. The calculational technique, referred to here as "back calculation," is described briefly in the following paragraphs.

The parabolic differential equation used to model the transfer of heat in a solid with an internal heat source is

$$\bar{\nabla}\cdot K\bar{\nabla}T + \dot{q}''' = \rho C_p \frac{\partial T}{\partial t} . \tag{A.1}$$

Integration of Eq. (A.1) over an incremental volume V_i yields

$$\int_{V_i} \bar{\nabla}\cdot k_i\bar{\nabla}T_i \, dV_i + \int_{V_i} \dot{q}_i''' \, dV_i = \int_{V_i} \rho_i C_{p_i} \frac{\partial T_i}{\partial t} \, dV_i . \tag{A.2}$$

Assuming that $\dot{q}_i'''$, ρ_i, C_{p_i}, and $\partial T_i/\partial t$ are all constant over V_i reduces Eq. (A.2) to

$$\int_{V_i} \bar{\nabla}\cdot k_i\bar{\nabla}T \, dV_i + \dot{q}_i'''V_i = \rho_i C_{p_i} V_i \frac{\partial T_i}{\partial t} . \tag{A.3}$$

Application of the divergence theorem to the first term allows this result to be written as

$$\int_{A_i} k_i\bar{\nabla}T\cdot d\bar{A} + \dot{q}'''V_i = \rho_i C_{p_i} V_i \frac{\partial T_i}{\partial t} . \tag{A.4}$$

Restricting the application of these results to cylindrical geometries allows expansion of the gradient of T in cylindrical coordinates. This

yields

$$\int_{A_i} k_i \left(\frac{\partial T_i}{\partial r} \tilde{r} + \frac{1}{r} \frac{\partial T}{\partial \theta} \tilde{\theta} + \frac{\partial T}{\partial Z} \tilde{Z} \right) \cdot d\tilde{A} + \dot{q}'''V_i = \rho_i C_{p_i} V_i \frac{\partial T_i}{\partial t} . \quad (A.5)$$

By assuming that axial and azimuthal temperature gradients are insignificant when compared with the radial temperature gradient, one can reduce Eq. (A.5) to

$$\int_{A_i} k_i \frac{\partial T}{\partial r} \tilde{r} \cdot d\tilde{A} + \dot{q}'''V_i = \rho_i C_{p_i} V_i \frac{\partial T_i}{\partial t} . \quad (A.6)$$

With the assumption that $k_i(\partial T/\partial r)$ is a function of r and t only, Eq. (A.6) reduces to

$$2\pi r_o \, k_o Z_o \left. \frac{\partial T}{\partial r} \right|_{r_o} - 2\pi r_{in} \, k_{in} Z_{in} \left. \frac{\partial T}{\partial r} \right|_{r_{in}} + \dot{q}'''V_i = \rho_i C_{p_i} V_i \frac{\partial T_i}{\partial t} . \quad (A.7)$$

Assume now that the volumetric properties of the incremental volume V_i are located in space on a surface of no thickness at a radius r_i. This surface is referred to as a "node." This assumption requires that the heat flow between adjacent nodes be constant at any r between the nodal radii. Thus,

$$r_{out} \left. \frac{\partial T}{\partial r} \right|_{r_{out}} = \frac{T_i - T_{i+1}}{\ell n \, (r_{i+1}/r_i)} , \quad (A.8)$$

and

$$r_{in} \left. \frac{\partial T}{\partial r} \right|_{r_{in}} = \frac{T_{i-1} - T_i}{\ell n \, (r_i/r_{i-1})} . \quad (A.9)$$

This assumption also allows us to write

$$\frac{\partial T_i}{\partial t} = \frac{T_i(t) - T_i(t - \Delta t)}{\Delta t} . \quad (A.10)$$

Inserting the relationships (A.8), (A.9), and (A.10) into Eq. (A.7) yields

$$- \frac{\bar{k}_{i-1,i} 2\pi Z}{\ell n\ (\bar{r}_i/\bar{r}_{i-1})} (T_i - T_{i-1}) + \frac{\bar{k}_{i,i+1} 2\pi Z}{\ell n\ (\bar{r}_{i+1}/\bar{r}_i)} (T_{i+1} - T_i)$$

$$+ \dot{q}'''\pi Z(r_i^2 - r_{i-1}^2) = \rho C_p \pi Z(r_i^2 - r_{i-1}^2)$$

$$\times \frac{T_i(t) - T_i(t - \Delta t)}{\Delta t} . \quad (A.11)$$

Factoring out πZ and using an implicit formulation allows Eq. (A.11) to be written as

$$- \frac{2\bar{k}_{i-1,i}}{\ell n\ (\bar{r}_i/\bar{r}_{i-1})} [T_i(t) - T_{i-1}(t)]$$

$$+ \frac{2\bar{k}_{i,i+1}}{\ell n\ (\bar{r}_{i+1}/\bar{r}_i)} [T_{i+1}(t) - T_i(t)] + \dot{q}_i'''(r_i^2 - r_{i-1}^2)$$

$$= \rho C_{p_i} (r_i^2 - r_{i-1}^2) \frac{T_i(t) - T_i(t - \Delta t)}{\Delta t} . \quad (A.12)$$

Collecting terms in Eq. (A.12) yields

$$\left[\frac{2\bar{k}_{i-1,i}}{\ell n\ (\bar{r}_i/\bar{r}_{i-1})}\right] T_{i-1}(t) + \left[- \frac{2\bar{k}_{i-1,i}}{\ell n\ (\bar{r}_i/\bar{r}_{i-1})} - \frac{\rho C_{p_i}(r_i^2 - r_{i-1}^2)}{\Delta t}\right.$$

$$\left. - \frac{2\bar{k}_{i,i+1}}{\ell n\ (\bar{r}_{i+1}/\bar{r}_i)}\right] T_i(t) + \left[\frac{2\bar{k}_{i,i+1}}{\ell n\ (\bar{r}_{i+1}/\bar{r}_i)}\right] T_{i+1}(t)$$

$$= -\dot{q}_i'''(r_i^2 - r_{i-1}^2) - \left[\frac{\rho C_{p_i}(r_i^2 - r_{i-1}^2)}{\Delta t}\right] T_i(t - \Delta t) . \quad (A.13)$$

Equation (A.13) may be conveniently written as

$$\bar{A}\,\bar{T} = \bar{B}\ , \tag{A.14}$$

where $\bar{A}$ is the tridiagonal coefficient matrix of the system:

$$\bar{A} = \begin{bmatrix} a_{1,1} & a_{1,2} & 0 & 0 & \cdots & 0 & 0 & 0 & 0 & 0 \\ a_{2,1} & a_{2,2} & a_{2,3} & 0 & \cdots & 0 & 0 & 0 & 0 & 0 \\ 0 & a_{3,2} & a_{3,3} & a_{3,4} & \cdots & 0 & 0 & 0 & 0 & 0 \\ \vdots & & & & & & & & & \\ 0 & 0 & 0 & 0 & \cdots & a_{n-3,n-4} & a_{n-3,n-3} & a_{n-3,n-2} & 0 & 0 \\ 0 & 0 & 0 & 0 & \cdots & 0 & a_{n-2,n-3} & a_{n-2,n-2} & a_{n-2,n-1} & 0 \\ 0 & 0 & 0 & 0 & \cdots & 0 & 0 & a_{n-1,n-2} & a_{n-1,n-1} & a_{n-1,n} \\ 0 & 0 & 0 & 0 & \cdots & 0 & 0 & 0 & a_{n,n-1} & a_{n,n} \end{bmatrix} \tag{A.15}$$

where

$$a_{i,i} = -\frac{2\bar{k}_{i-1,i}}{\ell n\,(\bar{r}_i/\bar{r}_{i-1})} - \frac{\rho C_{p_i}(r_i^2 - r_{i-1}^2)}{\Delta t} - \frac{2\bar{k}_{i,i+1}}{\ell n\,(\bar{r}_{i+1}/\bar{r}_i)}\ , \tag{A.16}$$

$$a_{i,i+1} = \frac{2\bar{k}_{i,i+1}}{\ell n\,(\bar{r}_{i+1}/\bar{r}_i)}\ , \tag{A.17}$$

$$a_{i,i-1} = \frac{2\bar{k}_{i-1,i}}{\ell n\,(\bar{r}_i/\bar{r}_{i-1})}\ , \tag{A.18}$$

$$a_{n,n} = \frac{2\bar{k}_{n-1,n}}{\ell n\,(\bar{r}_n/\bar{r}_{n-1})} - \frac{\rho C_{p_n}(r_n^2 - r_{n-1}^2)}{\Delta t}$$

$$- 2/[1/r_n h_f(t + \Delta t)] + [\ell n\,(r_n/\bar{r}_n)/k_n]\ . \tag{A.19}$$

$\bar{T}$ is a column vector of unknowns (nodal temperatures at time t):

$$\bar{T} = \begin{bmatrix} T_1 \\ T_2 \\ \cdot \\ \cdot \\ \cdot \\ T_i \\ \cdot \\ \cdot \\ \cdot \\ T_{n-2} \\ T_{n-1} \\ T_n \end{bmatrix} . \qquad \text{(A.20)}$$

$\bar{B}$ is a column vector of knowns:

$$\bar{B} = \begin{bmatrix} b_1 \\ b_2 \\ b_3 \\ \cdot \\ \cdot \\ \cdot \\ b_{n-2} \\ b_{n-1} \\ b_n \end{bmatrix} . \qquad \text{(A.21)}$$

If the nodal heat generation terms $\dot{q}'''$ are expressed as fractions of the total heat generation rate $\dot{Q}$, such that

$$F_i\dot{Q} = \dot{q}_i''' \ , \tag{A.22}$$

the elements of the $\bar{B}$ vector may be written

$$b_i = -F_i\dot{Q}(r_i^2 - r_{i-1}^2) - \left[\frac{\rho_i C_{p_i}(r_i^2 - r_{i-1}^2)}{\Delta t}\right] T_i(t - \Delta t), \ i < n, \tag{A.23}$$

and

$$b_n = -F_n Q(r_n^2 - r_{n-1}^2) - \left[\frac{2}{\dfrac{1}{r_n h_f(t)} + \dfrac{\ell n(r_n/\bar{r}_n)}{k_n}}\right] \times T_b(t - \Delta t) - \left[\frac{\rho_n C_{p_n}(r_n^2 - r_{n-1}^2)}{\Delta t}\right] T_n(t - \Delta t) \ . \tag{A.24}$$

The back-calculational method is iterative and is based on the assumption that the radial and axial power distributions of the pin are fixed and known. The method is illustrated schematically in Fig. A.1.

The matrix form of the conduction equation is given in Eq. (A.14); this equation may be written for a single node as

$$a_{i,i-1}T_{i-1} + a_{i,i}T_i + a_{i,i+1}T_{i+1} + F_i\dot{Q} = b_i \ . \tag{A.25}$$

Assuming that node k is the outermost heat-generating node, F_i for all nodes $i > k$ will be zero. If the outermost node is node m, Eq. (A.25) for node m reduces to

$$a_{m,m-1}T_{m-1} + a_{m,m}T_m = b_m \ . \tag{A.26}$$

Heat transferred between the outermost node and the fluid may be expressed

ORNL-DWG 79-4628 ETD

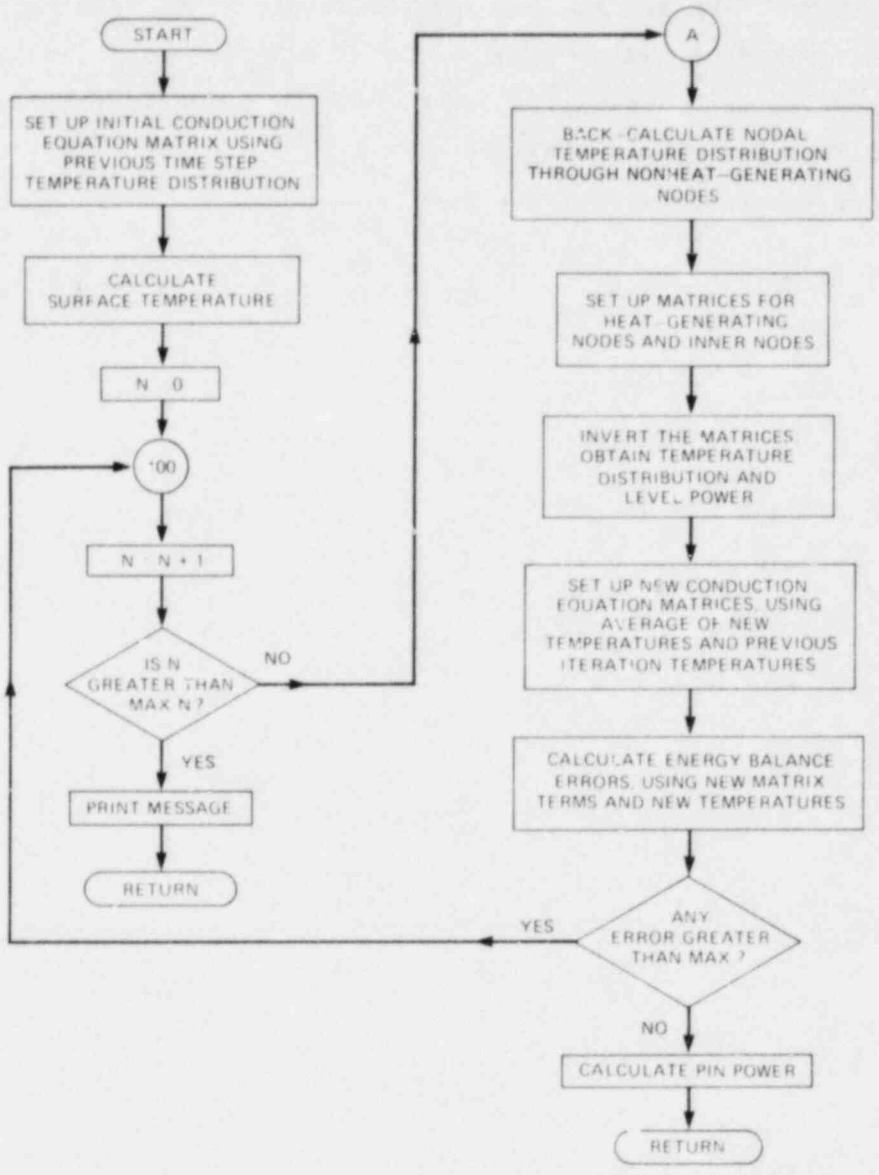

Fig. A.1. Simplified back-calculation method.

as

$$T_m = T_W + q'' \left[\frac{1}{r_s h_f} + \frac{\ell n(r_s / r_m)}{k_m} \right] . \qquad \text{(A.27)}$$

The temperature of the outermost node on the specified level of the pin is determined by Eq. (A.27), and the temperature of the next inner node is determined by solving Eq. (A.26) for T_{m-1}. Equation (A.25) is then solved for each successive inner node (T_{i-1}, beginning with $i = m - 1$) until a heat-generating node ($F_i \neq 0$) is reached. A matrix system is then constructed that has the form

$$\bar{A}_B \, \bar{T}_B = \bar{B}_B \, ,$$

where

$$\bar{A}_B = \begin{bmatrix} a_{1,1} & a_{1,2} & 0 & 0 & & & F_1 \\ a_{2,1} & a_{2,2} & a_{2,3} & 0 & & & F_2 \\ 0 & a_{3,2} & a_{3,3} & a_{3,4} & \cdot & \cdot & F_3 \\ \cdot & \cdot & \cdot & \cdot & & & \cdot \\ \cdot & \cdot & \cdot & \cdot & & & \cdot \\ \cdot & \cdot & \cdot & \cdot & & & \cdot \\ 0 & 0 & & a_{k-1,k-2} & a_{k-1,k-1} & & F_{k-1} \\ & & & 0 & a_{k,k-1} & & F_k \end{bmatrix} ,$$

$$\bar{T}_B = \begin{bmatrix} T_1 \\ T_2 \\ T_3 \\ \cdot \\ T_{k-2} \\ T_{k-1} \\ Q \end{bmatrix} , \qquad \text{(A.28)}$$

and

$$\bar{B}_B = \begin{bmatrix} b_1 \\ b_2 \\ b_3 \\ \cdot \\ \cdot \\ \cdot \\ b_{k-1} - a_{k-1,k} T_k \\ b_k - a_{k,k} T_k - a_{k,k+1} T_{k+1} \end{bmatrix} .$$

The solution is determined by inverting the matrix. The conduction equation matrix is then reformulated, using "iteration-averaged" nodal temperatures, defined as

$$\bar{T}_i = \frac{T_i^j + T_i^{j-1}}{2} , \qquad (A.29)$$

where j is the iteration counter.

An energy-balance error is calculated for each node as

$$\text{Error}_i = a_{i,i-1}\bar{T}_{i-1} + a_{i,i}\bar{T}_i + a_{i,i+1}\bar{T}_{i+1} + F_i\dot{Q} - b_i . \qquad (A.30)$$

If any Error_i is greater than a user-supplied value, the iteration is repeated, beginning with a recalculation of the temperature of the outer node. If all errors are smaller than the user-supplied limit, the pin power is determined by dividing Q (determined by inverting the matrix) by the level's axial power fraction; system power is then simply the pin power multiplied by a user-supplied factor.

NUREG/CR-2753
ORNL-5886
Dist. Category AN

Internal Distribution

1-20. W. G. Craddick
21. H. W. Hoffman
22. A. L. Lotts
23. D. G. Morris
24. C. B. Mullins
25. T. W. Robinson, Jr.
26. H. E. Trammell
27. ORNL Patent Office
28. Central Research Library
29. Document Reference Section
30-31. Laboratory Records Department
32. Laboratory Records, RC

External Distribution

33-37. Director, Division of Accident Evaluation, Nuclear Regulatory Commission, Washington, DC 20555
38. Office of Assistant Manager for Energy Research and Development, Department of Energy, Oak Ridge Operations Office, Oak Ridge, TN 37830
39-40. Technical Information Center, Department of Energy, Oak Ridge, TN 37830
41-140. Given distribution as shown under category AN (10 - NTIS)